10-13-2017

# Non-centrosymmetric Superconductivity and Magnetism in the Presence of Broken Symmetries

Mojammel Alam Khan
*Louisiana State University and Agricultural and Mechanical College*, mojammelkhan1987@gmail.com

# NON-CENTROSYMMETRIC SUPERCONDUCTIVITY AND MAGNETISM IN THE PRESENCE OF BROKEN SYMMETRIES.

A Dissertation

Submitted to the Graduate Faculty of the
Louisiana State University and
Agricultural and Mechanical College
in partial fulfillment of the
requirements for the degree of
Doctor of Philosophy

in the

Department of Physics & Astronomy

by
Mojammel Alam Khan
B.S.(Physics), University of Dhaka, 2011
M.S.(Physics), Louisiana State University, 2016
December 2017

*To my beloved parents and siblings.*

# Acknowledgments

I owe my gratitude to all my family, friends, and mentors who helped and guided me toward the pinnacle of my student life, which is this dissertation.

I would like to express my sincere gratitude and appreciation for my Ph.D. Adviser, Professor David P. Young. Without his continuous support and guidance, this dissertation would not have materialized. Throughout the years that I have worked under his supervision, I have immensely benefited from his wisdom, knowledge, and scientific acumen. He was always very patient and kind towards me in my learning years. His gentle, happy, and comforting attitude made the burden of hard times weigh less. For all his support, and for never losing trust in me, I will be eternally grateful to him, and I consider myself to be lucky to have him as my mentor and adviser.

I also have a deep gratitude towards professor John F. DiTusa. As my co-Adviser and mentor I have learned a wide variety of scientific topics from him. His vast knowledge in various aspects of physics encouraged me to learn more and made me rich as a researcher. I am grateful for his constant encouragement and constructive criticism that helped me to improve myself. I would also like to express my gratitude to him for including me in the LACNS projects that helped me learn new aspects and made this dissertation a success.

I would also like to thank and express gratitude towards my other committee members, Dr. Daniel Sheehy and Dr. Philip Adams. I have had many constructive discussions about various topics and gained more knowledge from them. I am grateful for their support in various stages of my research projects. I am also thankful to my collaborators Dr. Shane Stadler, Dr. Dana Browne, Dr. Ilya Vekhter, Dr. Rongying Jin, and Dr. Weiwei Xie (chemistry, LSU) for their support and help in performing experiments and measurements and discussions that helped me collect data, analyze them, and publish the results. I must thank Dr. Stadler for all the motivation and guidance he gave me countless times. I will remember our conversations at Highland Coffee on many afternoons about science, physics, and life in general.

I am thankful to all my friends at LSU who helped create an environment that enabled me to overcome my homesickness. I remember the fun and fruitful times I had with Jonny Olson, my friend and study partner who helped me tremendously. I am also grateful for the friendship of Dr. Mahmoud M. Asmar, a great theoretical physicist. I have learned a great deal about physics and life from the discussions we had at Highland Coffee and I will greatly cherish those memories.

Cheers to my parents and siblings and other family members who constantly supported me throughout my life. I want to thank them for their guidance, trust and encouragement all along.

# Table of Contents

# List of Tables

# List of Figures

# Abstract

Non-centrosymmetric (NC) superconducting and magnetic compounds have been synthesized and investigated using magnetic, specific heat, and transport measurements, as well as by neutron scattering and quantum oscillations. The crystal structures of NC compounds are defined by the lack of an inversion center. In NC superconductors, a finite antisymmetric spin orbit coupling originating from broken inversion symmetry results in unconventional Cooper pairing. Instead of a single spin channel, the order parameter is a mixture of spin-singlet and spin-triplet states. For NC magnetic compounds, the antisymmetric and isotropic spin interactions compete, leading to a helical ground state.

We have studied the NC superconductor $Re_6Zr$ through measurements of the magnetic, transport, and thermal properties in polycrystalline form as well as via electronic structure calculation. We observed a bulk superconducting transition at temperature $T_c \sim 6.7$ K. From the magnetic, magneto-transport, and heat capacity measurements, we extracted the critical field and other superconducting parameters of $Re_6Zr$. The upper critical field and thermal conductivity measurements indicate a relatively weak to moderate contribution from a triplet component to the order parameter, while the heat capacity and London penetration depth measurements favor a fully gapped superconductor. The results suggest a complex superconducting behavior with the possibility of point nodes in the superconducting order parameter.

We have also studied NC superconductor BiPd via quantum oscillations in its magnetization in an effort to probe the possible topological states of this compound. The search for topological superconductors (TSCs) is now at the forefront of condensed matter physics. TSCs are characterized by a full superconducting gap in the bulk and robust topologically protected gapless edge or surface states, which are Andreev bound states composed of Majorana fermions. Due to the presence of a Dirac point at 0.7 eV below the Fermi level of the surface in BiPd, topological surface states have been observed. The bulk superconductivity appears to be complex with the possible realization of vortex core states, suggesting

the order parameter is unconventional. We observed clear oscillations in the magnetization of BiPd using the de Haas-van Alphen (dHvA) effect. Several pieces of a complex multi-sheet Fermi surface have been identified. Among those, a 40-T pocket was found to be three dimensional and anisotropic in nature. From the temperature dependence of the amplitude of the oscillations, the cyclotron effective mass was found to be $(0.18 \pm 0.1)\ m_e$. Further analysis showed a non-trivial $\pi$-Berry phase associated with the 40-T pocket, which strongly supports the presence of topological states in the interior of BiPd and Dirac-like carriers in this band.

The NC compound $Ru_{1-x}Co_xGe$ crystalizes in the cubic *B20* structure. This particular structure is chiral, and doping the diamagnetic insulator, RuGe, with Co induces a magnetic state below 10 K, as indicated by a sharp peak in ac susceptibility measurements. For nominal 15% and 20% Co doping, the Curie temperature was found to be 6 K and 8.2 K, respectively. AC susceptibility and magnetization measurements show weak ferromagnetic behavior. The possible realization of helimagnetism, and an even higher order magnetic state known as the Skyrmion lattice, is explored and discussed.

# Chapter 1
# Introduction

One of the most fundamental characteristics that can be used to classify any object or to make distinction between countless numbers of objects is their inherent symmetry. Symmetries set the underlying framework to any phenomena, be it the formation of a crystal, or properties of a material. When water freezes and assumes a solid form, the continuous translational symmetry is broken. Interesting and often complex phenomena occur when other symmetries are broken as well. For example, in superconductivity, gauge symmetry is broken, and due to this, persistent currents can be realized in a superconducting ring or torus [1]. Coupled with the spin orbit interaction and other broken symmetries, a seemingly simple system can adopt to a variety of rich phases that are not only interesting from a purely scientific point of view, but also for many practical purposes. Here, we will be discussing the effect of broken symmetry, predominantly the inversion symmetry in superconducting and magnetic materials, which will henceforth be noted as noncentrosymmetric, as well as the role of spin orbit coupling (SOC) on their properties.

Any noncentrosymmteric structure can be defined by a lack of an inversion center, as shown in the simplified Fig. 1.1 for a molecule. It is common knowledge that a particular symmetry is defined by a set of operations through a given point in the structure, which upon completion, will reproduce the original structure. In the case of Fig. 1.1, clearly the structure doesn't reproduce itself upon an inversion operation. For example, if we use the inversion center, i, in this case the yellow atom located at the center of the molecule, and move each atom in the molecule along a straight line through the inversion center to a point at an equal distance from the inversion center, the resulting configuration is distinguishable from the original, and thus noncentrosymmetric. [2] This kind of broken inversion symmetry can have significant consequences on a materials properties, if the material also possesses strong SOC, which will be discussed as we progress through the literature.

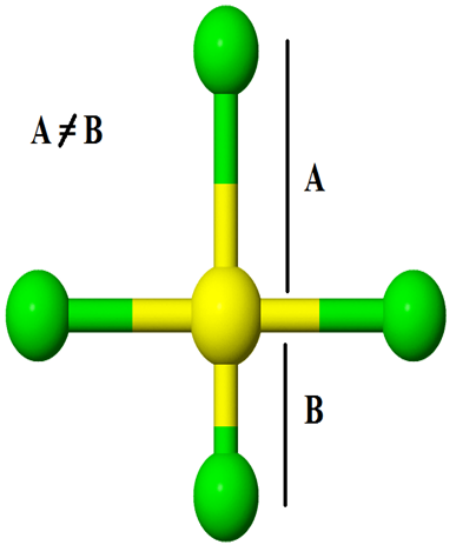


Figure 1.1: Noncentrosymmetry in two dimensions. Taking the yellow ball in the middle as the center for an inversion operation cannot reproduce the original structure, since A≠B, and hence it lacks an inversion center i.e. it is noncentrosymmteric

Spin orbit coupling (SOC) is one of the most fundamental and important interactions in materials besides the coulomb interaction. Spin is an intrinsic quantity of subatomic particles, and due to this electrons are associated with a spin magnetic moment [3], $\mu_s = -g_s \frac{e\vec{S}}{2m_0}$, where $g_s$ is the Lande factor and amounts to 2.003 [4]. Electrons in an atom also have motion with respect to the nucleus of the atom i.e the orbital motion. This orbital motion corresponds to the orbital angular momentum, and hence an orbital magnetic moment $\mu_l = -\frac{e\vec{l}}{2m_0}$. If we consider a reference frame where the electron is stationary, i.e. the electron's frame of reference, then the nucleus will be orbiting the electron, and hence will create a magnetic field. The electron, due to its spin magnetic moment, will be subjected to a force or torque due to this orbital field, which will attempt to rotate the spin moment as seen in Fig. 1.2.

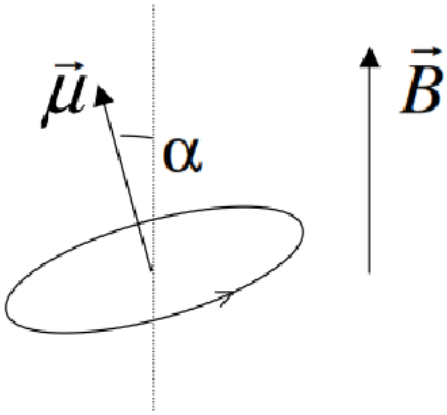


Figure 1.2: Magnetic interaction of a magnetic moment under a magnetic field $\vec{B}$. The induced torque tends to rotate the moment along the field and are perpendicular to both magnetic field and the magnetic moment. Illustration was taken from this Ref. [3]

Due to this interaction, the magnetic potential energy of the electron is given by,

$$E_{mag} = \int_{\pi/2}^{\alpha} (\vec{\mu_s} \times \vec{B_l}) d\alpha. \tag{1.1}$$

which gives us the energy to be $E_{mag} = -\vec{\mu_s} \cdot \vec{B_l}$ and immediately shows that the energy is minimized when the angle $\alpha$ is zero, i.e. the moment is aligned along the field direction [3]. In the parallel configuration, the energy is lower while in the anti-parallel configuration it is higher, which results in the splitting of energy levels of the atom in two. This interaction of the electron spin magnetic momentum with the orbital magnetic momentum is the spin-orbit interaction, and the corresponding change in the electron energy levels in an atom has some important consequences. The most fundamental of these is the fine structure splitting of the spectral lines of hydrogen. The splitting of the red spectral line in the visible spectrum is shown in Fig. 1.3. [3, 4] Other magnetic interactions, such as due to

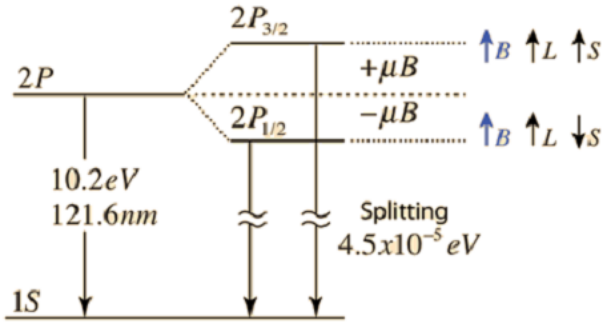


Figure 1.3: Splitting of spectral lines of hydrogen due to spin-orbit interaction. Illustration was taken from this Ref. [5]

nuclear spin and orbiting electrons, are much weaker and are responsible for the hyperfine structure of the energy levels. [3] Usually the SOC is larger in heavier atoms since the SOC constant, which is , $a \propto Z^4$, depends on Z, the atomic number of the atom. Presence of heavy elements in a compound lacking a center of inversion invokes interesting properties which will be discussed in the following sections.

## 1.1 Superconductivity

Heike Kamerlingh Onnes pioneered one of the most striking and promising scientific discoveries, when he cooled mercury metal below 4.1 K and measured its electrical resistivity. He found that mercury loses all of its resistivity at that temperature. This discovery of superconductivity in 1911 was followed by the observation of other metals that exhibit zero resistivity below a certain critical temperature. The fact that the resistance is zero has been demonstrated by persistent currents, i.e supercurrent, in superconducting lead rings for many years with no measurable reduction. An induced current in an ordinary metal ring would decay rapidly from the dissipation of ordinary resistance, but superconducting rings have exhibited a decay constant of over a billion years! Apart from zero resistivity, superconductors also show perfect diamagnetism i.e the Meissner effect[6], where the material in its superconducting state expels all of the magnetic flux from its volume. A characteristic sharp peak in heat capacity, denoting a sharp discontinuity at the superconducting transition[7] is also observed. With all its striking properties, supercon-

ductivity has remained as one of the most prominently studied avenues of condensed matter physics. This mechanism of superconductivity remained a mystery until early 1950, when the Ginzburg-Landau (GL) theory successfully explained the type-1 superconductor [8]. In the phenomenological GL theory, electrons are considered to behave like a single coherent wave. GL theory was followed by the theory of vortices by Abrikosov [9]. This theory explained type-2 superconductivity and the notion of the vortex field. This led to the discovery of superconducting magnets, which have been used in a wide range of sectors, including transportation (maglev train), medical diagnosis (MRI), particle accelerators, etc. Even after the success of GL and Abrikosov theory, the understanding of superconductivity, i.e the mechanism of forming the superconducting state, was not complete until 1957, when Bardeen-Cooper-Schrieffer (BCS) proposed the formation of Cooper pairs in the superconducting state [10]. From the isotope effect, it was known that the superconducting state appears through the interaction between electrons and lattice vibrations, and Cooper's work in 1956 laid the foundation for the electron-electron attractive interaction through phonons. Cooper showed that in the presence of an attractive interaction between the electrons, a bound state can exist between two electrons above the filled Fermi sea of a degenerate electron gas [11]. But a comprehensive framework of the mechanism wasn't fully realized until the BCS theory, which is essentially a many-body theory, where the superconducting electrons were treated via a many-body wave function, and the notion of Cooper pairs (electron pairs) was at its core. It was shown that the attractive interaction exists between two electrons with an energy difference less than the phonon frequency, [12] and thus within the energy $\hbar\omega_D$, the interaction is constant. The BCS model [1, 10, 13] is built on this idea of Fermi surface instability and the BCS ground state can be described by the Eq. 1.2.

$$\mid \psi_{BCS} >= \prod_{\vec{K}} (u_{\vec{K}} + e^{i\phi(\vec{K})} v_{\vec{K}}\, c^{\dagger}_{\vec{K}\uparrow} c^{\dagger}_{-\vec{K}\downarrow}) \mid \psi_0 > . \tag{1.2}$$

Here, $\mid \psi_0 >$ is the vacuum state with no particles present, and $\mid u_{\vec{K}} \mid^2 + \mid v_{\vec{K}} \mid^2 = 1$ implies the probability of the pair of electrons ($\vec{K} \uparrow$, -$\vec{K} \downarrow$) being occupied is $\mid v_{\vec{K}} \mid^2$ and $\phi$ is the phase of the condensate [1]. The creation operator $c^{\dagger}_{\vec{K}\uparrow}$ creates an electron with momentum $k$ and spin $s$ in the upward direction and the latter in the downward direction with opposite momenta, and hence the second term in Eq. 1.2 describes the creation of a cooper pair in the s-wave state. Thus, for the isotropic interaction the energy wave function is spatially symmetric, which leads to the formation of Cooper pairs with opposite spins. This ensures that the total pair wavefunction is antisymmetric under particle exchange [1, 14]. In this condensed state below the critical temperature, Cooper pairs are bosonic, having zero angular momentum and spin, and this state is referred to as the singlet state, even pairing, or s-wave pairing state.

Along with this pairing mechanism, BCS theory successfully explained and predicted many superconducting properties, including the size and nature of the superconducting energy gap. In a superconducting state the attractive interaction between electrons leads to the ground state being separated from the excited states by a small energy gap. The excitation energy is given by the following equation,

$$E_{\vec{K}} = \sqrt{\varepsilon^2_{\vec{K}} + \mid \Delta_{\vec{K}} \mid^2}. \tag{1.3}$$

Here, $\varepsilon_{\vec{K}}$ is the band energy and $\Delta_{\vec{K}}$ is the momentum $k$-dependent energy gap [1, 14]. For weakly-coupled BCS superconductors, the gap is given by,

$$\Delta_0 = 1.764 k_B T_c. \tag{1.4}$$

Deviation from this gap structure is common and mostly associated with unconventional superconductivity. The critical field, the thermal properties, i.e heat capacity, thermal conductivity, etc., as well as many electromagnetic properties, are a consequence of the energy gap [4].

For the isotropic interaction, we saw that the superconducting order parameter is a fully-gapped spin singlet, i.e S = 0 state. However, with strong on-site Coulomb interactions, other pairing states apart from s-wave spin singlet can occur, such as spin triplet pairing. In the spin triplet, or p-wave superconductors, the Cooper pairs form in an odd parity states with higher angular momentum, such as l = 1. For such a spin triplet superconductor with S = 1, the pairing state is described by a vector *d(k)* [15, 16]. Depending on the form of *d(k)*, the superconducting gap may become highly anisotropic and develop nodes in the gap. Another important consequence of such pairing is to realize non-unitary triplet states which break time reversal symmetry in the superconducting state [14, 17]. Similar to the l = 1 triplet pairing state, other pairing configurations with higher l values can also be found, such as the l = 2 spin singlet d-wave pairing with even parity.

The other important aspects of superconductivity, namely the coherence length and penetration depth, emerge as a natural consequence of BCS theory. The superconductor that can be described using the macroscopic BCS theory is known as a 'conventional' superconductor, and its properties follow well-described patterns, such as, exponential temperature dependence of heat capacity, London penetration depth, and thermal conductivity below the transition temperature [1]. Deviation from BCS behavior is particularly interesting and gives rise to unconventional superconductivity, which implies a pairing channel other than the symmetric s-wave state [18]. It is this key point that provides much of the impetus for this work. Here, we will investigate the physical properties of intermetallic superconductors that lack a center of inversion symmetry (noncentrosymmetric), where unconventional superconductivity is not uncommon.

## 1.2 Noncentrosymmetric Superconductors

Superconductors without a center of inversion in their crystal structure are known as noncentrosymmetric superconductors (NCSs), and they have been of tremendous research interest recently. Even though the NCSs were known for a long period of time, a resurgence in their study began in 2004. Discovery of the first NC heavy fermion superconductor,

$CePt_3Si$[18], followed by $CeRhSi_3$ and $CeIrSi_3$, and many other materials, sparked a fury of research effort to understand the superconducting nature of these materials. The ground state in BCS (conventional s-wave pairing) superconductors is formed where the total angular momentum of a Cooper pair is equal to zero (even pairing or singlet state), as discussed above. However, in an NCS, it is not possible to designate the pairing symmetry as either purely singlet (even pairing) or triplet (odd pairing), but instead the symmetry may be a mixture of the two.

In systems without inversion symmetry, an asymmetric potential gradient exists parallel to the unique crystal axis that is caused by the nuclei located at asymmetric positions. This gives rise to a spin-orbit interaction $(\vec{k} \times \Delta\vec{V}) \cdot \vec{\sigma}$ acting on electrons with momentum $\vec{k}$ and spin $\vec{\sigma}$. As a result, parity, and hence spin, is no longer a good quantum number. Consequently, the conventional classification of the superconducting states as a spin singlet, which are spatially symmetric ($s$,$d$-wave), or spin triplet, with antisymmetric ($p$,$f$-wave) wave functions of the Cooper pairs, no longer applies to these types of superconductors. In the most common situations, the strength of this antisymmetric spin-orbit coupling (ASOC) significantly exceeds the superconducting energy gap, pre-empting pairing between ASOC-split bands, and resulting in mixed singlet-triplet states [17, 19, 20]. This mixed state can be expressed as [21]

$$\hat{\Delta}(k) = i(\Delta(k) + d(k) \cdot \sigma)\sigma_y. \tag{1.5}$$

Here, the gap parameters $\Delta(k)$ and $d(k)$ represent the spin-singlet and spin-triplet pairing states, respectively, and $\sigma_y$ is a Pauli matrix. Due to finite ASOC, the degenerate bands will be split into sheets, and hence the resulting gap will be given by [14]

$$\hat{\Delta}_{\pm}(k) = \Delta_k \pm |d(k)|. \tag{1.6}$$

The above shows that the two gaps are a combination of constructive and destructive

interference of the singlet and triplet pairing terms [14]. The amount of mixing, i.e. the strength of the triplet paring term, depends on the strength of the ASOC, which is characterized by the vector *g(k)*. Due to this, the Hamiltonian is defined by the term $\alpha_{SO} g(k) \cdot \vec{S}$, where $\alpha_{SO}$ is the strength of the ASOC. Even though, in general the lack of an inversion center is detrimental to purely triplet pairing [22], the triplet pairing can be realized in unique crystal directions, where the triplet state is protected by symmetry [23], and degenerate electronic states can be achieved. This is more understandable from the viewpoint of irreducible representations of the corresponding crystal point group, where in many cases the gap anisotropy is required by symmetry [18]. In those cases, the gap parameter and the ASOC vector are parallel to each other i.e. $d(k)||g(k)$ for certain channels, and the triplet pairing state can realize [14]. If the triplet component is significant, the superconducting gap may become highly anisotropic, and develop line or point nodes [23–26]. Electron correlations are also important in realizing unconventional superconducting properties, and thus we can divide the realm of NCS's into two major parts, which are discussed below.

### 1.2.1 Strongly Correlated NCS Superconductor

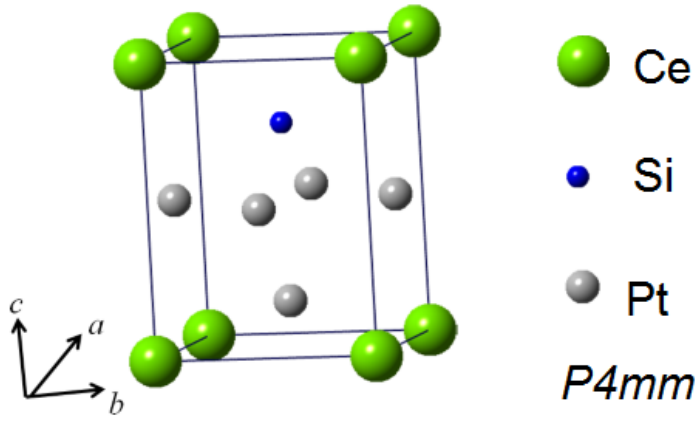


Figure 1.4: Crystal structure of $CePt_3Si$. Illustration was taken from this Ref. [14]

The first reported heavy fermion NCS was $CePt_3Si$, which is also strongly correlated and superconducts at ambient pressure with nodes in the superconducting gap [18, 27, 28].

This compound crystallizes in the primitive tetragonal structure with space group *P4mm* and clearly lacks a center of inversion, as seen in Fig. 1.4, and is hence, noncentrosymmetric. $CePt_3Si$ exhibits complex behavior, where it goes from a non-Fermi liquid behavior, to a magnetically ordered phase, and then to a superconducting phase upon lowering the temperature [27, 28]. Ce-based strongly correlated NCSs are a benchmark of this type, and among them, $CePt_3Si$ is the pioneer. In these compounds, the Kondo effect, in competition with the RKKY interaction, and crystalline electric field (CEF) effects dictate the ground state, which may lead to a magnetic quantum phase transition upon changing parameters, such as pressure or composition [18].

$CePt_3Si$ orders antiferromagnetically below 2.2 K, and within this magnetic ordering, it goes through a superconducting transition at 0.75 K. [18, 27, 28] The Ce atoms order within the basal plane [1 0 0] with a propagation vector of k = (0,0, 1/2) and an ordered moment of only 0.16 $\mu_B$, instead of 0.5 $\mu_B$, due to a Kondo type interaction [18, 29].

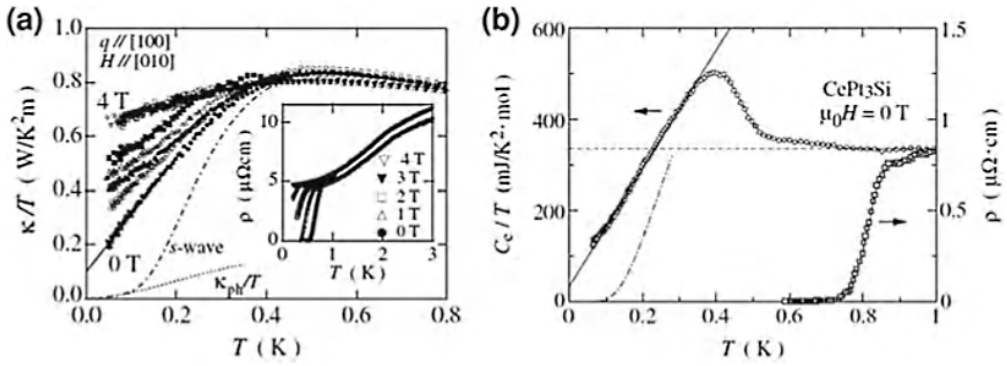


Figure 1.5: The temperature dependence of (a) Thermal Conductivity and (b) Heat capacity of $CePt_3Si$ indicated by left (axis) arrow and resistivity showing superconducting transition indicated by right (axis) arrow. The linear temperature dependence at low temperature is indicative of a nodal gap structure. The illustration was taken from Ref. [18], which presented the data from Ref. [30, 31]

The superconducting state of $CePt_3Si$ is very unique for multiple reasons. Apart from the coexistence of superconducting and antiferromagnetic states, the superconducting order parameter is anisotropic [18]. The unconventional nature of the superconducting state can

arise from a variety of interactions present in $CePt_3Si$, as well as strong ASOC, which amounts to $\sim 50 - 200$ meV spin splitting for several bands near the Fermi surface. [32] From thermal measurements, such as heat capacity, it was found that the low temperature behavior departs from BCS predictions [30]. Similar behavior was also observed for the low temperature thermal conductivity. In both cases, instead of an exponential temperature dependence associated with an activated energy gap, a power law behavior was found, as seen in Fig. 1.5. This power law behavior implies the existence of line nodes in the superconducting gap, indicating the existence of triplet pairing states [18, 30]. This aspect of triplet pairing in NCSs is rather intriguing, since it was pointed out by Anderson [22] that inversion symmetry is necessary to realize such a state. Even though it was later shown that the triplet pairing state is protected in particular crystallographic orientations for noncentrosymmetric structures [23] with a parallel *d(k)*, such pairing should account for point nodes in the gap. However, if the ASOC is large enough to allow for significant mixing of spin-singlet and spin-triplet pairing components with a larger triplet contribution, then line nodes can be found in the gap [18, 33]. A large ASOC of $\sim$ 200 meV points toward the latter scenario for $CePt_3Si$. The existence of line nodes in the gap was also found in a penetration depth study with similar low temperature behavior of the superfluid density, [34] corroborating the thermal measurements.

The Nuclear Magnetic Resonance (NMR) is a very useful tool to examine the gap structure via the spin susceptibility $\chi_s$ measured across the superconducting transition region. For BCS isotropic gap, arising from the s-wave pairing , the value of $\chi_s$ decreases due to the formation of copper pairs and emergence of spin zero state [18]. For a triplet pairing state such as p-wave, the $\chi_s$ is expected to remain constant at a particular crystallographic direction which can be seen in Fig. 1.6.

NMR measurements on $CePt_3Si$ are particularly interesting, since they do not show any sign of decrease in $\chi_s$ for any orientation [18, 35], unlike Fig. 1.6(b). This constant $\chi_s$ was attributed to the strong electron correlations present in this compound, and hence is

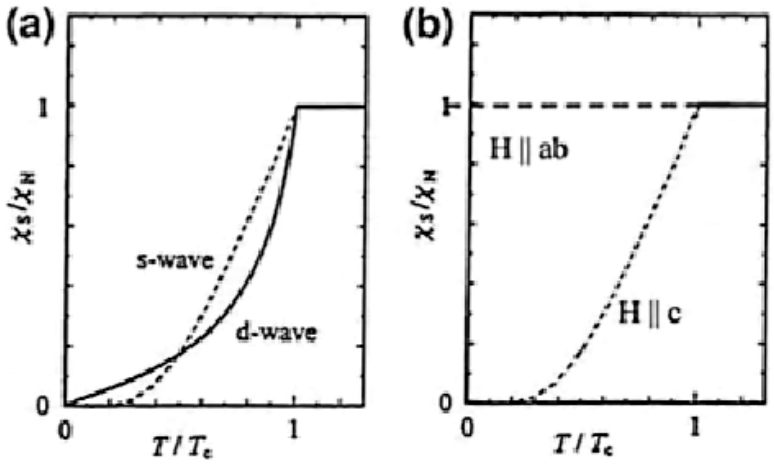


Figure 1.6: The temperature dependence of the electronic spin susceptibility for (a) s-wave and d-wave like pairing and (b) for triplet pairing states. The illustration was taken from Ref. [18]

not a good indicator for the existence of triplet-pairing states. [18].

The upper critical field ($H_{c2}$) is also often a good indicator of the spin pairing state of a superconductor. For $CePt_3Si$, $H_{c2}$ is nearly isotropic with a value of 5 T, which exceeds the Pauli limit, $H_p$, given by,

$$H_p = 1.83 T_c. \tag{1.7}$$

Electron-electron correlations, as well as the magnetic ordering, can eliminate the Pauli paramagnetic limiting field for all directions [18]. However, $H_{c2}$ was found to be close to the orbital limit of $\sim$ 4 T, indicating the existence of the spin triplet pairing state for $CePt_3Si$ [18]. The orbital field is given by,

$$H_{orb}(T) = \frac{\Phi_0}{2\pi\xi^2(T)}. \tag{1.8}$$

Here, $\xi(T)$ is the coherence length of the superconducting order parameter. In the case when $H_{c2}$ is determined by $H_{orb}(T)$, spin-triplet pairing is possible [18].

Several other Ce-based heavy fermion compounds also crystallize in noncentrosymmet-

ric structures and show exotic behavior under applied pressure. In fact, all of the similar compounds of $CeTX_3$ can be divided into two major groups with X = Si or Ge. $CeTSi_3$ with T = Co, Ru, Rh, Pd, Os, Ir, and Pt, and $CeTGe_3$ with T = Fe, Co, Rh, and Ir all crystallize in the noncentrosymmetric $BaNiSn_3$-type structure with space group I4mm. Many of these compounds except, $CeCoSi_3$, $CeRuSi_3$, $CeOSSi_3$, and $CeFeGe_3$ order antiferromagnetically [18]. Among these, $CeRhGe_3$ orders antiferromagnetically at 14.6 K and becomes superconducting above 8.0 GPa of applied pressure [36, 37]. The magnetic, superconducting, and other properties of some selected Ce-based heavy fermion compounds, along with other NCSs are listed in Table. 1.1.

In these compounds, in general, the competition between the RKKY interaction and a stronger Kondo interaction lead to a non-magnetic ground state, and by the application of physical pressure, a quantum critical point (QCP) can be reached, i.e. $T_N$ is driven to 0 Kelvin [14, 18]. Superconductivity often appears around the QCP for some of the compounds [18]. Interestingly, some of these show strongly anisotropic behavior in $H_{c2}$. For example, in $CeIrSi_3$, $H_{c2}(0)$ has a value of 9.5 T in a direction perpendicular to the $c$-axis, but the value of $H_{c2}$ is larger than 30 T along $c$-axis at an applied pressure of 2.65 GPa [38]. This clearly indicates that Pauli limiting is absent for field along the $c$-axis, and in that case, $H_{c2}$ is determined by the orbital limiting field [18]. Similar behavior was also found in $CeRhSi_3$ [39] and is consistent with the spin susceptibility calculated theoretically for the triplet-pairing state permitted by the noncentrosymmetric structure of these compounds [14, 26].

Apart from the Ce-based heavy fermions, only a handful of strongly correlated NCSs have been reported. Among those, UIr is widely known for its unconventional superconductivity [40]. UIr is ferromagnetic at 46 K at ambient temperature, and under applied pressure, the ordering is suppressed at around 1.7 GPa [40]. Interestingly, upon increasing the pressure, a second, but weaker ferromagnetic transition appears at 18 K at 1.9 GPa, which reveals a QCP at a critical pressure of 2.7 GPa. The superconductivity appears near

this QCP under pressure at 0.14 K [40]. This is a challenging theoretical problem from the standpoint of a noncentrosymmetric structure, where the spin degeneracy for a ferromagnet, like UIr, will be lost, and hence the superconductivity should be suppressed [40]. Interestingly, among all the compounds mentioned here, apart from $CePt_3Si$, none of the other members superconduct under ambient pressure. This severely restricts investigation of their pairing state in intrinsic form. Moreover, strong electron-electron correlations and the coexistence of magnetic order and superconductivity in $CePt_3Si$ also limits the understanding of the role of the strong ASOC in realizing the line nodes in the order parameter. As we discussed earlier, existence of line nodes and a constant $\chi_s$ are often taken as the evidence of mixed singlet and triplet pairing, but the existence of line nodes can also be explained as a consequence of a coupling of superconductivity with magnetic order, which can be seen in both centrosymmetric and noncentrosymmetric cases [14, 41].

Thus, even though most of these heavy fermion compounds show unconventional superconductivity, the role of ASOC due to the lack of an inversion center is not justified with certainty. This motivates the investigation of the superconductivity of the weakly correlated materials lacking an inversion center in order to clarify the role of ASOC on their superconducting properties.

### 1.2.2 Weakly Correlated NCS Superconductor

As the early research works on NCSs were heavily focused on Ce-based heavy fermions, the distinction of strong electron correlations from large ASOC on their superconducting properties was not well understood. Thus, it is of scientific interest to study the systems with weaker electronic correlations and large ASOC to understand the effect of the noncentrosymmetric structure on the superconducting properties. Among many weakly correlated NCSs, the role of ASOC on the order parameter is perhaps best understood by the canonical examples of $Li_2(Pd,Pt)_3B$. Both the $Li_2Pd_3B$ ($\gamma = 9\,mJ/molK^2$) and $Li_2Pt_3B$ ($\gamma = 7\,mJ/molK^2$) crystallize in the cubic perovskite type structure with space group $P4_332$, which lacks an inversion center as well as supports strong electron-electron

correlations. [42, 43] Thermal, magnetic, and NMR measurements on the superconducting properties of $Li_2Pd_3B$ established BCS s-wave superconductivity, which was in accordance with the small value of ASOC. [42, 44, 45]. In $Li_2Pd_3B$ spin splitting, due to ASOC, is about 30 meV, and the corresponding gap structure shows no sign of a spin-triplet pairing component, as the spin susceptibility observed in NMR decreases in the superconducting phase. [45] Substituting heavier Pt in place of Pd greatly enhances the strength of the ASOC, which is about 200 meV for $Li_2Pt_3B$, and the corresponding gap was found to contain line nodes from various measurements, such as heat capacity, magnetic penetration depth, as well as the NMR Knight shift [42, 42, 44, 45]. Since both compounds are isostructural, and their $\gamma$ values are comparable, the change in the structure of the gap is attributed to the change in the strength of the ASOC and subsequent splitting at the Fermi level. This was further elucidated by magnetic penetration depth measurements, which were modeled for both compounds. For $Li_2Pd_3B$ the data follow an s-wave like gap function, where as for $Li_2Pt_3B$ the data can be modeled with a gap consisting of an admixture of an isotropic singlet state and a triplet state, which is compatible with the ASOC of the corresponding crystal structure. [42] For $Li_2Pt_3B$, the ratio of the magnitude of the spin-singlet to spin-triplet pairing component is about 0.6, indicating the larger triplet paring component that ultimately yields line nodes in the gap, consistent with the larger ASOC. $Li_2Pd_3B$, on the other hand, has a ratio of 4, which indicates a dominating singlet state. [42]

Weakly correlated superconductors that are isostructural to the heavy fermions that superconduct under pressure are also of interest (see section 1.2.1). Compounds of the chemical form $RTX_3$ (R = Sr, Ba, La, Ca; T = transition metal; X = Si,Ge), which crystallize in the same $BaNiSn_3$ type structure without a center of inversion, are of particular interest. [14] Superconductivity has been found in several compounds, such as $SrPdGe_3$ ($T_c$ = 1.49 K), $SrPtSi_3$ ($T_c$ = 2 K), $SrPtGe_3$ ($T_c$ = 1 K) [21, 46, 47], $BaPtSi_3$ ($T_c$ = 2.25 K) [48], $CaPtSi_3$ ($T_c$ = 2.3 K), $CaIrSi_3$ ($T_c$ = 3.6 K) [49], $LaIrSi_3$ ($T_c$ = 0.9 K) [18], and

$LaRhSi_3$ ($T_c$ = 2.26 K) [50], all of which are classified as weakly correlated systems. Specific heat measurements of $BaPtSi_3$, $CaPtSi_3$, and $CaIrSi_3$ indicate that each is consistent with an isotropic superconducting gap of the magnitude predicted by conventional BCS theory [14, 18].

The search for NCSs resulted in finding other superconducting compounds, such as $T_2Ga_9$ (T = Rh, Ir), $Re_3W$, $Re_{24}Ti_5$, $LaNiC_2$, and $Re_6Zr$ [14, 17, 18, 51, 52]. Among these, apart from the latter two compounds, all of them show typical BCS type superconductivity in accordance with the small value of ASOC. The case of $LaNiC_2$, and $Re_6Zr$ are interesting, as these two are the only NCSs so far to show time reversal symmetry (TRS) breaking in the superconducting state, as probed by muon spin spectroscopy ($\mu SR$). [17, 51] TRS invariance is essential to allow for the spin-singlet pairing state to occur, while for the triplet-pairing state, it is not conserved [21].

$LaNiC_2$ crystallizes in the orthorhombic structure with space group *Amm2* and superconducts below 2.7 K. Magnetic penetration depth measurements indicate both the presence of point nodes and a fully gapped, two-gap superconducting gap structure. [14, 51]. Perhaps the most important experimental result is the observation of a spontaneous magnetic field at the onset of superconductivity, probed via $\mu SR$ measurements [51]. This unequivocally indicates that the TRS is broken in the superconducting state, which immediately points toward an unconventional pairing mechanism, such as non-unitary spin-triplet states, where the Cooper pairs are not in a spin-zero state, rather they are polarized [14, 21, 51]. A symmetry analysis of the corresponding irreducible representation of the crystal structure reveals that, while there are three non-unitary states compatible with the structure, none of these are allowed in the presence of a sizeable ASOC, which in the case of $LaNiC_2$ is negligible [14, 51], as seen in Table 1.1.

A similar TRS broken state was found at the onset of superconductivity for $Re_6Zr$, which is shown in our work and discussed in Chapter 3. Even with a negligible ASOC at the Fermi level in $Re_6Zr$, the TRS broken state can be well understood via the irreducible

representation of the space group [17, 53, 54]. Here, the symmetry analysis shows a non-unitary state is compatible with the TRS breaking and the high symmetry of the cubic $\alpha$-Mn space group, and a mixed singlet and triplet state was identified [14, 17]. These analysis suggest that although the ASOC in $LaNiC_2$ and $Re_6Zr$ is negligible, the unconventional pairing state may still arise as a sole consequence of the noncentrosymmetric crystal structure and its underlying point group symmetries [14, 18].

Further information is desired on the relationship between the nature of the pairing state and the strength of the ASOC. The following table 1.1 shows the superconducting parameters of various NCSs, including the value $E_r$, which is defined as the ratio of the amount of spin splitting due to ASOC (i.e. $E_{ASOC}$) to $T_c$: $E_r = \frac{E_{ASOC}}{k_B T_c}$, which represents the contribution of the spin-triplet component to the order parameter. [55]. It is easy to see that, except for $Y_2C_3$, the quantity $E_r$ serves as a good parameter to tune the mixed pairing states in NCSs. As a general rule, we can say that a large $E_r$ is usually required for a predominant spin-triplet state, and hence, unconventional superconductivity [18, 55].

Table 1.1: Normal and superconducting parameters of selected NCS superconductors. A more in depth review on NCS superconductors can be found in Ref. [18]

| Compound | $T_c$ (K) | $\gamma$ (mJ/mol K$^2$) | Gap structure | $E_{ASOC}$ (meV) | $E_r$ | Ref. |
|---|---|---|---|---|---|---|
| $CePt_3Si$ | 0.75 | 390 | Line nodes with $H_{c2} > H_p$ | $\sim$ 200 | 3093 | [27, 28, 30, 31, 55] |
| $CeRhSi_3$ | 1.05(p = 3 GPa) | 110 | Anisotropic, $H_{c2} > H_p$ | $\sim$ 12-80 | 883 | [18, 39, 56] |
| $CeCoGe_3$ | 0.7(p =7.1GPa) | 32 | Anisotropic, $H_{c2} > H_p$ | $\sim$13-48 | 795 | [57, 58] |
| $Li_2Pt_3B$ | 2.7 | 7 | Anisotropic, line nodes | $\sim$200 | 860 | [18, 42, 43] |
| $Y_2C_3$ | 15 - 18 | 6.3 | Two gaps/Line nodes | $\sim$ 9-20 | 11 | [59–61] |
| $LaNiC_2$ | 2.75 | 7.7 | TRS Breaking, two gaps/nodes | $\sim$ 42 | 117 | [51, 62–64] |
| $Re_6Zr$ | 6.75 | 27 | TRS breaking, single/two gaps/multi-band | $\sim$30 | 52 | [17, 53, 54] |
| BiPd | 3.78 | 4 | Anisotropic, Two gaps, $H_{c2} > H_p$ | $\sim$50 | 157 | [55, 65, 66] |
| $Li_2Pd_3B$ | 7 | 9 | Anisotropic, fully gapped | $\sim$30 | 49 | [18, 42, 43] |
| $La_2C_3$ | 13.2 | 10.6 | Isotropic/Two gaps | $\sim$30 | 26 | [59, 67] |
| $BaPtSi_3$ | 2.25 | 5.7 | Isotropic, single gap | $\sim$ 200 | 1000 | [18, 48] |

## 1.3 Noncentrosymmetric Magnets: Skyrmions and B20 Compounds

In the previous sections we have discussed the consequence of broken inversion symmetry and spin orbit coupling on the superconducting properties of NCS's. A natural question arises: How does the lack of an inversion center affect the other physical properties, like magnetism, for example, in these systems? A wide variety of research has been

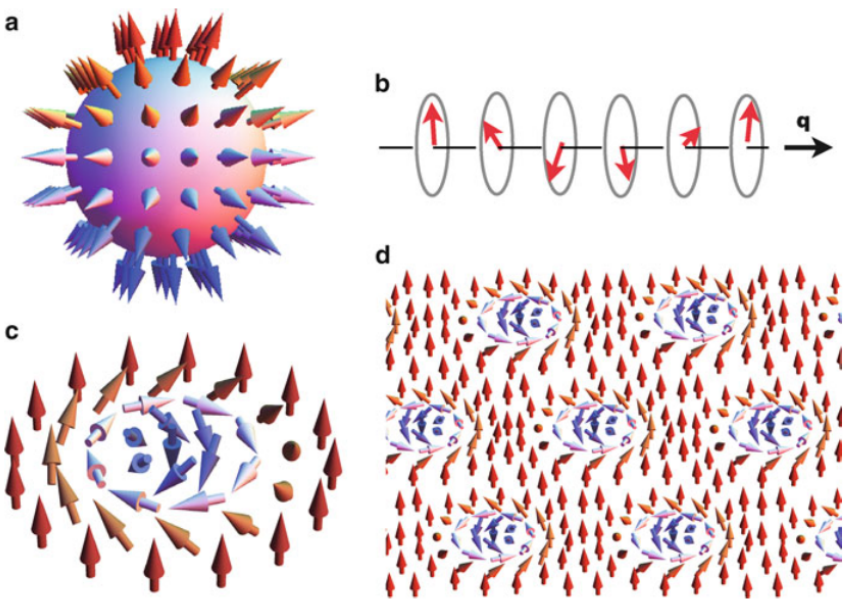


Figure 1.7: (a) Schematic description of the original hedgehog-type Skyrmion proposed by Tony Skyrme, where the magnetization points in all directions wrapping a sphere. (b) A schematic of the helical state realized in chiral-lattice magnets, such as the B20 cubic magnets, as a consequence of the competition between the Dzyaloshinskii-Moriya (DM) and ferromagnetic exchange interactions described in the text. (c) Schematic of a Skyrmion in the B20 compounds, which corresponds to a projection of the hedgehog type Skyrmion on a two-dimensional (2D) plane.(d) The Skyrmion crystal realized in chiral-lattice magnets under an external magnetic field in which Skyrmions form a triangular lattice with hexagonal symmetry. The illustration was taken from Ref. [68]

done, and it was found that for magnetic materials, a lack of an inversion center has some interesting consequences, which are important for applications of functional materials, as well as for basic science. A broad range of magnetic systems have been found to host non-collinear magnetic structures due to the lack of inversion symmetry, such as magnetic Skyrmions in the cubic B20 systems [70, 71], as well as magnetic chiral solitons [72] and other helical spin arrangements. In magnetic materials its the competition among multiple interactions that often gives rise to complex non-collinear or non-coplanar spin structures, such as vortices, domain walls, bubbles, and spirals [68]. Driven by spin-polarised electric currents, domain walls and vortices in metallic ferromagnets are useful in magnetic storage devices, such as race-track memory [68, 73]. Magnetoelectric cross-correlation phenomena,

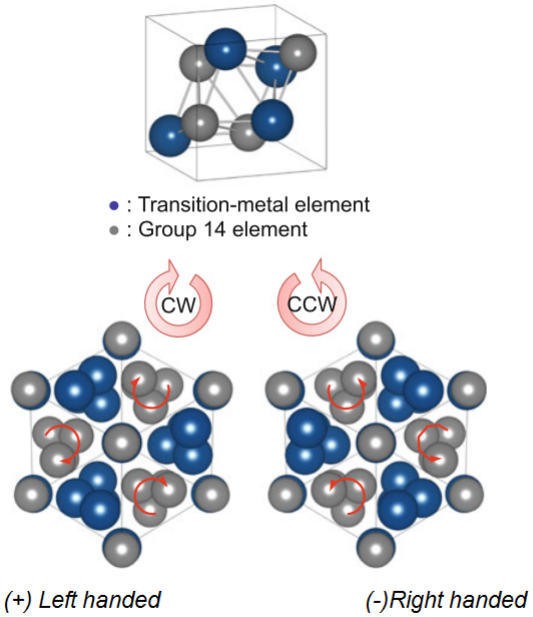


Figure 1.8: Schematic diagram of the B20 structure. The unit cell clearly lacks inversion symmetry. The lower panel shows the unit cell along the [111] direction. The left or right handedness is apparent, illustrating the chiral nature of the structure. The figure was taken from Ref. [69]

due to the coupling between magnetism and electricity in insulating magnets, gives rise to magnetic spirals through the generation of ferroelectric polarisation via a relativistic spin-orbit interaction [68]. In addition to these spin structures, perhaps the most important and scientifically interesting phenomenon is the magnetic Skyrmions, which are vortex-like swirling spin structures characterized by a quantized topological number. They are currently attracting considerable research attention, since their peculiar dynamic response to an external magnetic field holds high promise for applications involving spintronic devices. [68, 74, 75] Interestingly, topological Skyrmions were first predicted by Tony Skyrme in the field of high energy particle physics in the 1960s to account for the stability of hadrons as quantized topological defects in the three-dimensional (3D) non-linear sigma model [76, 77]. However, it also turns out to be of great importance in condensed matter physics, as a low energy excitation with a topological origin. A magnetic Skyrmion has

been experimentally realized in several condensed matter systems. It is composed of spins pointing in all directions and wrapping a sphere, similar to the spines on a hedgehog, as shown in Fig. 1.7(a). The number of such wrappings corresponds to a topological invariant, and thus, the Skyrmion has topologically-protected stability i.e. it is a topological quantity which is immune to external disorder [68].

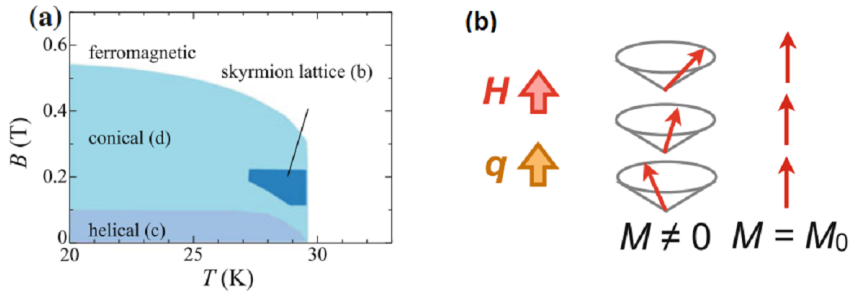


Figure 1.9: (a) Universal phase diagram of B20 compounds in the T-B plane [69]. (b) Schematic diagram of conical and ferromagnetic spin orientations. [68]

Skyrmions have been observed in many systems with distinct characteristics. Among them, the noncentrosymmetric (NC) chiral magentic systems are the recent additions. The realization of a Skyrmion phase in NC chiral magnetic system was predicted recently [78–80], and shortly after, experimental observation was made [81]. The exotic magnetism found in transition metal silicides and germanides having the B20 crystal structure, which has fascinated condensed matter physicists for a long time. Transition-metal elements and main group (14) elements with composition ratio of 1:1 will sometimes form in the cubic B20-type structure which lacks an inversion center, as well as mirror symmetry, as seen in Fig. 1.8. Among these B20 compounds, the prototypical itinerant magnet, MnSi, is the most heavily studied. It was investigated as a long wavelength helimagnet [82], a prototypical weak itinerant ferromagnet [83], a possible pressure induced quantum critical system [84], and most recently, as a host for a Skyrmion lattice. [85]. Other known B20 compound includes, FeSi, CoSi, FeGe, MnGe, RuGe and CoGe, where doping Co in FeSi results in magnetic ground state [69]. The B20 compounds are characterized by the

space group $P2_13$, which is No. 198 in the international table with the Pearson and Strukturbericht symbols being cP8 and B20, respectively. From Fig. 1.8 it is evident that the crystal structure not only lacks a center of inversion, but is also chiral. In the absence of inversion center, and with the presence of finite spin-orbit interaction or coupling (SOC), an antisymmetric interaction, namely the Dzyaloshinskii-Moriya (DM) interaction, exists along with the symmetric isotropic exchange interaction. [86, 87] Along with these two interactions, the crystalline field interactions (magnetic anisotropy energy) also exist, and they are hierarchical in strength, with the ferromagnetic exchange interaction being the strongest, then the DM interaction, and finally the easy axis anisotropy. These interactions are well separated in energy scale. This hierarchy of different magnetic interactions results in general magnetic properties of the B20 compounds and a generic theoretical description of this family. First, the ferromagnetic spin-spin interaction with $\propto S_i \cdot S_j$ works to align the spins parallel to each other i.e. in a collinear or ferromagnetic configuration, while the DM interaction with $\propto S_i \times S_j$ favors a mutually perpendicular spin arrangement i.e. 90° between spin directions [69]. For the NC B20 compounds, the Hamiltonian $\mathscr{H}$, and the total free energy $F$ of the spin system, are functionals of the spatial variation of the spins, S(r), and thus, can be expressed respectively as [88],

$$\mathscr{H} = \int dr \Big[ \frac{J}{2} \sum_{ii'} (\frac{\partial S_i(r)}{\partial r_{i'}})^2 - DS(r) \cdot (\nabla \times S(r)) - \frac{1}{2} K_1 \sum_i S_i(r^4) - H \cdot S(r) \Big], \quad (1.9)$$

$$
\begin{aligned}
F = & \Big[\frac{1}{2}(\chi(0)^{-1} + J\,Q^2)\langle S^2\rangle_p + \frac{1}{4}\gamma\,\langle S^4\rangle_p\Big] \\
& + \vec{D}[\vec{S_1} \times \vec{S_2}] \cdot \vec{Q} \\
& + \frac{1}{2}[A_1(\langle 3S_z^2 - S^2\rangle_p(3Q_z^2 - Q^2) + 3\langle S_x^2 - S_y^2\rangle_p(Q_x^2 - Q_y^2)) \\
& + A_2(\langle 3S_z^2 - S^2\rangle_p(Q_x^2 - Q_y^2) - \langle S_x^2 - S_y^2\rangle_p(3Q_z^2 - Q^2)) \\
& + 4A_3(\langle S_xS_y\rangle_p Q_xQ_y + (\langle S_yS_z\rangle_p Q_yQ_z + (\langle S_zS_x\rangle_p Q_zQ_x)] \\
& - \frac{1}{2}K_1(\langle S_x^4\rangle_p + \langle S_y^4\rangle_p + \langle S_k^4\rangle_p).
\end{aligned}
\tag{1.10}
$$

Here, the summation is over all the magnetic atoms/spins and $S_i$ is a unit vector along the direction of the $i^{th}$ spin of magnitude S. $J$ measures the strength of the ferromagnetic interaction, while $D$ is the strength of the DM interaction, and in general, J>>D. In the Eq. 1.10, the first term represents the ferromagnetic exchange interaction, the second is the DM interaction, and the third and fourth are the anisotropy energies, which are dependent on both S and Q, and only on Q, respectively [69]. The spin function $\mathbf{S(r)}$ has the form $\mathbf{S(r)} = \mathbf{S}_1\ \cos(\mathbf{Q}\cdot\mathbf{r}) + \mathbf{S}_2\ \sin(\mathbf{Q}\cdot\mathbf{r})$, since it is well established that the helical structure is comprised of a single $\mathbf{Q}$. Since the DM interaction is an order of magnitude lower in energy than that of the ferromagntic interaction, it can only produce a slight rotation of the spin, i.e. a small canting in an otherwise linear spin configuration. And thus, due to this competition, the ground state of these B20 magnetic compounds is a long-period spiral spin structure. The DM interaction term $\mathbf{D}[\mathbf{S}_1\times\ \mathbf{S}_2]\cdot\mathbf{Q}$ is thus important to not only produce the spiral structure but also for the stability of the long period helical order, in which the helical plane is normal to $\mathbf{Q}$. The ratio of $D$ to $J$ determines the $\mathbf{Q}$ and minimize the free energy, with its sign determining the rotation direction, i.e. the helicity of the spiral [69, 88], where $Q \approx |D|/J$. Finally, the direction of the spiral or helix is pinned along a certain crystal axis by the magnetic anisotropy interaction described by the third term of the Hamiltonian, which is also third in the energy scale.

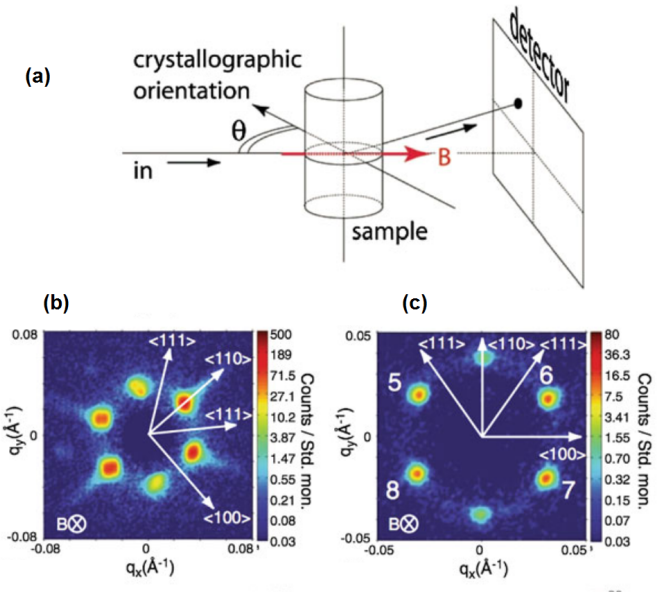


Figure 1.10: (a) Schematic description of the experimental setup of SANS on MnSi (b)-(c) Variation of the SANS pattern with magnetic field and the six-fold peak intensities. The spins are arranged in a triangular lattice and form in the plane normal to the applied field. The illustration was taken from [69], which took permission from the original work [85].

Below the transition temperature and zero applied field, the helical phase is stable, and the formation of this state has been seen in several B20 compounds, including MnSi, $Fe_{1-x}Co_xSi$, MnGe, and FeGe [68]. The typical helical period in these compounds ranges from 3 nm to 230 nm, and the direction of the spin is normal to the direction of Q. In addition to this helical structure, the application of a small magnetic field just below the transition temperature $T_N$, induces the Skyrmion phase (or A phase), which can be seen in Fig. 1.7(a,c). The occurrence of the Skyrmion lattice phase is intimately connected to the helimagnetic state having a characteristic wavevector that matches the helimagnetic (HM) wavevector, Q. Upon increasing the field, the helical structure transforms into a conical structure with modulation vector Q flopped along the field direction (Fig. 1.9(b)). And finally, a spin-collinear (ferromagnetic) state is observed above the critical field $H_c$ [69], where $H_C \approx D^2S/J$. The experimental confirmation of Skyrmions was probed in MnSi via small angle neutron scattering (SANS) by Mühlbauer *et al* [85]. In their SANS experiment, six magnetic Bragg reflections were observed in the T-H region of the Skyrmion or A-phase,

when the magnetic field was applied parallel to the incident neutron beam. A typical setup for a SANS experiment is shown in Fig. 1.10(a), and the six Bragg peaks are seen in Fig. 1.10(b-c). The six-fold peaks indicate that the Skyrmion magnetic structure has three independent Q values, since a single Q diffracts the neutron beam (unpolarized) into two positions (±Q) in reciprocal space. It was suggested[69, 85] that the Skyrmion phase is actually a superposition of the three helical structures corresponding to three different wave vectors with a mutual angle of 120° between them, which can then be regarded as a triangular lattice of spin-swirling objects, or spin knots, with a hexagonal symmetry i.e. the Skyrmion lattice. As discussed above, this Skyrmion is a topological object with an integer topological number i.e. winding number $\omega_\mu$. For the B20 compounds, the Skyrmion structure in spin space corresponds to a sphere, as seen in Fig. 1.7(a), with a winding number given by [85],

$$\int \frac{1}{4\pi} \hat{n} \cdot (\partial_x \hat{n} \times \partial_y \hat{n}) dx dy = -1. \tag{1.11}$$

Where the integer value corresponds to the topological index, and thus the stability of the Skyrmion phase.

Apart from the SANS work on MnSi, and eventually on other B20 compounds, real space observation of Skyrmions in $Fe_{0.5}Co_{0.5}Si$ by the Lorentz transmission electron microscopy (LTEM) method has been performed [81]. A magnetic force microscopy (MFM) measuremnt [89] was also done on $Fe_{0.5}Co_{0.5}Si$, and all of these experiments unequivocally established the existence and nature of the magnetic Skyrmions in the noncentrosymmetric B20 compounds. A list of these compounds are is given in the following Table. 1.2

Table 1.2: A list of B20 compounds hosting the skyrmion lattice.

| Material | $T_N$ (K) | $\lambda_m$ (nm) | Type | Ref. |
|---|---|---|---|---|
| MnSi | 30 | 18 | Metal | [75, 85] |
| $Fe_{1-y}Co_ySi$ | <36 | 40 to 230 | Metal | [81, 90, 91] |
| FeGe | 278 | 70 | Metal | [92] |
| MnGe | 170 | 3 | Metal | [93] |
| $Cu_2OSeO_3$ | 59 | 62 | Insulator | [71, 94] |

## 1.4 Goal and Outline

From the discussions above, it is evident that due to broken inversion symmetry, coupled with finite spin-orbit interaction, as well as other fundamental interactions, superconductors and magnetic systems can produce scientifically interesting phenomenon that can also be exploited in functional material applications. The role of the ASOC on the physical properties of NCSs is challenging, and more studies on similar systems are desirable. The chiral magnets forming in the B20 structures currently have only a few members that have been experimentally verified to support the Skyrmion lattice. The materials world is vast, and the majority of its phase space is still unexplored. Thus, the discussion above provides the motivation for further exploration of these intermetallic compounds. Our goal is to study systems that can help us understand the effect of these interrelated interactions in materials that lack inversion symmetry, as well as to synthesize new materials in an effort to probe deeper into the unexplored phase space.

This dissertation is structured as follows: In Chapter 2, we will discuss the general experimental details, such as the synthesis of single and polycrystalline samples, as well as characterization and measurement techniques. Some specific measurement techniques are discussed in the respective chapters, where a particular compound has been investigated.

In Chapter 3, we will discuss the NCS superconductor $Re_6Zr$, followed by a discussion of BiPd in Chapter 4. In Chapter 5, we will venture into some of the unexplored phase space mentioned above by presenting data on a new magnetic B20 phase: $Ru_{1-x}Co_xGe$, and finally in Chapter 6, we will conclude the dissertation by summarizing our results.

# Chapter 2
# Experimental Procedures

In this chapter I will discuss the synthesis, characterization and other technical details of the instruments I have used throughout my research endeavor at Louisiana State University (LSU). Synthesis of polycrystalline and single crystalline compounds are one of the cardinal parts of my research and hence an important part of this dissertation as well. For my personal research projects, as well as collaborative ones, I have synthesized a variety of samples using a multitude of techniques and equipment. The choice of the instrument and technique always depended on the nature of the sample, as well as the nature of the characterization techniques to be applied later. The synthesis of the materials at hand were primarily done in the department of Physics & Astronomy at LSU while some of the preliminary characterization and experiments were done in the departments of Physics, Chemistry, and Geology, Shared Instrument facility (SIF) as well as at national laboratories, such as the National High Magnetic Field Laboratory (NHMFL) in Tallahassee, FL and in several beam lines at the High Flux Isotope Reactor (HFIR) at Oak Ridge National Laboratory (ORNL). I will discuss the synthesis techniques and equipment setup in the following section and then the characterization in the subsequent sections.

## 2.1 Synthesis

A variety of melting, and hence synthesis techniques, are available in the synthesis laboratory in the Department of Physics & Astronomy at LSU. This is imperative to produce materials of different types which are at the core of this dissertation. The techniques that I used can be divided into two groups based on the nature of the sample i.e. whether the material was synthesized in polycrystalline form or as single crystals. The techniques include:

- Preparation of polycrystalline samples by arc melting, RF-induction melting, and by

solid state reaction in high-temperature tube and box furnaces.

- Synthesis of single crystal samples by a modified Bridgman technique with RF-induction, optical floating zone and zone refining, chemical vapor transport, and by metallic flux growth.

## 2.2 Polycrystalline Sample Synthesis

### 2.2.1 Arc Melting

The technique of arc melting is widely used in both small labs, as well as in large-scale industries. It is used to melt high melting temperature and low vapor pressure materials [95]. It uses an electric arc to heat and melt the material under an inert gas - usually ultra high purity (UHP) Argon (Ar). A small-scale laboratory arc melter consists of a water-cooled copper hearth and a tungsten rod as an electrode. The plasma arc is created between the tungsten electrode and the hearth by means of a welding power supply (see Fig. 2.1). After creating the arc, the materials melt due to the radiant heat from the arc, as well as the arc current passing through the material. The arc furnace can achieve temperatures in excess of 3000° C, which is considerably higher than standard tube and box furnaces that peak near 1500° C.

The typical mass of an arc melted sample is  1 gram. Starting materials to be melted are placed on a water-cooled copper hearth and a Zirconium (Zr) button that will be melted first as an oxygen getter. The sample chamber is then evacuated using a roughing vacuum pump and refilled with UHP-Ar (purging). This pump and purge cycle is repeated at least 4 times to minimize the oxygen content inside the chamber. Finally, the sample is melted under UHP-Ar. The sample forms a button after melting, and the button is flipped several times and re-melted to produce a homogeneous sample through a proportional mixing of the starting materials.

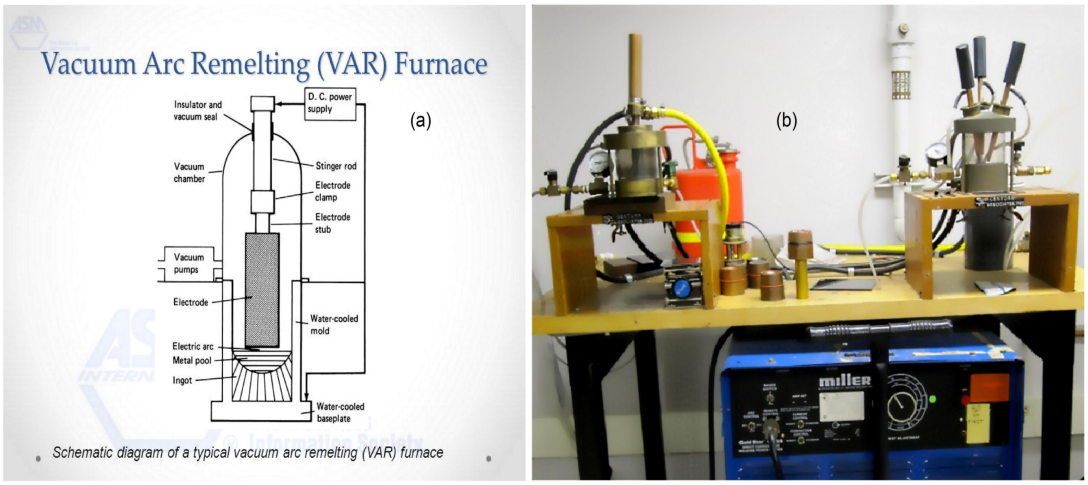


Figure 2.1: Arc melting (a) schematic diagram [96] (b) The single- and tri-arc furnaces, showing the front of the welding power supply [97].

- **RF-induction Melting**

Radio frequency (RF) induction heating relies on Faradays law of electromagnetic induction. As shown in Fig. 2.2(a), a high frequency ( 100 kHz) alternating current is applied through an inductor (work coil), which is a hollow copper coil. This produces an alternating magnetic field, and the metal or conductive material (work piece) that is to be heated or melted is placed inside the copper coil, so that a change in magnetic flux occurs through the work piece. The changing magnetic field from the work coil produces a large eddy current in the work piece, which eventually flows within a thin layer of its surface, which in turn increases its effective resistance [97]. This resistance is the key to the induction heating process and is otherwise avoided in other induction applications like transformers, for example. A secondary source of heat is the magnetic hysteresis which produces internal friction within the work piece. [99] One important distinction between arc melting and induction melting is that induction is a non-contact melting i.e. there is no contact between the heating element and the heat source, since the material is heated through induction, and hence the samples made through this process are much cleaner than

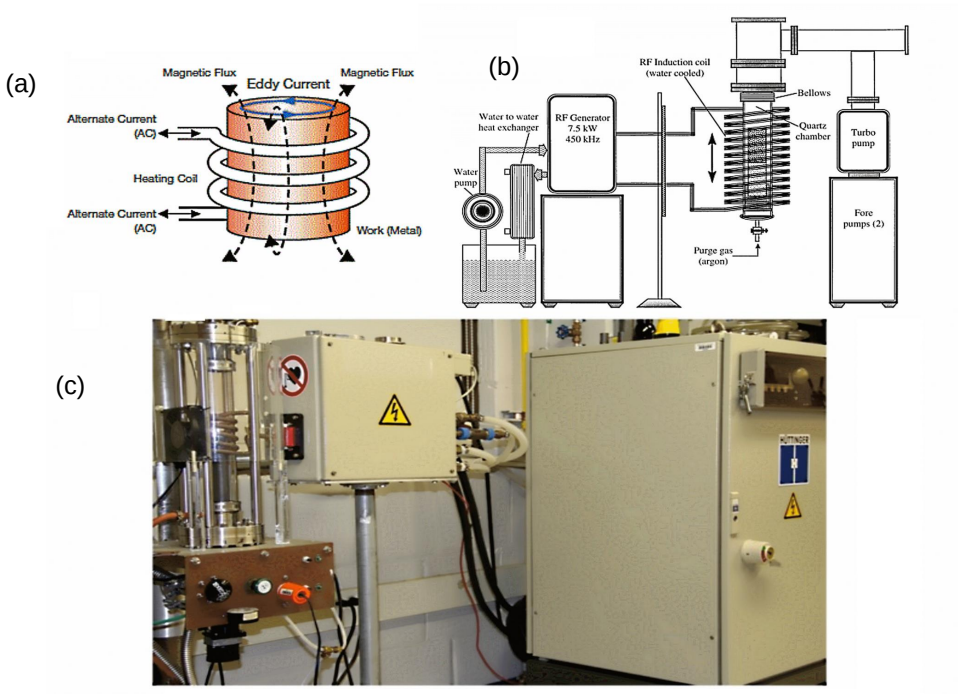


Figure 2.2: Induction melting: (a) A high frequency alternating current induces an intense and rapidly changing magnetic field through the work piece i.e. sample.(b) Schematic diagram of a typical laboratory RF-induction system. [98] and(c) RF-induction melting furnace in the Department of Physics and Astronomy at Louisiana State University. [97]

that of arc melting. Moreover, induction heating can be applied in vacuum, in gas, and even when the work piece is placed in a liquid solution. A typical polycrystalline sample consists of a stoichiometric mixture of the starting materials ( 2 grams) that are placed in an alumina ($Al_2O_3$) crucible, which is then wrapped by thin tantalum or niobium metal foil that acts as a flux susceptor. We have also used graphite crucibles, which can act as the flux susceptor itself, when the possibility of contamination from the graphite to the sample was minimal to none. Depending on the nature of the sample, the induction process was either heated in vacuum or under UHP-Ar to a complete liquid state. The RF supply unit we have in our lab (Fig. 2.2(c)) allows for a range of frequencies and power output (0 - 100 kHz),which gives us freedom to heat the sample slowly. This enabled us to melt high vapor pressure materials which are not possible to melt efficiently in arc melting. This process works for most of the intermetallic materials within melting temperatures of $\sim$2000° C and produces much cleaner sample than typical arc melting.

### 2.2.2 Solid State Reaction

Synthesizing polycrystalline materials by solid state reaction from a stoichiometric mixture of solid powder of starting materials using table top box and tube furnaces, as shown in Fig. 2.3, is perhaps the most widespread method of making samples. The choice of melting and temperature depend on the chemistry of the materials involved. Usually, the temperature of materials must be elevated above room temperature to get them to react, and a considerable time may be spent at this temperature to complete the reaction. The condition of the reaction, the thermodynamic free energy associated with it, coupled with structural properties and the available surface area for the reaction, will dictate the temperature and time scale required. [100].

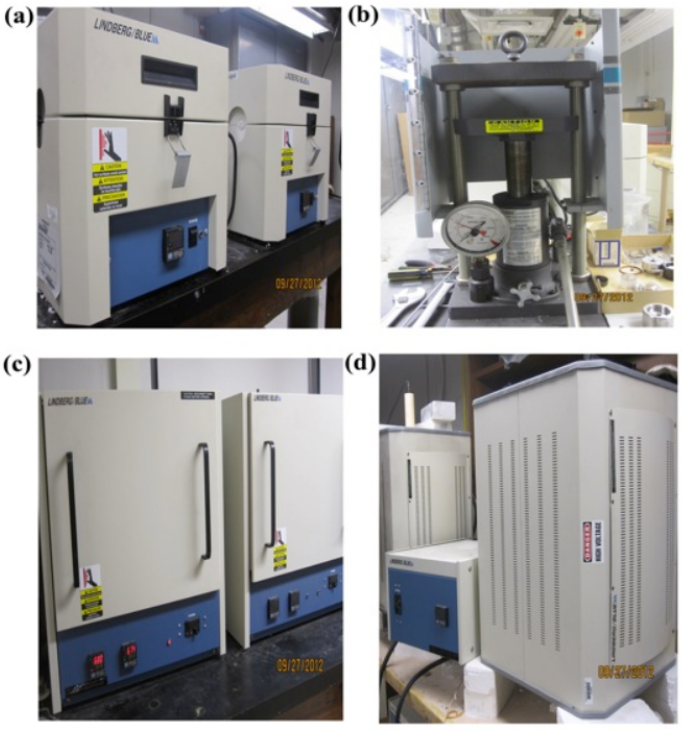


Figure 2.3: Table top tube(a) and box (c) furnaces. (b) Hydraulic pellet press instrument operating at room temperature i.e cold press. (d) High temperature vertical tube furnace in the Department of Physics and Astronomy at LSU [97]

In general a reaction might occur at temperatures as high as 1000–1600°C in 24–48 hrs. This method is particularly useful for volatile materials, since the temperature control

is precise with this technique, as opposed to arc or RF melting. The use of these furnaces shown in Fig. 2.3 is not limited to reactions only, as they can be used to anneal a pre-melt material to improve their homogeneity.

To make a sample by solid-state reaction, stoichiometric mixtures of the initial materials are weighed and then ground well with a mortar and pestle to obtain a good mixture. The powders are then pressed into a pellet by at least 3 tons of pressure using a stainless steel Graseby Specac die and hydraulic press (Fig. 2.2(b)). The pellet is then wrapped in Ta foil, placed in an alumina crucible, and sealed in an evacuated quartz tube (or under UHP-Ar). The tube is then placed in a horizontal tube or box furnace for sintering (Fig. 2.3(a)&(c)), where the maximum operating temperature is 1200°C - 1450°C.

## 2.3 Single Crystal Synthesis

Single crystals are more desirable for experimental investigations due to anisotropy that may emerge along different crystallographic directions. In single crystals, the effects of grain boundaries are significantly reduced, and hence studies of single crystalline materials provide more intrinsic behavior. Furthermore, certain experimental procedures require high quality single crystal samples to investigate certain properties, such as quantum oscillations in materials to study the Fermi surface as well as topological states, angle resolved photoemission spectroscopy (ARPES) to study surface states, as well as many of the neutron diffraction techniques. Thus, production of single crystals was of vital importance for this dissertation, and except for one particular system, which we will discuss in the next section, all other systems I have studied were prepared as single crystals. All single crystal synthesis attempts were made with one of the following techniques:

- Modified Bridgman technique
- Floating zone technique
- Metallic flux growth &
- Chemical vapor transport

Using these techniques, I was successful in growing large crystals using the modified Bridgman and floating zone techniques, which will be briefly discussed below.

### 2.3.1 Modified Bridgman Technique

The modified Bridgman technique evolved from the original Bridgman–Stockbarger technique that has been used for producing single crystals, as well as polycrystalline ingots. The method involves heating polycrystalline material above its melting point and slowly cooling it from one end of its container, where a seed crystal is usually located [101]. In the case of a modified Bridgman technique, a seed crystal may or may not be used, and while the container or the crucible is slowly cooled off, the cold tip solidifies and may act as the seed crystal. As the growth continues, a single crystal of the same crystallographic orientation as the seed is grown and usually forms along the length of the container. The process can be carried out in a horizontal or vertical orientation and in many cases the container was also rotated at a fixed rate. [101] This technique has been widely used in producing intermetallic materials, as well as semiconducting crystals, where the Czocralski process is more difficult. Control over the temperature gradient along the crucible can be difficult, since it is heated by induction. As such, not all intermetallics will grow high quality and homogeneous crystals. Nonetheless, for laboratory purposes where crystals up to few grams are sufficient to do experimental investigations, this process is effective.

We applied a modified Bridgman method using the rf-induction melting furnace as seen in Fig. 2.4. A tapered graphite crucible with a conical tip was machined and then used for the growth. Typically several grams of pre-reacted polycrystalline material were placed in the crucible, which was then sealed in a quartz tube under vacuum or placed directly inside the rf-coil chamber under UHP-Ar pressure. Once the crucible was positioned inside the rf-coil using the crystal puller, the materials were carefully melted through induction heating. The power was maintained to keep the melt in a liquid state. The crucible, and hence the molten sample, was then slowly lowered through the heating zone at a growth rate of 1-2 mm/hour, which successfully produced large crystals of several different materials, as

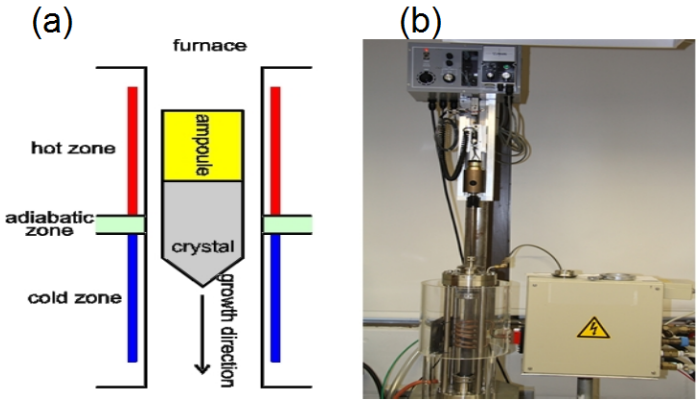


Figure 2.4: (a) Schematic block diagram of a typical modified vertical Bridgman crystal growth [102] (b) Modified Bridgman growth using rf-induction furnace with a crystal puller in the Department of Physics and Astronomy at LSU [97]

shown in Fig. 2.5.

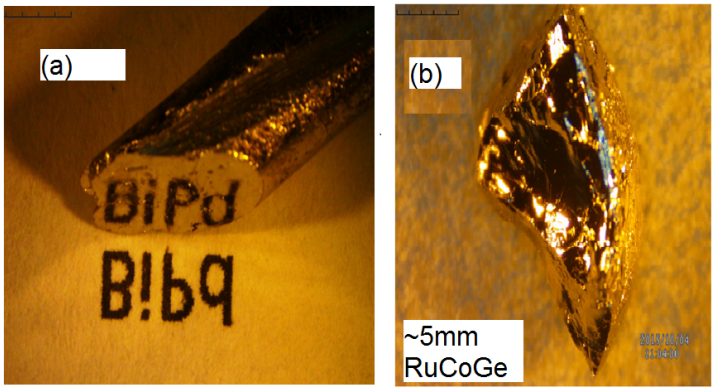


Figure 2.5: Examples of single crystals produced in our lab utilizing the rf-induction furnace with a crystal puller employing a modified Bridgman method (a) A piece of BiPd single crystal (b)Co-doped RuGe

### 2.3.2 Floating Zone

The optical floating zone (FZ) process, which is also known as the zone refining or zone melting [105], is a method of producing high purity single crystals of intermetallics and oxides, in which a narrow region of a crystal is melted first and then the molten zone is moved along the crystal growth direction. It is a sophisticated method, where two polycrystalline rods (one is used as feed and the other is used as seed) are simultaneously rotated in opposite directions to ensure homogeneity, as well reducing the possibility of producing

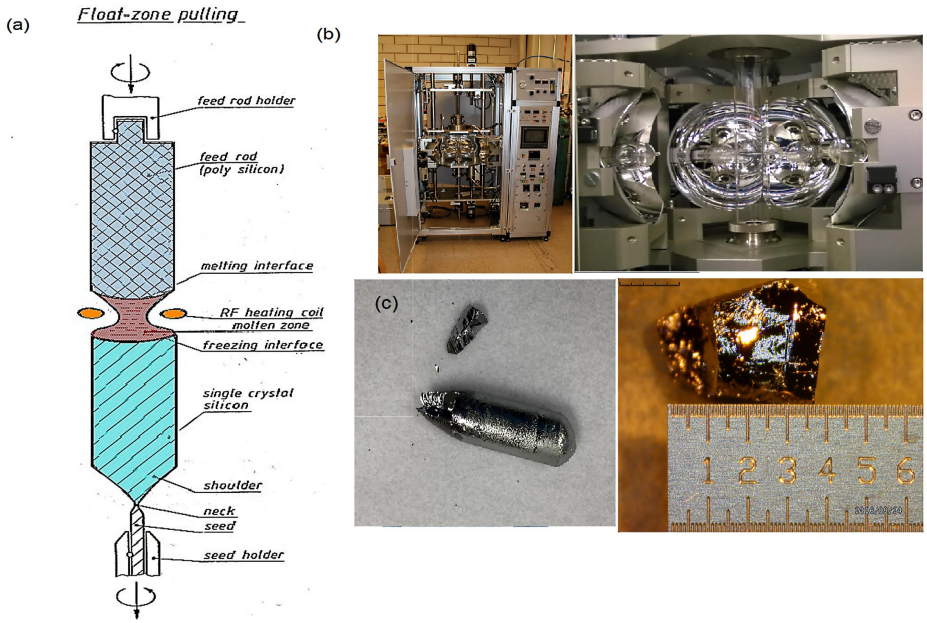


Figure 2.6: (a) Schematic diagram of FZ growth [103] (b) FZ furnace at LSU. A similar system can be found in many research labs [104](c) Some $Cr_{11}Ge_{19}$ crystals grown with the FZ technique.

multi-domain crystals. This method was invented by John Desmond Bernal [106] and was further developed in Bell Labs. While its early use was to produce high quality semiconducting crystals to make transistors, it can be extended to virtually any solute-solvent system with some concentration difference between solid and liquid phases at equilibrium [103]. This method cannot only produce single crystals, but it can also be used to refine the crystals further to ensure homogeneity and single domain crystalline product.

The most important part of any FZ system is the temperature control. The heating source is designed to produce a significant amount of heat as high as$\sim$3000°C and concentrate it over a narrow melting region. This molten zone is then moved through the entire length of the sample uniformly. A variety of heat sources can be used, from rf-induction to resistive heaters, as well as gas flames. Generally, the choice for research laboratory FZ furnaces is optical heaters that rely on halogen or xenon lamps that consist of two to four bulbs as heat sources and mirrors to concentrate their light at the hot zone. Some sophisticated FZ furnaces heat with lasers, and others allow application of hydrostatic pressure. A block diagram of a typical FZ furnace with an rf-induction heat source is shown in

Fig. 2.6(a). A typical image furnace similar to the one at LSU is shown in Fig. 2.6(b).

To synthesize crystals using the FZ furnace, a systemic procedure has to be followed which begins with the synthesis of starting material as a polycrystalline rod. Stoichiometric amounts of initial elements are melted in the rf-induction furnace. The product is then ground to a fine powder and pressed into long rods. For my crystal growths, I used a slightly different approach. Instead of making rods by pressing powders, which in many cases can be quite fragile, I melted the powders in very small diameter quartz tubes which were sealed under vacuum. The product was again a polycrystal but in a very straight rod shape with good homogeneity. This rod of starting material was then again put in a quartz tube and sealed under vacuum. It was placed in the FZ furnace and slowly lowered through the hot zone, which mimicked the modified Bridgman technique mentioned earlier. The difference between the growth in the rf-induction furnace and the FZ is that in the latter, precise control over the temperature gradient could be achieved, as well as a slower growth rate with a fixed crucible rotation. For example, to grow the $Cr_{11}Ge_{19}$ crystals, which can be seen in Fig. 2.6(c), a growth rate of 0.5 mm/hour was used, and the sample was rotated by $\sim$ 30 rev/minute.

## 2.4 Analysis

Once the samples have been synthesized, the next step is to verify their phase purity and investigate their physical properties. No crystal is perfect, and it will contain impurities and possibly other phases. Careful investigation of its structure and stoichiometry is imperative. In the following sections, I will discuss the structural analysis process, which will be followed by a description of the physical properties characterization.

### 2.4.1 Crystal Phase and Elemental Analysis

Crystal structure, and hence the phase purity, can be investigated through X-ray diffraction (XRD), as well neutron scattering. XRD is widely used in almost every research laboratory around the world. Both single and polycrystalline (powder) samples can be analyzed using XRD, which helps to verify the crystal structure of the system at hand. Once

the structure is determined, elemental analysis was done either by wavelength dispersive spectroscopy (WDS) in an electron microprobe or energy dispersive spectroscopy (EDS) in a scanning electron microscope (SEM).

- **XRD Analysis**

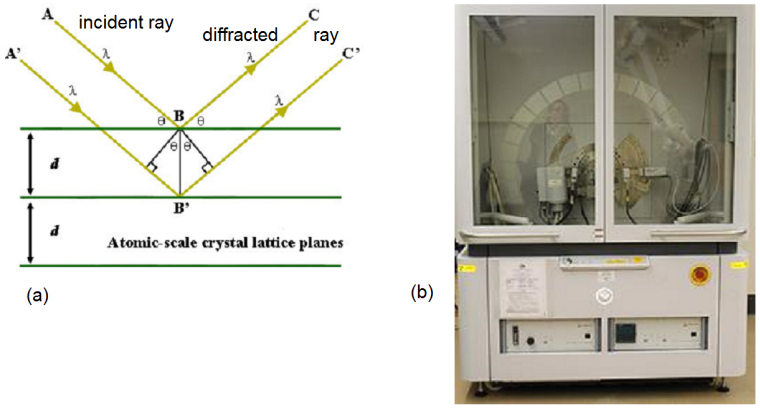


Figure 2.7: (a) Schematic diagram of XRD from Bragg's law [107] (b) The powder XRD diffractometer at SIF, LSU [108].

All of the materials we have studied were measured with either powder XRD or single crystal XRD analysis. As a general rule of thumb, prior to performing any other characterization on a material, an XRD spectrum is measured. All of the powder XRD was done at the Shared Instrumentation Facility [108] (SIF) at LSU. At SIF, a Panalytical Empyrean multipurpose diffractometer equipped with PreFIX (pre-aligned, fast interchangeable X-ray) modules and a PIXcel3D detector is used for XRD analysis. This system provides a maximum usable range of -111° $< 2\theta <$ 168° with a $2\theta$ linearity equal to or better than ±0.01°. Typically, a Cu $K_\alpha$ radiation source with $\lambda = 1.540562$ Å is monochromatized and used as a multipurpose diffractometer to analyze polycrystalline samples. For single crystal analysis, a Nonius Kappa CCD X-ray diffractometer with a graphite monochromator and Molibdenum $K_\alpha$ radiation of $\lambda = 0.71$°Å was used, which is located in the department of Chemistry at LSU. In General, for powder XRD, a small amount of sample to be analyzed is ground into fine powder and then placed on top of a zero-background flat silicon stage. Almost all of the powder XRD was performed using the $\theta$-$2\theta$ geometry, and data were taken from 10° to 90° at a constant scan of 2° per minute at room temperature. When the

incident beam interacts with the target (sample), the outgoing beams are diffracted in all directions and undergo constructive interference at angles governed by Bragg's law [4], as shown in Fig. 2.7(a).

If we consider specular reflection from parallel lattice planes separated by a distance d, then when the X-rays are incident on the sample, reflection from successive planes will have a path difference of 2d sin$\theta$, where $\theta$ is the angle of incidence and reflection and measured from the plane as shown in Fig. 2.7(a) for rays A and A$'$. Constructive interference will occur between the reflected beams from successive planes (C and C$'$), when this path difference is equal to an integral number (n) of the wavelength of the incident beam, $\lambda$ [4]. Thus

$$2dsin\theta = n\lambda. \tag{2.1}$$

It is important to mention that even though reflections from all the parallel planes are specular, only at a certain $\theta$ values all reflections from all planes will add in phase to give a strong reflection, and hence a strong peak in the diffraction data [4]. Bragg's law is a natural consequence of the periodicity of the crystals, and hence the symmetry of the structure. Thus, each reflection can be assigned to integer set of indices (hkl), which are also known as the Miller indices. Finally, the information about the lattice cell dimensions can be determined by Fourier transformation of the diffraction data [107]. Usually, the technique of Rietveld refinement is employed to find the unit cell information, as well as phase information using the Full prof [109] program.

- **SEM**

Scanning Electron Microscopy (SEM) is one of the most widely used techniques for investigating sample surface topography, which uses electrons instead of light to produce a high resolution image [110]. Since the SEM uses electromagnets instead of lenses to focus, a much greater magnification can be achieved, as well as a greater contrast between the smallest features on a specimen. SEM can also be used as a microprobe for elemental analysis.

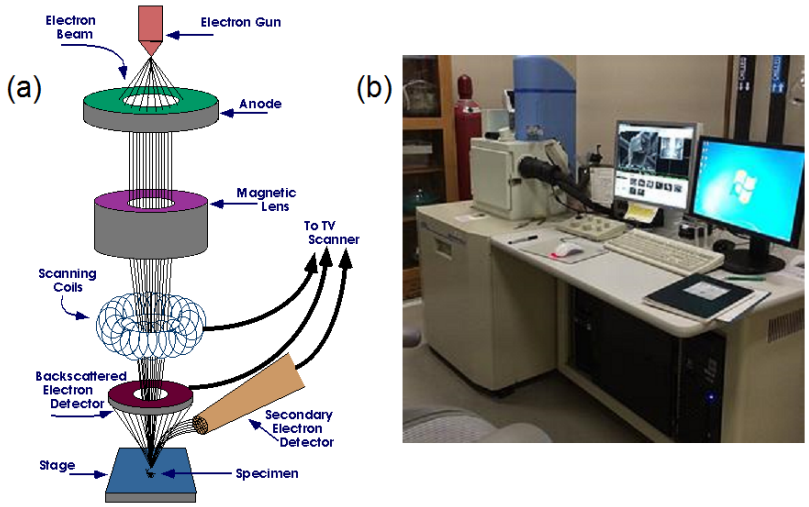


Figure 2.8: (a) Schematic diagram of an SEM [110] (b) The JSM -6610 LV SEM instrument at SIF, LSU [108].

In an SEM, a beam of electrons is produced by an electron gun, as shown in Fig. 2.8(a). The beam travels through electro-magnetic fields in vacuum toward the bottom of the microscope and interacts with the sample. The samples are prepared in a conductive state, which is relatively simple, if the sample is itself conductive. Upon the interaction, the sample emits X-rays (used for elemental analysis, EDS) and electrons, such as backscattered electrons (used for crystal structure and orientation), secondary electrons (used for imaging), and Auger electrons, all of them are collected by the detectors and processed further [110].

- **WDS**

Unlike in SEM, wavelength dispersive spectroscopy (WDS) primarily focuses on the X-rays emitted from the sample upon interacting with the high energy incident electron beam, which provides a much higher resolution for elemental analysis than SEM alone, which can be seen in Fig. 2.9(b).

For some of our single crystal specimens, the elemental analysis was done using the JEOL JXA-733 SuperProbe Electron Probe Microanalyzer (EPMA) in the department of Geology under SIF at LSU. After the sample is bombarded with the incident electron beam, the X-rays generated from the sample are collected and passed through an analytical

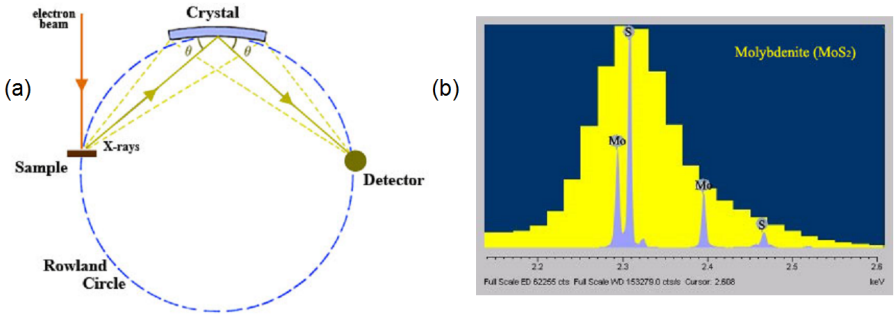


Figure 2.9: (a) Schematic diagram of a WDS configuration (b) Comparison of resolution of Mo and S spectral lines in EDS (yellow) vs. WDS (grey). The figures were taken from this [111] reference.

crystal at a certain angle $\theta$. Thus, only the X-rays that satisfy Bragg's law are reflected, so that only a single particular wavelength corresponding to a specific element is passed on to the detector [111] (Fig. 2.9(a)). The collected rays are then corrected for the atomic number of the element (Z), absorption in the sample (A), and finally the fluorescence (F). Collectively, this correction is known as a matrix or ZAF correction [97]. The final result of the analysis is then displayed as a function of the weight percentage of the elements present in the specimen.

### 2.4.2 Physical Property Characterization

Physical properties, such as electrical resistivity ($\rho$), thermo-power (S), magnetization, heat capacity, etc., were investigated to identify the fundamental behavior of a material and were measured using a variety of tools. In the following sections, I will briefly discuss the instruments and techniques that are generally used for the types of materials I have investigated. Specific measurement techniques, such as de Haas-van Alpen (dHvA) and neutron scattering, will be discussed in their respective chapters.

- **Physical Property Measurement System (PPMS)**

The Quantum Design (QD) Physical Property Measurement System (PPMS) is a cryogenic measurement platform, which provides precise control over temperature and magnetic field. The Model 6000 is the platforms main control unit, and it interfaces with various options to perform several measurements, such as AC transport (resistivity), ACMS op-


Figure 2.10: The PPMS in Dr. David Young's lab in the Department of Physics and Astronomy at LSU [97]

tion (AC susceptibility, magnetization), and heat capacity options. As such, the PPMS is the primary workhorse of our lab. Apart from these plug and play options, we also could customize a breakout box to connect with external systems to measure other parameters, such as thermoelectric effects utilizing Labview software. The system is kept cold using cryogens such as liquid nitrogen (outer dewer, nitrogen jacket) and liquid Helium (cryostat, inner dewar with probe) and can vary temperature from 1.8 K to as high as 400 K. This wide range of temperature enables us to perform measurements on a variety of systems, including: superconductors, magnetic systems, as well as semiconductors and insulators. A niobium alloy superconducting magnet produces a field of $\pm$ 9 T, which can be operated in both persistent mode to save energy, and hence Helium, and driven mode for faster measurements. Usually the temperature control has an accuracy of $\pm$ 0.5% with a slew rate of 0.01-12 K/min with sweep capability [112].

The measurement probe is immersed in liquid Helium and incorporates sensors, such as temperature control, helium level meter, gas lines, sample puck connector (pin head), and other required electrical connections. The alternating current (AC) measurement system (ACMS) option was used to measure magnetic susceptibility. The ACMS option consists

of drive and detection coils, electrical connector, as well as its own thermometer. The whole assembly is put inside the probe and fits directly into the sample chamber that contains a uniform magnetic field region produced by the superconducting magnet. For AC measurements, the AC drive coil provides an AC magnetic field while the detection coil measures the inductive response to the combined effect of the sample moment and drive field [97, 112].

- **Transport Properties**
  - Electrical Resistivity:

Materials can carry energy as well as be used as a transport medium. Usually the energy is transferred as an electrical current (conductivity, $\sigma$) , heat ( thermal conductivity, $\kappa$) or as sound waves. By studying these transport phenomena in depth knowledge about the materials electronic state, as well as correlation effects and interactions between carriers and phonons can be understood.

In general, a materials ability to carry electrical charge, i.e current is defined as its conductivity [4] and is given by,

$$\sigma = \frac{1}{\rho} = \mu n e \tag{2.2}$$

Here, $\mu$ is the mobility of the carriers which is related to the scattering rate $\tau_q$ (the relaxation rate of the carriers), $n$ is the number density of the charge carrier (carriers per unit volume), and $e$ is the charge of an electron. Unless a material is in a superconducting state, it will not carry current without any loss. This loss is due to resistance, and every material has a unique resistivity $\rho$, given by,

$$\rho = \frac{RA}{L} \tag{2.3}$$

Here, A is the cross-sectional area of the material, and L is the length. The resistance to the current originates from multiple sources, including, crystal imperfections, disorder,

impurities, as well as electron-phonon scattering. At high temperatures, the collisions between the conduction electrons and the lattice phonons dominates, where as at low temperatures, impurities and disorder dominate and gives rise to the residual resistivity ($\rho_0$(T)) at zero temperature. Since the electrons are fermions and follow the Fermi-Dirac distribution, for metals the charge carrier density $n$ is independent of temperature, and the only temperature-dependent term is the mobility, which is related to $\tau_q$, and hence the scattering processes described above. It is obvious that different materials, such as metals, semiconductors, and insulators, will differ in their respective conductivity. Metals typically have resistivities of a few micro-ohm cm ($\mu$ $\Omega$-cm), semiconductors show a few milli-ohm cm (m$\Omega$-cm to $10^2$ m$\Omega$-cm), and insulators can be in the mega-ohm cm range [4]. Their temperature-dependent resistivity behavior is also different, as metals show decreasing resistance (i.e. increasing conductivity) with decrease in temperature. Semiconductors and insulators, on the other hand, show an increase in resistivity with decreasing temperature. Thus, the temperature-dependent transport behavior of a material can be used to classify it. Typically, the electrical transport properties of metals at low temperature are described by Fermi-Liquid (FL) theory [4]. Here, electron-electron interactions are important, and the resistivity is given by the following:

$$\rho = \rho_0 + AT^{\alpha}. \tag{2.4}$$

where $\rho_0$ is the residual resistivity, A is the generalized Fermi coefficient (which gives information about electron-electron correlations), and $\alpha$ is the temperature dependent exponent. From the value of $\rho_0$ and the resistivity at room temperature, crystal purity can be assessed through the value of the residual resistivity ratio (RRR), where RRR = $\rho_{290K}/\rho_0$. For a high purity metallic crystal, RRR values can be over a few thousand. The temperature dependence of many semiconductors and insulators is activated and can be described

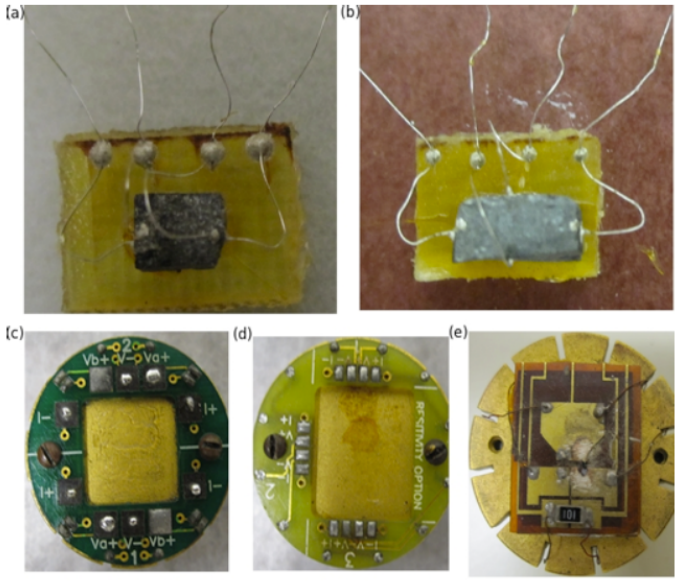


Figure 2.11: The electrical resistivity measurement arrangement. (a) Four probe technique, where four electrical contacts using platinum wires are attached to a polished sample. The outer two leads are current leads, and the inner two are voltage leads. This is a longitudinal configuration for resistivity. (b) Transverse arrangement is used for Hall resistance. (c) AC resistivity puck (d) DC puck and (e) MMR stage for thermo-power. Pictures were taken from this [97] reference.

by the Arrhenius formula [4],

$$\rho = \rho_0 e^{\frac{E_g}{2K_B T}}. \tag{2.5}$$

where $E_g$ is the band gap separating the conduction and valence bands, and $K_B$ is the Boltzman constant. From a logarithmic plot of the resistivity versus inverse temperature, the value of the band gap can be found.

In our laboratory, the resistivity of the materials under study was measured by a standard four-point probe method. The samples were usually cut and polished to a bar-like shape, and their dimensions were measured in order to calculate the cross-sectional area. The length L is the distance between the two voltage contacts as seen in Fig. 2.11(a). The electrical contacts were usually platinum wires of 0.002-inch diameter and are attached

to the sample using a two-component conductive epoxy (Epoteck H 20E). The sample and leads were placed on a small insulating plastic sheet (G10) with GE vacuum grease. Once the lead wires were attached to the sample, it was placed on a hot plate for a few minutes to cure the epoxy. The sample was then connected to the PPMS sample stage (puck) by soldering the leads to the puck contact pads, and then placing it into the PPMS sample chamber. A small current of 0.1- 3 mA, was used for excitation, and the resulting voltage was measured automatically, with the resistivity being calculated by the software using Ohms law.

$$V = IR. \tag{2.6}$$

The AC transport option of the PPMS gives the data as resistivity versus temperature plots.

- Thermal Conductivity:

Thermal conductivity ($\kappa$) is a transport property of any material [113]. A material's ability to transfer heat is exploited over a wide range of applications, including use as heat sinks (materials with high $\kappa$) and as thermal insulators (materials with low $\kappa$), and hence they are of great importance. A material with a temperature difference along its length will conduct heat energy from the high to low temperature end. The heat ($Q$) conducted during a time $t$ through a bar of material is given by

$$Q = \frac{(\kappa A \Delta T)t}{L}. \tag{2.7}$$

where $A$ is the cross-sectional area of the bar, $L$ is its length, and $\Delta T$ is the difference in temperature between the two ends of the bar. In a material heat can be transported either by conduction electrons (dominant in a metal) or by the lattice phonons. In most materials, both mechanisms contribute to the heat flow simultaneously and will dominate under different conditions and in different temperature ranges. It is obvious that, similar

to electrical conductivity, thermal conductivity can also be affected by scattering processes. The dominating scattering processes are phonon-phonon, phonon-defect, electron-phonon, electron-impurity, and even electron-electron interactions [113].

Both the electrical conductivity and the thermal conductivity at low temperature give rise to an important law known as the Wiedemann-Fraz law [4], where the ratio of these two quantities is given by the following equation,

$$\frac{\kappa}{\sigma} = LT \tag{2.8}$$

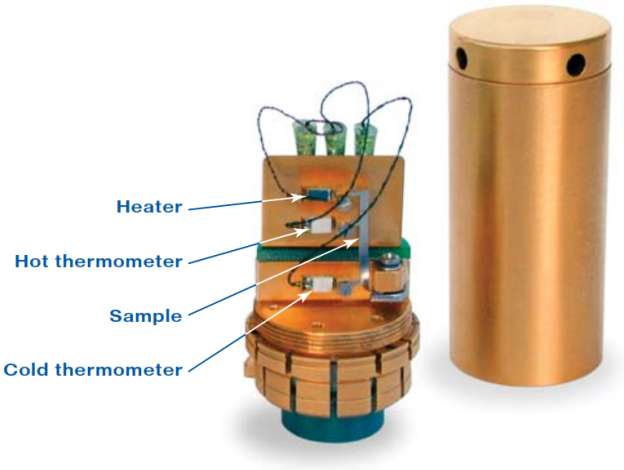


Figure 2.12: The thermal transport puck with radiation shield used in the transient method. [112]

Here, $L$ is a proportionality constant known as the Lorenz number, and for free electrons, it has a value of, $L = 2.44 \times 10^{-8} W\Omega K^{-2}$ and is based on the idea that both the heat and electrical current are transported via free electrons. At a certain finite temperature, a material may no longer obey the Wiedemann-Franz law, and the deviation can be ascribed to various scattering processes and to the phonon contribution to the overall thermal conduction.

Thermal conductivity can be measured either by a steady-state method by maintaining a constant temperature difference across the sample, or by a transient method, where the

thermodynamic response of the sample is measured after the application of a short heat pulse [97]. Using the PPMSs thermal transport option we employed a low-frequency square wave heat pulse to create a temperature gradient across the sample, and then the response was measured.

- **Thermodynamic Properties**
  - Heat Capacity:

The temperature and field dependence of a materials specific heat capacity is another important characterization measurement [113]. It is defined as the energy needed to change the temperature of a sample by a unit amount $\Delta T$,

$$C = \frac{Q}{\Delta T} \tag{2.9}$$

Here, $C$ is the heat capacity, $Q$ is the heat required, and $\Delta T$ is the temperature difference. Since changing the temperature of the material requires either the absorption or the release of energy, a measurement of the heat capacity can provide information on phase transitions in the system. Thus, sharp anomalies or bumps in the specific heat data are usually indicative of a phase transition [113]. The temperature dependence of the specific heat follows characteristic trends for different kinds of excitations. The lattice vibrations or phonons usually contribute more to the heat capacity above a finite temperature and follow a power law behavior, which is also known as the Debye model [4],

$$C \simeq 1944[\frac{T}{\theta_D}]^3 \simeq \beta T^3. \tag{2.10}$$

where $\theta_D$ is the Debye temperature, and $\beta$ is a characteristic coefficient unique to the material and the formula above is useful at low temperatures. For metals, the heat capacity can be described by the free electron gas model, which predicts a linear temperature dependence. Thus, combining the phonon and electron contributions to the specific heat

capacity gives the following:

$$C = \gamma T + \beta T^3 \tag{2.11}$$

Here, $\gamma$ is the Sommerfeld coefficient, whose value provides an indication of the carriers effective mass, which is an important concept that depends on scattering interaction processes [4], and also explains the discrepancy between the theoretical and experimental values of heat capacity in materials. Due to the several interaction and scattering processes mentioned before, the quasi-particle mass in some materials can be 1000 times heavier than the free-electron mass, and these types of materials are known as heavy fermions.

At low temperatures ($\mathrm{T} < \theta_D$), apart from the charge carrier contribution, several other processes can contribute to the overall heat capacity, such as magnon and nuclear Schottky contributions. In a magnetic field (applied or internal), due to the Zeeman effect, the energy levels of a nucleus with spin $I$ can split into $2I+1$ levels, i.e. the moment associated with the spin can orient themselves into $2I+1$ ways. This introduces an anomaly in the heat capacity known as the Schottky upturn, which is due to the magnetic moments at very low temperatures and contributes a finite $\delta \mathrm{T}^{-2}\ e^{T_s/T}$ amount [113] to the overall heat capacity. Thus, for a magnetic system, the total heat capacity at temperature $T$, where the energy splitting $\Delta$E is small compared to the thermal energy $k_B$T, can be expressed as

$$C = \gamma T + \delta T^{-2} e^{T_s/T} + \beta T^3. \tag{2.12}$$

At very low temperature, such as $T < 1$ K , only the first two terms in Eq. 2.12 are required to describe the heat capacity, since the lattice vibrations (phonons) are essentially frozen out [113].

The heat capacity was measured in high vacuum using a $^3$He system from 0.3 K to 300 K. There were also options for application of magnetic field up to 9 T in the PPMS. A time relaxation method was used to measure the specific heat capacity, and the addenda

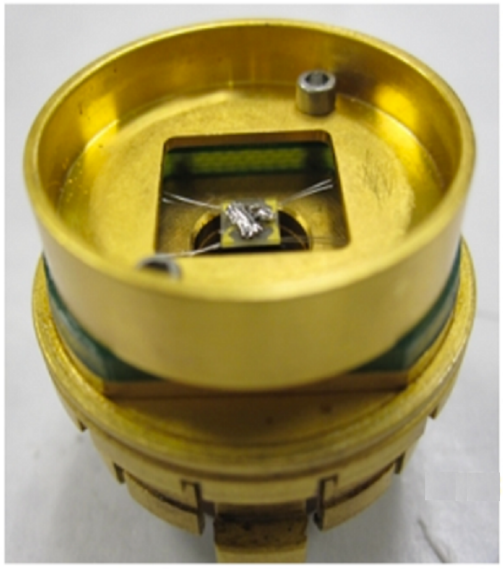

Figure 2.13: The heat capacity measurement puck using the time-relaxation method [97]

was subtracted Fig. 2.13. The PPMS's automated system then calculates the heat capacity through careful analysis of the measurements using a sophisticated model [114]. The data then are further analyzed by using the models described previously.

- **Magnetization Measurements**

The magnetic behavior i.e. the response of a material with respect to an applied magnetic field, mostly emanates from its unpaired electrons. In general, any material can be classified by any of the four basic magnetic categories, such as diamagnetic, paramagnetic ferromagnetic, or antiferromagnetic. All materials have a diamagnetic component to their magnetization, which is the result of electrons in atomic orbits setting up induced currents to oppose (negative magnetization) the external field. However, in many materials other contributions to the magnetization will dominate. In metals and doped semiconductors, for example, some spins align along the field direction and give rise to a positive contribution, and are thus paramagnetic. In the case of atoms with moments that are non-interacting, their susceptibility $\chi$ follows the Curie law [115]

$$\chi = \frac{M}{H} = \frac{C}{T} \tag{2.13}$$

.

Here, $M$ is the magnetic response of the material, i.e. the magnetization to the applied field $H$, and $C$ is the Curie constant given by

$$C = \frac{N_A(g\mu_B)^2}{3K_B}J(J+1) \tag{2.14}$$

,

where $N_A$ is the electron density, $\mu_B$ is the Bohr magneton, $g$ is the Lande $g$- factor, and $J$ is the size of the moment [115]. The spins tend to align with the applied magnetic field direction as the temperature of the material is reduced, and below a certain temperature (Curie Temperature $T_c$), in some magnetic materials, the moments all spontaneously align in parallel to (along) the field. This is known as ferromagnetic ordering. An abrupt anti-parallel configuration is also common and known as antiferromagnetic ordering, where the transition temperature is known as the Neel temperature, $T_N$. In both of these magnetic orientations, the moments are correlated with each other through exchange interactions [4]. For interacting systems which result in collinear, or even more complex magnetism, the Curie law is expressed with a correction known as the Weiss molecular field correction, and the magnetization above the transition temperature can be described by [4, 115],

$$\chi = \frac{C}{T-\theta_w} + \chi_0 \tag{2.15}$$

.

Eq. 2.15 is known as the modified Curie-Weiss law. Here, $C$, which is the Curie constant, and $\theta_w$, which is the Weiss constant (temperature), provide information on the size of the moment and type of exchange interaction, respectively. $\chi_0$ is an experimental correction to the susceptibility data which often contains the paramagnetic contribution from the conduction electron i.e. the temperature-independent Pauli-paramagnetic contribution as well as Landau contribution.

Magnetic measurements, such as field-dependent magnetization, as well as magnetic susceptibility, can provide a comprehensive picture on the magnetic state of a system. From susceptibility data - using the Curie-Weiss law - the nature of magnetic interactions can be understood. For example, the sign of $\theta_w$ provides information on the nature of the magnetic exchange interaction. When $\theta_w$ is zero, the system is paramagnetic. If its positive, then ferromagnetic exchange interactions dominate, and antiferromagnetic wins if the sign is negative. A refined Curie constant can provide us with the effective moment, $\mu_{eff}$, of the material which is derived as [4],

$$C = \frac{N\mu_B^2\mu_{eff}^2}{3K_B}. \tag{2.16}$$

The magnetic measurements for this dissertation work have been performed on the PPMS and in a Quantum Design Superconducting Quantum Interference Device (SQUID-MPMS). A SQUID provides some advantages over the PPMS, such as two orders of magnitude greater sensitivity, which was useful for small single crystals and low-moment samples. The sample was weighed and inserted into the sample chamber of the PPMS or SQUID using a plastic drinking straw. The straw is used, since it has a very low magnetic background. The sample chamber was then cooled down to base or the desired temperature in zero applied field (ZFC) and then a certain constant field was applied. The magnetization was then measured as a function of temperature upon warming ($M$ vs $T$, or $\chi$ vs $T$ curves). The hysteresis, or field-dependent measurement, was also performed at a fixed temperature by varying the applied field and measuring the magnetic response of the sample. In the PPMS, the ACMS option was used to do the magnetic measurements, where the magnetometer is a Faraday-extraction type, in which the sample is quickly pulled in and out ($\sim$ 1 m/s) of a set of detection coils. This movement induces a voltage that is directly proportional to the magnetic moment of the sample. The induced voltage signal is analyzed using a digital signal processor (DSP) to determine the magnetic moment of the sample relative to a calibrated standard [97].

# Chapter 3
# Complex Superconductivity of $Re_6Zr$

## 3.1 Introduction

In this chapter the NCS superconductor $Re_6Zr$ will be discussed in detail. A concise version of this work has already been published in *Physical Review B* (PRB) and can be found in Ref. [54]. Since the discovery of superconductivity in $CePt_3Si$ [18], the topic of superconductivity in systems lacking spatial inversion symmetry has undergone a resurgence, and many superconducting materials that were known to be NCS superconductors came to the forefront. The search for new NCS superconductors is also a major part of the research efforts in the study of the effects of broken symmetries. As discussed previously in the first chapter, broken inversion symmetry in some NCS superconductors invokes strong antisymmetric spin-orbit coupling (ASOC) which might significantly exceed the superconducting energy gap, pre-empting pairing between ASOC-split bands, which results in mixed singlet-triplet states [17, 19, 20]. If the triplet component is significant, the superconducting gap may become highly anisotropic, and develop line or point nodes [23–26]. It is important to note that there is no symmetry requirement for gap anisotropy in NCSs. Strong anisotropy is rare in such materials [21, 42, 51], and most frequently it appears from the projection of the pairing interaction onto the ASOC-split bands, as, for example, in $Li_2Pt_3B$ [116]. In addition to nodes, the consequence of a triplet or antisymmetric (and in some cases symmetric d-wave) pairing component can break time reversal symmetry (TRS) (a non-zero angular momentum from the cooper pairs) in the superconducting state [117]. The superconducting pairing state can also be further classified in terms of the corresponding gap function, which is given by the irreducible representations of the point group associated with a given crystal symmetry. Moreover, some irreducible representations might break TRS due to the symmetry of that representation [117]. A comprehensive analysis of the point group representation of the crystal lattice symmetry is beyond the scope of

this dissertation, and we shall only utilize the published data and explanation used by the authors of this article [118] for $Re_6Zr$.

Very recently, muon spin relaxation ($\mu$SR) measurements on two NCSs, $LaNiC_2$ [119] and $Re_6Zr$ [17], indicated TRS breaking in both of these systems by detecting the appearance of a spontaneous magnetic field at the onset of superconductivity. So far only a handful of unconventional superconductors, e.g. $Sr_2RuO_4$ [120, 121], $UPt_3$, (U,Th)$Be_{13}$ [122, 123], (Pr,La)(Os,Ru)$_4Sb_{12}$ [124], $PrPt_4Ge_{12}$, and $LaNiGa_2$ [125, 126] were found to exhibit this property. $LaNiC_2$ and $Re_6Zr$ are the only two NCSs to date that show evidence for TRS-broken states. Generally, since the ASOC has the full symmetry of the lattice, absence of inversion symmetry by itself cannot lead to the TRS breaking: strong electron-electron interactions and/or an unconventional pairing mechanism are required to stabilize such a state. Indeed, it was suggested that a purely-triplet state emerges in $LaNiC_2$ due to electron-electron correlations allowing the TRS breaking[119]. Similarly, if $Re_6Zr$ supports the TRS state, as is indicated by the $\mu$SR measurements [17], it must be due to an unconventional pairing mechanism. For such a mechanism the gap anisotropy is required by symmetry, and the pairing states suggested in Ref. [17] indeed possess either line or point nodes. While at present there is no other corroborating evidence available for TRS breaking, we investigate the possible consequences of it on the superconducting properties. Even though superconductivity in $Re_6Zr$ was first reported in 1961 [127], there have been no comprehensive studies of the electronic structure and physical properties at low temperature, which motivated us to investigate this interesting compound in detail.

In this section we present the synthesis, characterization, electronic band structure, resistivity, heat capacity, thermal conductivity, and low-temperature penetration depth of $Re_6Zr$, along with results from chemical doping and physical hydrostatic pressure measurements. Thermal and penetration depth measurements are very useful in providing information on the nature of the pairing state and on electron-electron interactions. In conventional BCS-like superconductors, the thermal conductivity, $\kappa(T)$, decreases below

$T_c$ [128]. However, in unconventional superconductors (non BCS-type), such as strongly correlated systems, high $T_c$ cuprates, and iron pnictides, the thermal conductivity often increases upon cooling below $T_c$ [129–134]. For example, it was suggested that over-doped samples in Co-doped $BaFe_2As_2$ show an enhancement in the electronic contribution to their thermal conductivity below $T_c$, due to an increase in the quasiparticle mean free path and the presence of a nodal gap structure [135]. More recent measurements on the same system attribute the enhancement in thermal conductivity to the formation of a spin gap with a reduction in electron scattering from magnetic spin fluctuations [131]. At low temperatures, $T \ll T_c$, the behavior of the electronic thermal conductivity, heat capacity, and the penetration depth carry information about the nodal structure of the gap.

The structure of $Re_6Zr$ is $\alpha$-Mn, cubic with space group $I\bar{4}3m$. The unit cell has 58 atoms that occupy four distinct crystallographic sites. A recent study [17] showed bulk $Re_6Zr$ has a superconducting transition of 7 K. From measurements performed in this work, several superconducting parameters, such as the coherence length ($\xi$), penetration depth ($\lambda$), and the upper critical field ($H_{c2}$) were estimated. $H_{c2}$ is important for NCS superconductors, since its value in comparison with the Pauli limiting field can suggest the existence of a triplet component to the pairing. We also performed specific heat measurements, which verified a bulk superconducting transition. Thermal conductivity showed an enhancement in the electronic contribution below $T_c$, very similar to that observed in Co-doped $BaFe_2As_2$. The enhancement in the thermal conductivity is suppressed with the application of an external magnetic field. Our results at low temperature do not give evidence for the existence of nodal quasiparticles, and are most consistent with a fully-gapped superconductor. While it is possible that the contribution of the excitations from linear point nodes is sufficiently small to be compatible with the data, we do not find good evidence for line nodes. This result severely restricts the possible order parameters for $Re_6Zr$.

## 3.2 Experimental Description

Polycrystalline samples of $Re_6Zr$ were made by arc melting about 1 g of stoichiometric amounts of pure Zr slug (99.99% Alfa Aesar) and Re slug (99.99% Alfa Aesar) under a partial pressure of UHP-Ar gas on a water-cooled copper hearth with a tungsten electrode. After melting, the starting materials form a button when cooled. The button of $Re_6Zr$ was then flipped several times and remelted to ensure a homogeneous sample by a congruent mixtures of the constituent elements. Mass loss during the synthesis was negligible, and after flipping and remelting the sample 3-4 times, it formed a uniform and hard button. Several off-stoichiometric samples were made to check the effect of stoichiometry on $T_c$. We also synthesized and studied samples doped with Hf, Ti, W, and Os to check the effect of chemical doping on $T_c$.

The crystal structure and phase purity of the arc melted samples were investigated by powder X-ray diffraction (XRD) using a small portion of powdered sample on a PANalytical Empyrean multi-stage X-ray diffractometer with Cu K$\alpha$ radiation ($\lambda = 1.54$ Å). The system has a $\theta$-$2\theta$ geometry, and data were taken from 10° to 90° at a constant scan of 2° per minute at room temperature. Elemental composition was determined with a JSM-6610LV high performance scanning electron microscope (SEM) equipped with an energy-dispersive spectrometer (EDS).

The electrical resistivity was measured using a standard four-probe ac technique at 27 Hz with an excitation current of 1-3 mA, in which small diameter Pt wires were attached to the sample using a conductive epoxy (Epotek H20E). Data were collected between 1.8 to 290 K and in magnetic fields up to 9 T using a Quantum Design, Physical Property Measurement System (PPMS). The specific heat was measured in the PPMS using a time-relaxation method between 2 and 20 K at 0 and 9 T. Magnetic susceptibility was also measured in the PPMS in a constant magnetic field of 30 Oe; the sample was zero-field-cooled (ZFC) to 1.8 K, and then magnetic field was applied, followed by heating to 10 K and then cooled down again to 1.8 K [field-cooled (FC)]. The low temperature upper

critical field was measured in a 35 T resistive magnet at the National High Magnetic Field Laboratory (NHMFL) using a four-probe ac technique with a 3 mA excitation current. The thermal conductivity was measured with the PPMS's thermal transport option, which uses a low-frequency square-wave heat pulse to create a temperature gradient across the sample.

The temperature dependence of the superconducting penetration depth was measured in a $^3$He fridge with a 9-T magnet at Ames Laboratory using a tunnel-diode resonator (TDR) oscillating at 14 MHz and at temperatures down to 0.5 K. Here, the TDR is a tunnel diode coupled with a tank circuit i.e. an L-C circuit. The tank circuit determines the resonant frequency for the tunnel diode oscillation utilizing the negative resistance regime of the diode. The whole assembly then acts as a cavity resonator in the radio-frequency (rf) or microwave frequency regime, and thus is suitable for high frequency operations [136, 137]. When a non-magnetic conductor is placed inside the cavity (coil of the tank circuit), it causes a change in the resonant frequency of the TDR assembly. Thus, by putting a superconducting material inside the coil, the resonant frequency will be changed due to the rf magnetic susceptibility i.e. the change in penetration depth $\lambda$ of the superconducting material [137]. This change in frequency was carefully resolved up to an order of $10^{-9}$ in a few seconds of counting time. Typically a very small piece of the sample to be studied is coated with a thin aluminum (Al) layer and mounted on a sapphire rod, where the temperature of the rod can be independently tracked, and thus the variation of the sample temperature can be isolated from the oscillator circuit temperature [137]. The rod is then inserted into the inductor coil of the tank circuit. This provides a stable temperature variance of about $\pm$ 1 mK throughout the measurement process [138]. A small ac magnetic excitation or drive field, $H_{ac}$ (usually $<$ lower critical field, $H_{c1}$) of 20 mOe is used to ensure that no vortices are created, and only the London penetration depth is measured [138]. Further details of the measurement and calibration can be found in these[136–138] references.

Measurement of the transition temperature under applied hydrostatic pressure ($P$) was carried out in a commercial BeCu cylindrical pressure cell (Quantum Design) within a Magnetic Properties Measurement System (Quantum Design, MPMS SQUID magnetometer). Daphne 7373 oil was used as the pressure-transmitting medium. The value of the applied pressure was calibrated by measuring the shift of the superconducting transition temperature of Pb, which was used as a reference manometer ($T_c$ of Pb is $\sim$ 7.19 K at ambient pressure)[139].

## 3.3 Result and Discussion

### 3.3.1 Characterization of Crystal and Electronic Band Structure

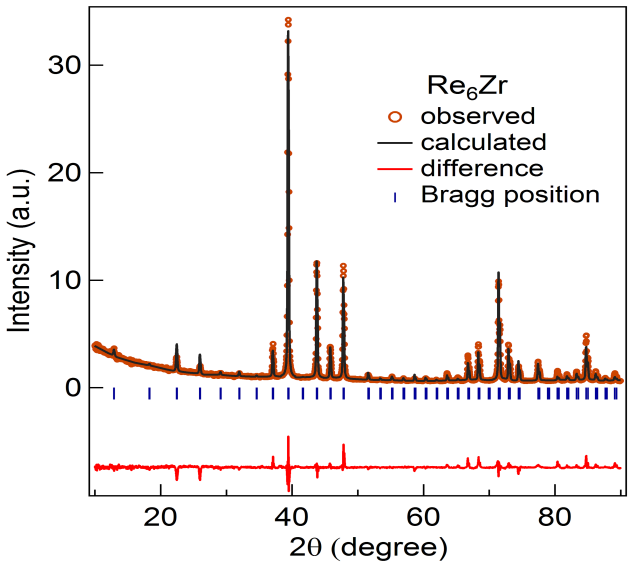


Figure 3.1: Powder XRD pattern (open circles) of $Re_6Zr$ at room temperature. The solid line represents the Rietveld refinement fit calculated for the $\alpha$-Mn cubic-type structure with space group I$\bar{4}$3m. The Red solid curve at the bottom describes the difference between the experimental and calculated patterns.

The XRD pattern of polycrystalline $Re_6Zr$ is shown in Fig. 3.1. Data taken on the Panalytical instrument were then further analyzed by Rietvelt refinement using the powder diffraction pattern analysis software Full Prof [109]. The refinement indicates that the sample was single phase with a cubic cell parameter of $a = 9.6989 \pm 0.0002$Å, which is in good agreement with published data [17]. A schematic view of the crystal structure

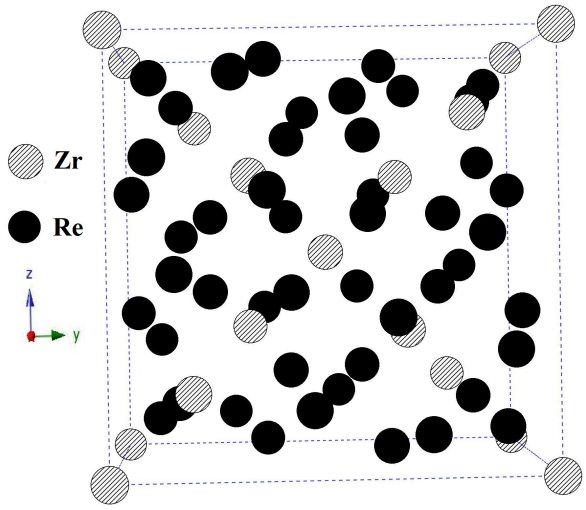


Figure 3.2: A schematic view of the crystal structure of $Re_6Zr$.

is shown in Fig. 3.2. The compound $Re_6Zr$ forms in the $\alpha$-Mn cubic structure with the primitive Bravais lattice $I\bar{4}3m$ (space group 217). This particular structure lacks a center of inversion. SEM data, utilizing EDS, confirmed the atomic ratio is approximately 6:1.

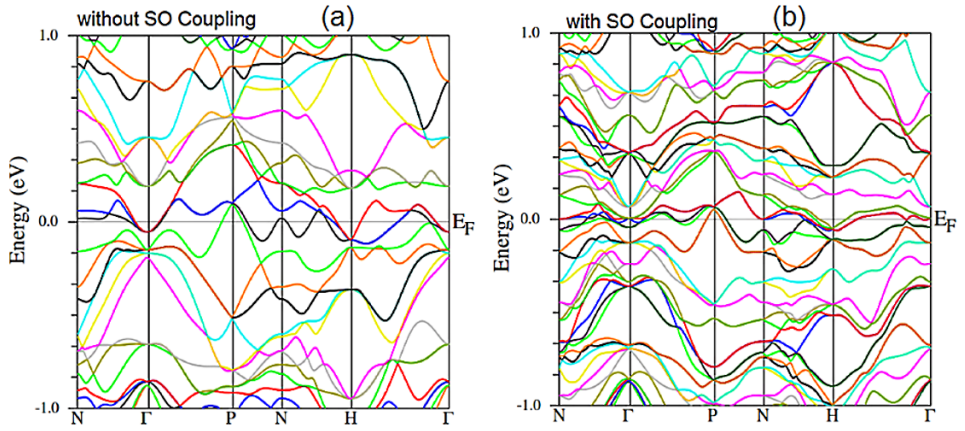


Figure 3.3: Section of the calculated electronic band structure of $Re_6Zr$ (a) without SO coupling along high symmetry directions within the range of $\pm$ 1 eV around $E_F$. (b) Section of the calculated electronic band structure with SO coupling. The Band splitting due to SO coupling is about 30 meV.

The electronic band structure of $Re_6Zr$ was calculated using the WIEN2K full-potential linearized augmented plane wave (LAPW) software package [140] using the Generalized Gradient Approximation exchange-correlation potential [141]. The room temperature lat-

tice constant of 9.6989 Å was used, and the cutoff in the LAPW basis was varied from $RK_{\max} = 7.00$ to $RK_{\max} = 8.00$ to ensure convergence. A $19 \times 19 \times 19$ mesh of points was used for the Brilluoin zone integration that employed the modified tetrahedron method. One set of calculations was done omitting the SO interaction for the valence bands. A second set of self-consistent calculations included the SO interactions for the valence bands using a scalar relativistic approximation.

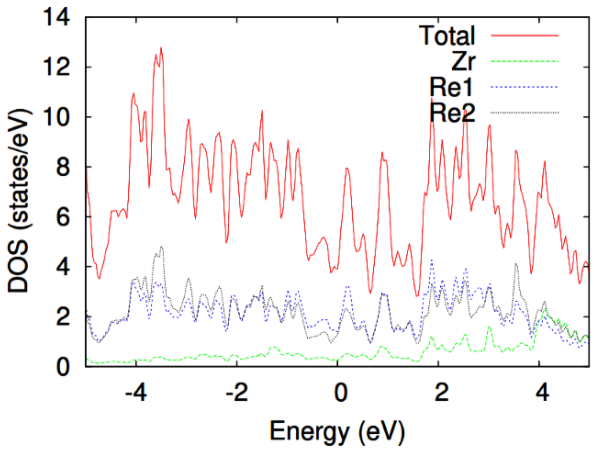


Figure 3.4: Section of the total and individual atom-projected DOS (in units of states $eV^{-1}$) of $Re_6Zr$ within the $\pm 4$ eV energy range around $E_F$. Result here is shown without SO coupling.

The results of these calculations are presented in Fig. 3.3(a) for the band structure calculated without taking the SO coupling into consideration and in Fig. 3.3(b), with SO coupling. The total density of states (DOS) is shown in Fig. 3.4. From the band structure plots, commonly referred to as *spaghetti plot*, multiple bands are observed to cross through the Fermi level. The DOS near the Fermi level is almost entirely composed of Re and Zr $d$ bands, however, since the ratio of Re to Zr is 6:1, the Re-$d$ bands comprise the majority of the states. There are 4 bands at $\Gamma$ about 0.2 eV below the Fermi surface, as seen in Fig. 3.3, and two of them look like a Dirac point. SO coupling lifts the bands very close to the Fermi level and splits the spin degeneracy, which can be seen in Fig. 3.3(b). The band splitting due to the SO interaction is about 30 meV and is comparable to that of $Li_2Pd_3B$ [18]. Its worthwhile to note that the band splitting due to ASOC in $Li_2Pt_3B$ is

about 200 meV, and it has an anisotropic superconducting gap [18, 116], while $Li_2Pd_3B$ has a fully-gapped isotropic order parameter.

### 3.3.2 Electrical Resistivity

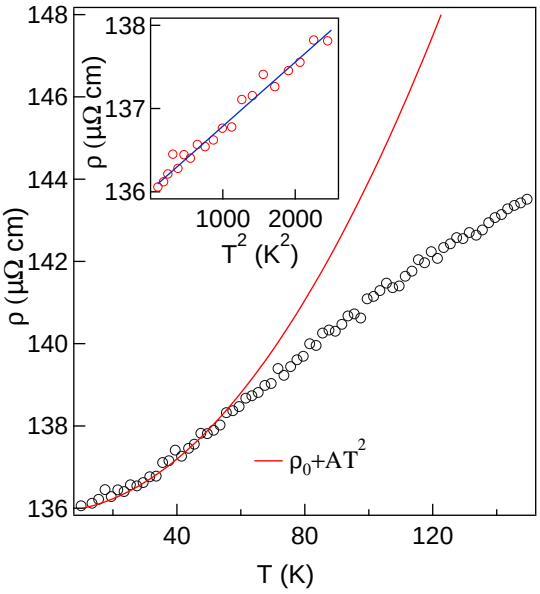


Figure 3.5: Normal state temperature dependence of the electrical resistivity of $Re_6Zr$. The solid line is a fit to the data as discussed in the text. Inset shows the data between 10-50 K, and the blue solid line indicates a linear fit to the data.

The normal state temperature dependence of the resistivity of $Re_6Zr$ between 10 K and 150 K is shown in Fig. 3.5. The resistivity is metallic, and an inflection point in $\rho(T)$ at $\approx$ 50 K is observed. The normal state resistivity ($\approx$ 150 $\mu$ $\Omega$ cm at room temperature) is typical of polycrystalline metallic materials. The residual resistivity ratio (RRR), $\rho_{290K}/\rho_0$ $\sim$ 1.1, is small, which suggests that the transport in the sample is dominated by disorder. The low temperature resistivity data were fit as shown in the Fig. 3.5 to the power law,

$$\rho = \rho_0 + AT^{\alpha}. \tag{3.1}$$

Here, $\alpha = 2$, the residual resistivity $\rho_0 \approx 135$ $\mu$ $\Omega$ cm, and the coefficient $A = 0.0079$ $\pm$ 0.0002 $\mu$ $\Omega$ cm/K$^2$. The fit describes the data reasonably well between 10 and 50 K, suggesting a Fermi-liquid like temperature dependence at low temperature in the normal

state.

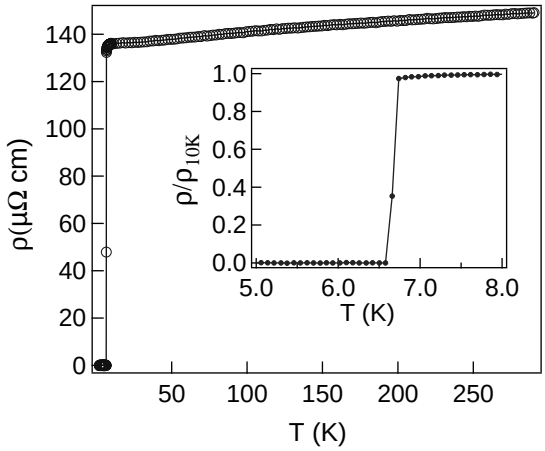


Figure 3.6: Temperature dependence of the electrical resistivity of $Re_6Zr$ from 2 K to 290 K with the inset showing a sharp superconducting transition at 6.7 K.

The value of $\rho_0$ is large, most likely due to the polycrystalline nature of the sample. The Kadowaki-Woods ratio [142] (KWR) $A/\gamma^2$, where $\gamma$ is the Sommerfeld coefficient, is taken as a measure of the degree of electron correlations in the material. From the heat capacity data, $\gamma$ was estimated as 27.5 mJ mol$^{-1}$K$^{-2}$, and the KWR was found to be $A/\gamma^2 \approx 10.44$ $\mu\Omega$ cm mol$^2$ K$^2$ J$^{-2}$. This KWR value is typical of heavy fermions and suggests $Re_6Zr$ is a strongly correlated electron system[142, 143]. The temperature dependent resistivity from 2 to 290 K is shown in Fig. 3.6. A sharp superconducting transition is observed at 6.7 K (inset Fig. 3.6). The 90% to 10% transition of the resistivity value width is less than 0.05 K indicating very good assessment of the transition temperature.

### 3.3.3 Magnetization and Upper Critical Fields

Apart from the transition to a zero resistance state, the Meissner effect i.e. perfect diamagnetism is a telltale signature of superconductivity. The ZFC and FC temperature dependent magnetic susceptibility data are shown in Fig. 3.7 Measurements were performed at 30 Oe in a temperature range from 1.8 K to 10 K. The onset of diamagnetism occurs near 6.6 K, which is in agreement with the transport data. The ZFC data show a large, negative volume susceptibility of near $-1$ at low temperature, indicating bulk superconductivity. A

perfect Meissner fraction corresponds to $4\pi\chi = -1$. Several small odd-shaped pieces of sample were measured, and the data were not corrected for demagnetization effects.

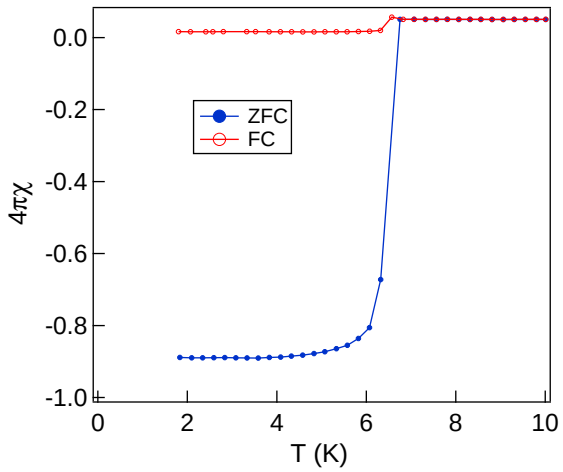


Figure 3.7: ZFC and FC susceptibilities for $Re_6Zr$ at a constant field of 30 Oe. The value of the ZFC volume susceptibility data at low temperatures indicates bulk superconductivity.

The upper critical field was calculated by applying a variety of magnetic fields up to 9 T to the same sample in the PPMS and measuring the shift in $T_c$. The transition temperatures at higher fields were measured in a 35 T resistive magnet at the NHMFL. For these measurements, temperatures were as low as 0.32 K, and critical fields at different temperatures up to 2 K were investigated. At all applied fields, a sharp superconducting transition was observed as shown in Fig. 3.8.

As expected, $T_c$ shifts to lower temperature as the field increases, and the transition gets broader. Superconductivity remains above 2 K for an applied field of 9 T (in the PPMS data [Fig. 3.8(a)]), which indicates a large upper critical field and is consistent with data from NHMFL [Fig. 3.8(b)]. Using the midpoint resistivity i.e. 50% drop in resistivity from its normal state value, the upper critical field is plotted as a function of transition temperature, $T_c$. The variation of $H_{c2}$ with $T_c$ is approximately linear with a negative slope, without showing any saturation for applied fields as high as 9 T. Below 2 K to 0.32 K and above 9 T, $H_{c2}$ shows slight saturation which can be seen in Fig. 3.9. The upper critical field can be estimated by fitting the data with the empirical Ginzburg-Landau (GL)

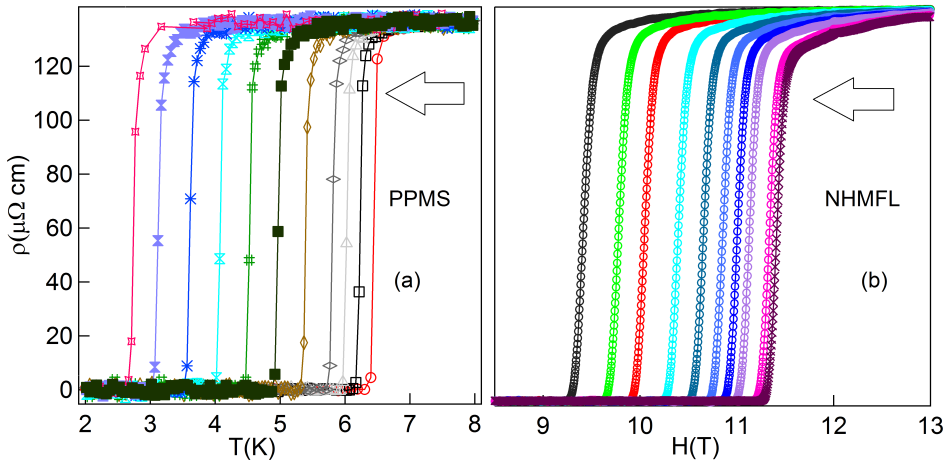


Figure 3.8: Upper critical field of $Re_6Zr$ as a function of temperature. The transition temperatures were taken from the midpoint of the resistivity drop from the normal state, as seen in (a) and (b). In the left upper panel (a), the behavior of the transition temperature under applied fields of 0, 0.5, 1, 1.5, 2, 3, 4, 5, 6, 7, 8, and 9 T is shown from right to left, respectively. On the right side of plot (b), the critical fields at different temperatures down to 0.32 K are shown, which were measured at the NHMFL.

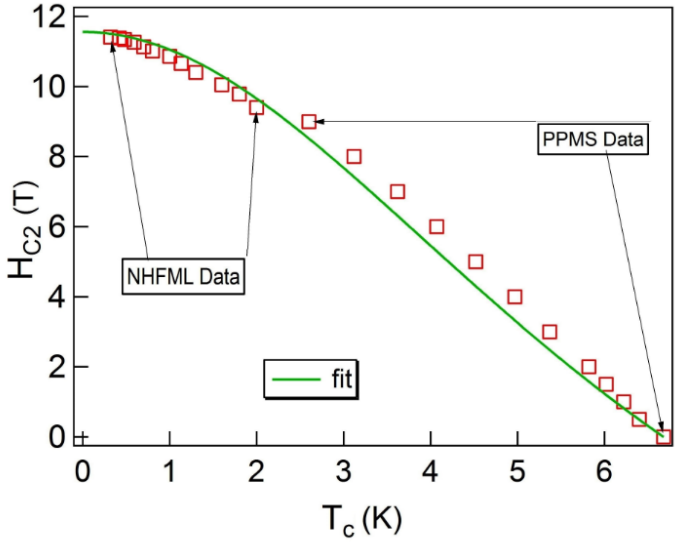


Figure 3.9: Upper critical field of $Re_6Zr$ as a function of the transition temperatures determined from Fig. 3.8. The solid line is the fit to Eq. 3.2, as described in the text.

formula [144],

$$H_{c2}(T) = H_{c2}(0)\frac{(1-t^2)}{(1+t^2)}, \tag{3.2}$$

with $t = T/T_c$, and $T_c$ is the transition temperature at zero applied field. The fit, which is shown in Fig. 3.9, gives a value of 11.6 ± 0.1 T. This value is close to the Pauli limiting field of $1.83T_c$, which is 12.22 T.

For a superconductor in the dirty limit, the orbital limit of the upper critical field is given by the Werthamer-Helfand-Hohenberg (WHH) [145, 146] expression,

$$\mu_0 H_{c2}(T) = -0.693\mu_0 T_c \frac{dH_{c2}}{dT_{T_c}}, \tag{3.3}$$

where $\mu_0\ H_{c2}(0)$ was estimated using the data range from $T = T_c$ to $T_c/3$. From the slope $\mu_0(\mathrm{d}H_{c2}/\mathrm{dT}) \approx -\ 2.31 \pm 0.04$ T/K, and using $T_c = 6.68$ K, we found $\mu_0\ H_{c2}(0) = 10.65 \pm 0.02$ T, which is slightly smaller than the value reported by Singh [17] *et al.*

Thus, the upper critical field is large and comparable to both the Pauli and orbital limiting fields. This large upper critical field can originate from strong coupling, SO scattering [147, 148], or from a triplet pairing component in $Re_6Zr$, as well as a combination of all of them.

If we assume the upper critical field to be purely orbital, the superconducting coherence length ($\xi$) can be calculated using $H_{c2}(0) = \Phi_0/2\pi\ \xi\ (0)^2$, where $\Phi_0 = \frac{h}{2e} = 2.0678 \times 10^9$ OeÅ$^2$ is the flux quantum[144]. From this we found $\xi(0) = 53.3$ Å, for $H_{c2}(0) = 11.6$ T. Similarly, from the relation $H_{c1}(0) = (\Phi_0/4\pi\ \lambda^2)\ln(\lambda/\xi)$, using 8 mT as $H_{c1}$, which was reported in this ref [118], the magnetic penetration depth was found to be, $\lambda(0) = 3696$ Å. The Ginzburg-Landau parameter is then $k = \lambda/\xi = 69.3$. The upper critical field and Pauli limiting field closely follow the relation $H_{c2}(0)/H_{\mathrm{Pauli}} = \alpha/\sqrt{2}$. The Maki parameter was found to be $\alpha = 1.34$. The sizable Maki parameter obtained is an indication that Pauli pair-breaking is non-negligible [149]. Thus, an anisotropic study of the upper critical field in a single crystal would provide greater evidence for it exceeding the Pauli limit, where the momentum-space dependence of the SO coupling could be studied[24]. If it is found to be the case, the result would suggest a substantial contribution from a spin triplet component

to the pairing mechanism[18, 150].

### 3.3.4 Thermal Conductivity

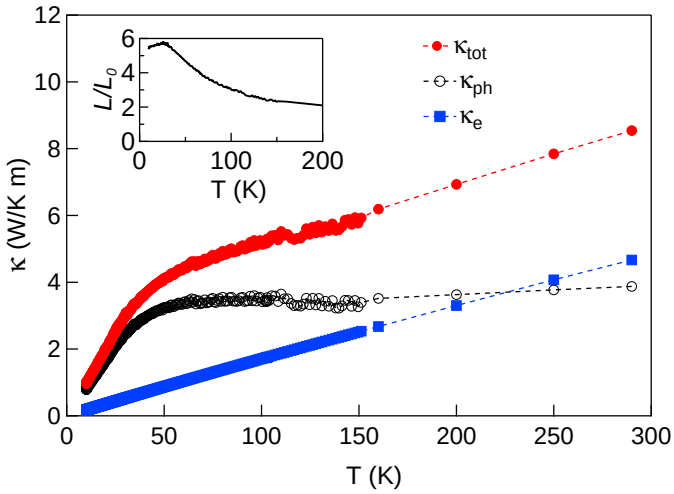


Figure 3.10: Thermal conductivity of $Re_6Zr$ above 10 K. The main panel shows the total, phonon, and electronic contributions to the thermal conductivity. The dashed lines are guides to the eye. Inset: Temperature dependence of the reduced Lorenz number.

We measured thermal conductivity from room temperature to down to 2 K, with and without applied magnetic field. The zero-field data above 10 K are shown in Fig. 3.10. A greater density of data points was taken below 150 K. The total thermal conductivity has a room temperature value of about 8.5 W/K m, which is comparable to other metallic alloys. We have assumed that the total thermal conductivity ($\kappa_{\rm tot}$) is composed of a lattice, or phonon contribution ($\kappa_{\rm ph}$), and a conduction electron contribution ($\kappa_{\rm e}$), which depends both on the temperature and carrier concentration. The electronic contribution to the thermal conductivity was estimated using the Wiedemann-Franz law described by Eq. 3.4, which assumes the energy/momentum relationship is given by a single parabolic band i.e. free electrons.

$$\kappa_{\rm e} = \frac{L_0 T}{\rho} \tag{3.4}$$

Here, $L_0 = 2.45 \times 10^{-8}$ W $\Omega$ K$^{-2}$ is the Lorenz number. The phonon contribution was then estimated from $\kappa_{\rm ph} = \kappa_{\rm tot} - \kappa_{\rm e}$. As shown in Fig. 3.10, $\kappa_{\rm e}$ increases proportionally with temperature, whereas $\kappa_{\rm ph}$ remains approximately constant above 50 K.

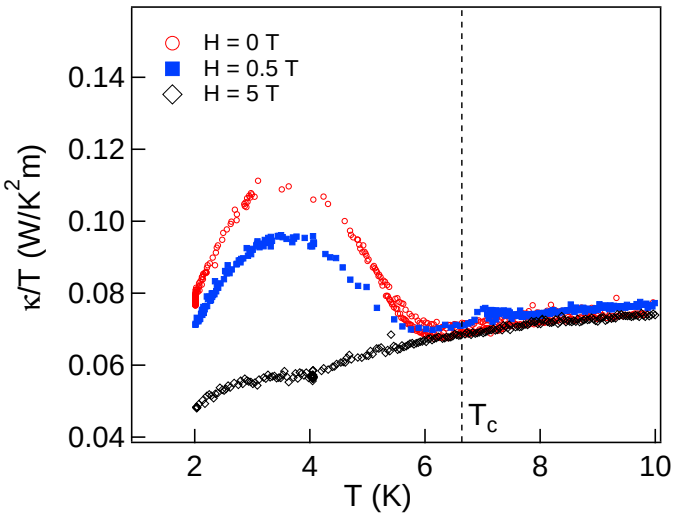


Figure 3.11: Low temperature thermal conductivity of $Re_6Zr$ in different magnetic fields, showing the enhancement below $T_c$ and the suppression with magnetic field. The vertical dashed line indicates $T_c$ at zero field.

The temperature dependence of the reduced Lorenz number ($L/L_0$) is shown in the inset of Fig. 3.10. Here, $L = \frac{\kappa_{\rm tot}\rho}{T}$. The reduced Lorenz number increases rapidly below 100 K with decreasing temperature and obtains a large maximum value of 5.8 at approximately 25 K. These large values of $L/L_0$ are typically observed in heavy fermion compounds, such as $URu_2Si_2$ and $CeCu_4Al$ [151, 152]. If the thermal conductivity were due solely to the electronic contribution, then the reduced Lorenz number would be identically 1, in accordance with the Wiedemann-Franz law. Large values of $L/L_0$ suggest the thermal conductivity is dominated by phonons, especially below 100 K.

Further evidence for a phonon-dominated thermal conductivity in $Re_6Zr$ is shown in Fig. 3.11, where we have plotted the low temperature thermal conductivity below 10 K, which spans the superconducting transition. The thermal conductivity shows no signature of superconductivity at the transition temperature, $T_c$, which is indicated by the dashed vertical line in Fig. 3.11. However, a significant enhancement in $\kappa_{\rm tot}$ occurs below $T_c$. In zero field, the thermal conductivity increases below 6 K and reaches a maximum near 4.5 K. This behavior is typically observed in unconventional superconductors, such as heavy

fermions, iron pnictides, and high-$T_c$ cuprates [131, 134, 151], in contrast to conventional superconducting systems, where the thermal conductivity decreases below $T_c$ due to the loss of the electronic contribution [128].

Many of the unconventional systems contain magnetic elements and order antiferromagnetically. The enhancement in the thermal conductivity is often attributed to a reduction in scattering from spin fluctuations [131]. We do not expect this to be the mechanism responsible for the enhancement in the thermal conductivity in $Re_6Zr$, as it displays standard metallic Pauli paramagnetism below room temperature.

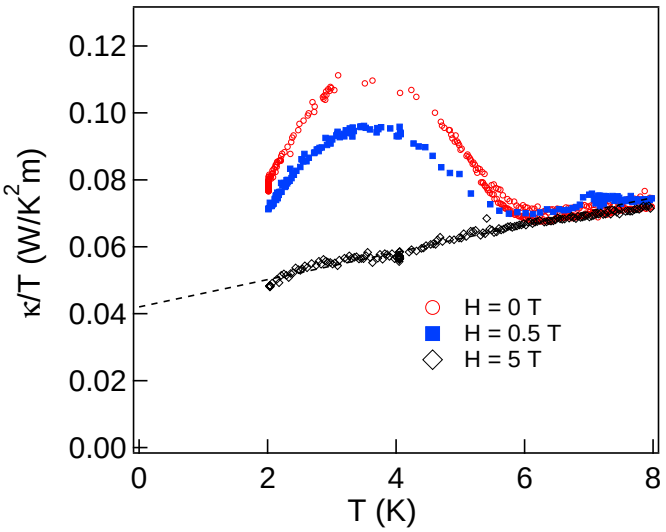


Figure 3.12: Temperature dependence of thermal conductivity $\kappa_{tot}$ below $T_c$. The dashed line is a linear fit to the data.

The enhancement could be electronic in origin, due to the reduction in strong inelastic scattering of electrons, which freeze out with the opening of the superconducting gap. It could also be attributed to the phonon component, as this contribution will increase below $T_c$ due to a rapid decrease in the quasiparticle scattering. However, a reasonable fit of the resistivity to the Fermi-liquid $T^2$ dependence, a small RRR value, and the estimated dominance of the phonon contribution to $\kappa$ at the superconducting transition are in favor of the latter scenario. As shown in Fig. 3.11, the peak in the thermal conductivity is suppressed in the presence of a magnetic field. We interpret the suppression as due to phonon-vortex

scattering in the mixed state ($H_{c1} < H < H_{c2}$), where $H_{c1} \approx 8$ mT [118]. This requires the inter-vortex spacing to be less than the phonon mean free path. Assuming a triangular vortex lattice, the vortex spacing ($a_v$) can be estimated by [1] $a_v = 1.075(\Phi_0/H)^{1/2} \approx 700$ Å, for a field value of 0.5 T. From specific heat and thermal conductivity data, and assuming a reasonable sound velocity of 3500 m/s, the phonon mean-free path is estimated to be $\approx 3000$ Å, which is indeed larger than the vortex spacing, further supporting the notion of the thermal conductivity being dominated by the phonon contribution in zero field.

Usually the low temperature (T $\ll T_c$) thermal conductivity data can show linearity if the gap contains nodes [18]. For $Re_6Zr$, the temperature dependence of $\kappa/T$ is shown in Fig. 3.12. Linear fits (black dashed lines) match the data well below the phonon enhancement peak for zero field and 0.5 T, and to even higher temperatures for the 5 T data, in which the phonon peak has been completely suppressed. A similar linear temperature dependence in $\kappa/T$ was observed in $CePt_3Si$ [30]. While it may be tempting to draw conclusions about the existence of nodes from the extrapolated linear dependence to $T = 0$, this would be misleading, as detailed measurements at much lower temperatures are necessary to determine the behavior of the electronic component of $\kappa/T$.

### 3.3.5 London Penetration Depth

The London penetration depth $\lambda$, is a characteristic response of a superconductor in an applied magnetic field. It refers to the exponentially decaying magnetic field at the surface of a superconductor i.e. the distance within which the field inside a thin layer of the superconductor decreases by the factor [4] $e^{-1}$. From the low temperature behavior of the penetration depth and corresponding superfluid density, information about the pairing symmetry of the superconducting order parameter can be extracted [137, 138]. For example, for high $T_c$ superconductors, Annet *et al.* showed [153] a superconducting gap with line nodes in crystals of tetragonal or orthorhombic symmetry with a spherical or cylindrical Fermi surface will give a linear temperature dependence at low temperature for their penetration depth. Using the TDR method, the temperature dependence of the

London penetration depth has been measured and is shown in Fig. 3.13.

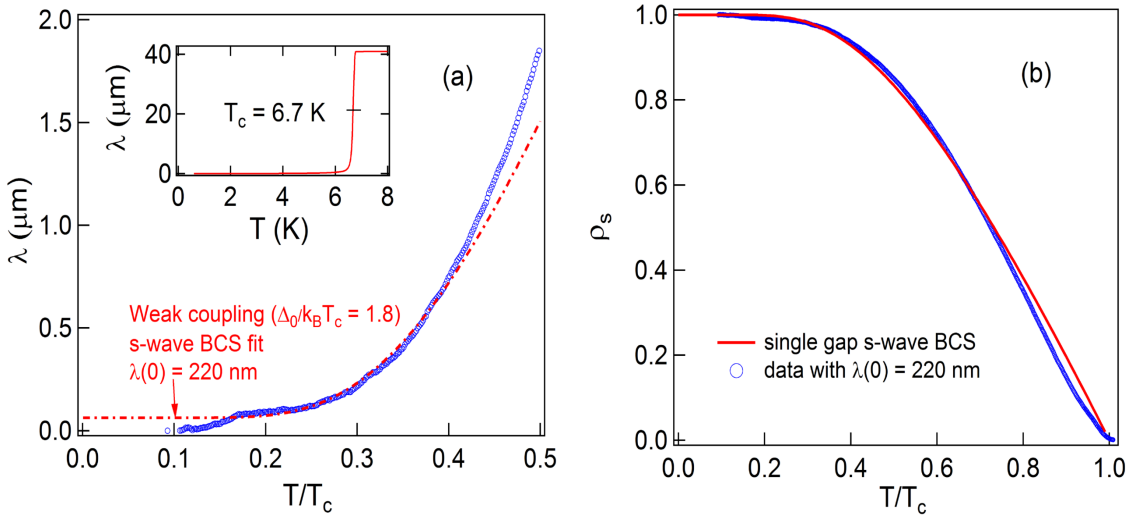


Figure 3.13: Temperature dependence of the London penetration depth (a) and superfluid density (b). The superconducting transition at $T_c = 6.7$ K is shown in the inset of the upper panel. The dotted line in the main body of the upper panel is a BCS fit to the data below $T = T_c/3$, as described in the text. The lower panel shows the corresponding superfluid density, and the solid line is a BCS fit to the data, as described in the text.

A sharp superconducting transition was observed at 6.7 K, which is similar to the value from the resistivity data. In order to determine the structure of the gap, one needs to probe the behavior of $\Delta\ \lambda(T)$ below about $T_c/3$ (2.23 K in the current study). We measured $\Delta\ \lambda(T)$ down to 0.5 K ($\sim$0.07 $T_c$) as seen in Fig. 3.13(a). While a small impurity feature was noticed below 1.1 K (0.16 $T_c$), we were able to observe the clear temperature-independent behavior of $\Delta\ \lambda(T)$ below 0.25 $T_c$ which is consistent with the s-wave BCS fit described by Eq. 3.5.

$$\Delta\lambda(T) \approx \Delta\lambda(0) e^{-\frac{\Delta(0)}{k_B T}} \sqrt{\frac{\pi\Delta(0)}{2k_B T}} \tag{3.5}$$

with $\Delta\ \lambda(0)$=220 nm. This suggests an isotropic superconducting energy gap similar to $Mo_3Al_2C$ [154]. Interestingly, other physical and thermal property studies of $Mo_3Al_2C$, such

as power law behavior in the NMR relaxation rate and absence of a Hebbel-Slichter peak, deviate from the BCS prediction, suggesting the possibility of a nodal superconducting gap in $Mo_3Al_2C$ [150, 155]. In addition, Fig. 3.13(b) shows the corresponding superfluid density of $Re_6Zr$, $\rho_s(T) = (\Delta\,\lambda(0)/\Delta\,\lambda(T))^2$, which is also consistent with that of a single s-wave isotropic BCS gap. In all likelihood, the polycrystalline nature of our sample might prevent us from determining its actual gap structure due to disorder and or impurities, as suggested by the large residual resistivity and small RRR value.

### 3.3.6 Heat Capacity

A characteristic superconducting transition was observed in the specific heat data, indicating bulk superconductivity. By fitting the $C/T$ vs $T^2$ data to the Eq. 3.6,

$$C/T = \gamma + \beta T^2. \tag{3.6}$$

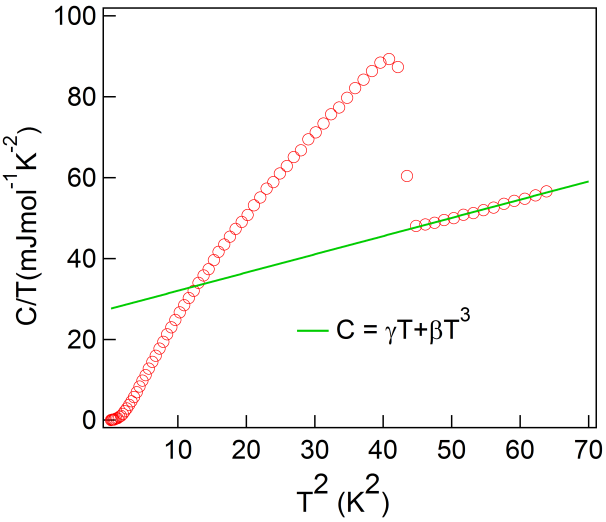


Figure 3.14: Temperature dependence of the total heat capacity. The data shows the superconducting transition and the solid line is a fit to the Eq. 3.6 as described in the text to estimate the phonon and electronic contributions to the total heat capacity.

as shown in Fig. 3.14, the value of the Sommerfeld coefficient was determined to be $\gamma = 27.5 \pm 0.4$ mJ mol$^{-1}$K$^{-2}$ and $\beta = 0.451 \pm 0.009$ mJ mol$^{-1}$K$^{-4}$. This moderate $\gamma$ value indicates the quasiparticles [4] have a larger effective mass than free carriers. The

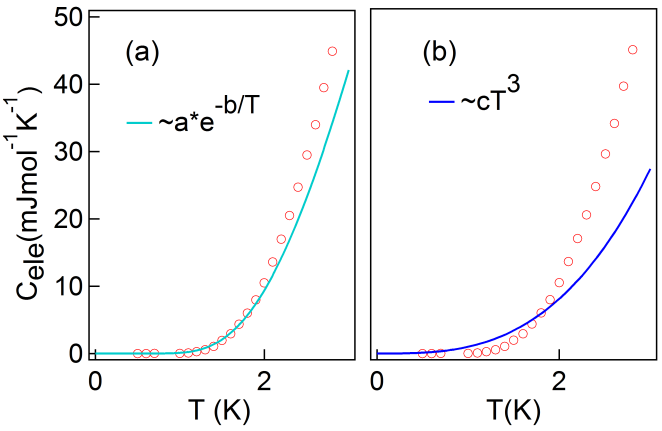


Figure 3.15: The electronic heat capacity below $T_c$ with fits for the BCS (a) and anisotropic (b) gap structures (solid lines) as described in text.

quantity $\beta$ is related to the Debye temperature through the relation $\beta = \frac{N12\pi^4 R}{5\Theta_D^3}$ which gives the Debye temperature for $Re_6Zr$ as 630 K for N= 58 atoms in the unit cell. The Debye temperature we found is quite large compared to the previous report. However, the large unit cell allows for nonacoustic phonon modes which can contribute to the overall heat capacity even at moderately low temperatures [144]. Thus, the actual Debye temperature might be in between the value estimated using N = 58 and N = 1. The ratio $\Delta\ C/\gamma\ T_c$ was found to be 1.62, which is in agreement with the previous work[17]. The ratio $\Delta\ C/\gamma\ T_c$ is larger than the BCS value of 1.43, indicating moderate coupling strength in $Re_6Zr$, which is in agreement with the behavior of the thermal conductivity.

The electron-phonon coupling strength can also be estimated using the McMillan formula [156] described by Eq. 3.7,

$$\lambda_{e-ph} = \frac{1.04 + \mu^* ln(\theta_D/1.45T_c)}{(1 - 0.62\mu^*)ln(\theta_D/1.45T_c) - 1.04} \tag{3.7}$$

Here, $\mu^*$ is the coulomb repulsion parameter, and for intermetallic superconductors [157], it generally assumes a value of 0.13. Thus, for $Re_6Zr$, the electron-phonon coupling strength was found to be $\lambda_{e-ph} \simeq 0.69$ using the intermediate value of $\theta_D = 319$ K taken from ref. [118]. The value of $\lambda_{e-ph}$ puts $Re_6Zr$ in the moderate- to strongly-coupled regime.

From the Sommerfeld coefficient the DOS can be calculated using the formula [158], $\gamma = (\pi^2\ k_B^2\ \mathrm{N(E}_F)/3)$, which yields a DOS to be 11.6 $\frac{states}{eV\,f.u.}$, where f.u. stands for formula unit. This large DOS is consistent with the theoretical calculations.

The low temperature behavior of the electronic specific heat and thermal conductivity is often a good indicator of the superconducting gap characteristics. For example, a power law behavior indicates nodes in the superconducting energy gap, while exponential behavior indicates a conventional, fully-gapped BCS state [18]. The electronic specific heat ($C_{\mathrm{ele}}$) below $T_c$ was estimated by subtracting the lattice component, $\beta\ T^3$, from the total specific heat. The electronic specific heat was then analyzed by fitting the data to the following forms: $a\ \exp^{-b/T}$ and $c\ T^3$. These are the expected temperature dependencies for gaps that are isotropic or contain point nodes, respectively. Our data are well fit by the exponential fit $C_{\mathrm{ele}} \propto a\ \exp^{-b/T}$ below $T = 2$ K, as shown in Fig. 3.15(a). The cubic power law does not represent the data as well as the exponential fit [Fig. 3.15(b)]. The above analysis suggests an isotropic gap. However, the accuracy of low-temperature electronic specific-heat data obtained by subtracting a phonon contribution grossly depends on the accuracy in determining the normal-state heat capacity from the in-field measurements[155]. In our study, the phonon contribution was estimated from zero-field data. Hence, the actual temperature dependence of the electronic specific heat might not be represented by the current data. Therefore, it would be difficult to distinguish the power law describing point nodes from the exponential behavior in our measurements. Note also that a similar behavior of the low temperature electronic specific heat in $Mo_3Al_2C$ was found in two different studies. First, Karki *et al.* [150] found exponential behavior in the low temperature electronic specific heat by using zero-field data to calculate the phonon contribution, while Bauer *et al* [155] found a power law behavior, when the phonon contribution was calculated by investigating the heat capacity thoroughly in both zero and applied field.

### 3.3.7 Doping and Pressure Studies

To investigate the effect of chemical doping on the superconducting transition temperature of $Re_6Zr$, we synthesized multiple samples doped with Hf, Ti, W, and Os. Among the doped samples, Os doping had a significant positive effect on the superconducting transition temperature, enhancing $T_c$ by $\approx 1\%$ per 1% nominal doping concentration as seen in Fig. 3.16. Due to the heavy nature of its constituent elements, we expect SO coupling to play a significant role in the physical properties of $Re_6Zr$. Os, being heavier, could enhance the SO coupling leading to an increase in $T_c$. The other dopants at or below nominal 10% either lowered the $T_c$ or had little effect. Note that unconventional pairing mechanisms in anisotropic channels are sensitive to disorder, and doping generally suppresses the transition temperature. An increase in $T_c$ with Os doping then either indicates an $s$-wave singlet-triplet mixing, inconsistent with the TRS breaking, or an intricate interplay of the ASOC with the microscopic mechanism responsible for unconventional pairing. The latter explanation, to our knowledge, has not yet been investigated theoretically in sufficient detail.

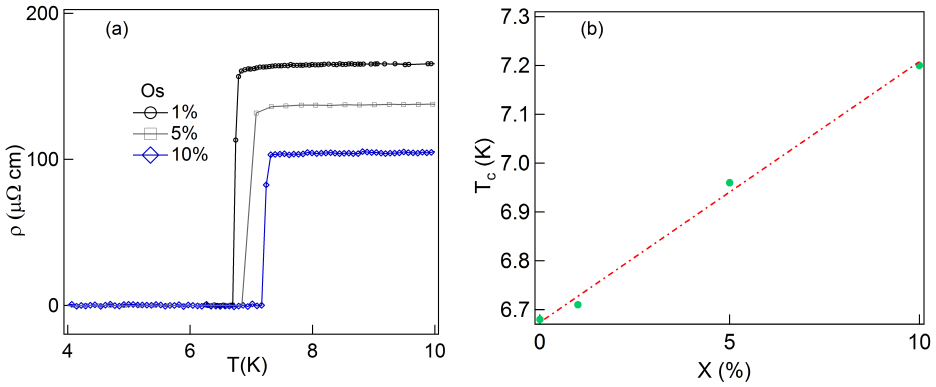


Figure 3.16: (a) Superconducting transitions in the Os-doped samples observed in the temperature dependence of the electrical resistivity. (b) Change in the superconducting transition temperature as a function of Os doping. The broken line is a linear fit to the data which shows a linear increase in the transition temperature.

The pure sample was also exposed to moderate hydrostatic pressure up to 8 kbar. Pressure only had a small effect on the transition, decreasing $T_c$ slightly as shown in Fig. 3.17.

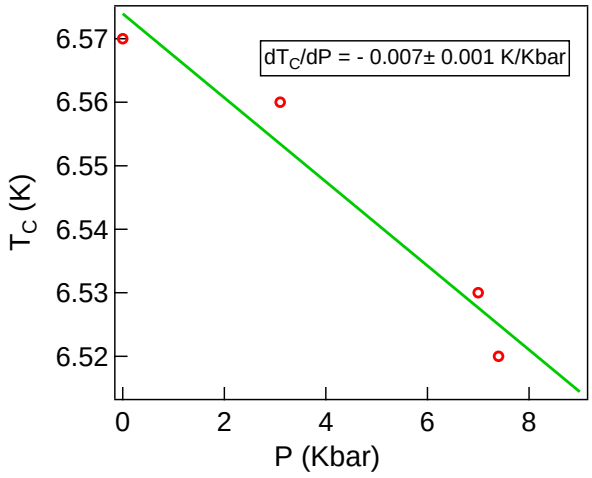


Figure 3.17: Change in the superconducting transition temperature of pure $Re_6Zr$ due to applied pressure. Solid line is a linear fit to the data which indicates a negative slope.

The solid line is a linear fit to the data which shows the decreasing trend of transition temperature under applied pressure.

All of the superconducting parameters calculated for $Re_6Zr$ are summarized in the Table 3.1.

Table 3.1: Superconducting and physical parameters of $Re_6Zr$

| Parameters | Unit | Value |
|---|---|---|
| $T_c$ | K | 6.7 |
| $\rho_0$ | $\mu\ \Omega$ cm | 135 |
| $\mu_0\ (\frac{dH_{c2}}{dT})_{T=T_c}$ | T/K | - 2.31 ± 0.04 |
| $\mu_0 H_{c2}$ | T | 11.6 ± 0.1 |
| $\mu_0 H^{Pauli}$ | T | 12.2 |
| $\xi_0$ | Å | 53.3 |
| $\lambda_0$ | Å | 3696 |
| $\kappa_0$ | | 69.3 |
| $\gamma$ | mJ/mol $K^2$ | 27.5 ± 0.4 |
| $A/\gamma^2$ | $\mu\ \Omega$ cm $mol^2$ $K^2$ $J^{-2}$ | 10.44 |
| $\Delta C/\gamma T_c$ | | 1.62 |
| $N(E_F)$ | states/ eV f.u. | 11.6 |
| $\lambda_{e-ph}$ | | 0.69 |

## 3.4 Conclusion

We have discussed the NCS superconductor $Re_6Zr$ by synthesizing polycrystalline samples of pure and doped $Re_6Zr$ utilizing arc-melting techniques. The results of XRD mea-

surements and elemental analysis confirm single-phase materials with the noncentrosymmetric $\alpha$-Mn structure type. From resistivity, magnetic susceptibility, and specific heat measurements, $Re_6Zr$ was confirmed to be a strongly correlated, type-II superconductor with a bulk transition temperature near 6.7 K with a moderately strong electron-phonon coupling. Several doping studies revealed that Os doping significantly enhanced $T_c$, which is possibly due to enhanced SO coupling. The thermal conductivity is dominated by the phonon contribution near the superconducting transition and is enhanced below $T_c$ due to a decrease in electron-phonon scattering, as normal electrons pair up to form the condensate. Applied magnetic fields between $H_{c1}$ and $H_{c2}$ suppress the peak due to phonon-vortex scattering. The upper critical field $H_{c2}(0)$ is comparable to the calculated Pauli limit, which can be a consequence of the SO interaction or strong coupling or might also be due to the contribution from a triplet pairing component to the order parameter.

While the above measurements coupled with the irreducible representation analysis [118] of the crystal point group of $Re_6Zr$ suggest that the superconducting behavior of $Re_6Zr$ deviates from that of the conventional superconductors, the low temperature electronic specific heat and penetration depth are best fit with an exponential temperature dependence. This is interesting, given that the authors of the irreducible representation analysis [118] showed that the order parameters for $Re_6Zr$ cannot belong to the fully symmetric representation, and therefore anisotropy is intrinsic and protected. From the representational analysis of the crystal point group of $Re_6Zr$, several solution or permitted states were found. Among those, two three dimensional F1 and F2 states, indicated that there are line nodes at $k_z = 0$ for the superconducting order parameter.While in the two dimensional E state there are clearly point nodes along $k_x = k_y = k_z$ of the Fermi surface. These states are required by symmetry to be anisotropic [118]. However, current experimental data suggests the gap is isotropic which is similar to the majority of the NCS superconductors, where conflicting behavior restricts the order parameter. Perhaps the smaller ASOC compared to other NCS superconductors, where nodes in the gap, as well

as non-BCS behavior was found, limits the amount of triplet component contributing to the order parameter. As discussed before, using the canonical examples of $Li_2Pt_3B$ and $Li_2Pd_3B$, where the presence of Pt results in an order of magnitude larger ASOC and nodes in gap, where as with Pd, the gap is BCS-like. Perhaps there is a lower limit to the strength of the ASOC, below which the triplet component that leads to linear nodes is too small to be experimentally discernible, but might support the existence of point nodes. The discussion in the introductory chapter, which summarizes the existing examples of nodal NCS superconductors, supports this proposition.

Another interesting scenario is to consider multi-gap singlet states, such as s+is, as described in Ref. [159]. Here, a non-zero (neither zero nor $\pi$) phase difference corresponds to the TRS broken state, while maintaining the fully-gapped order parameter. Within this multi-gap scenario, interband triplet pairing can also give rise to a fully-gapped yet TRS broken state, which was suggested for $LaNiC_2$ and $LaNiGa_2$. It was suggested that the pairing occurs between electrons of same spin, but on different orbitals, leading to a superconducting wave function with a triplet component but an isotropic even parity gap symmetry, since the overall wave function remains antisymmetric under particle exchange [159]. Interestingly, a very recent report [53] on a single crystalline sample of $Re_6Zr$ suggested multiband superconductivity from point contact Andreev Reflection data, where the order parameter consists of two isotropic gaps.

Considering the strength of the ASOC, the data, taken in its entirety, somewhat weigh against lines of nodes in the superconducting gap of $Re_6Zr$, but may be consistent with point nodes. To truly establish the effect of broken inversion symmetry in $Re_6Zr$, low temperature studies of the physical and thermal properties on a single crystal are highly desirable.

# Chapter 4
# Non-trivial Berry Phase in BiPd

## 4.1 Introduction

In this chapter we will discuss another NC superconducting system, BiPd, which recently has gained much interest in the context of a topologically non-trivial compound. Topological materials, such as topological insulators (TI) and topological superconductors (TSC's), are emerging materials with complex electronic structures and novel physical properties with potential use in practical applications, such as spintronics and quantum computation [160–166]. These interesting phenomena appear when strong spin-orbit coupling (SOC) modifies the band structure leading to non-trivial band states [160, 162]. In a TSC, it is the wave function of the electron pairs that exhibits topological properties, and among the most promising candidates for topological superconductivity are materials with non-centrosymmetric (NCS) crystal structures. In NCS superconductors, the lack of an inversion center lifts the spin degeneracy and, combined with strong antisymmetric SOC, leads to a complex order parameter with mixed spin singlet and spin triplet pairing components [18]. This can lead to topologically non-trivial superconducting phases, where the existence of Majorana fermionic modes at the vortex core with gapless edge states have been predicted. [167–169] The TSC is defined by a full superconducting gap in the bulk, but gapless edge or surface states, which are a consequence of Majorana fermions forming an Andreev bound state (ABS). [170] Majorana fermions are unique in that they are their own antiparticle, and they are of tremendous interest, not only in condensed matter, but also in high energy particle physics. [171]

BiPd displays type-II superconductivity below $\sim$3.8 K [172–174] and has attracted much interest recently due to the possibility of realizing unconventional superconducting states owing to the large SOC, and hence spin splitting due to the presence of the heavy element Bi. [175]. A plethora of experiments has been done in the last two years.

These include surface measurements utilizing STM and ARPES, which show Dirac surface states [174, 175] with unusual anisotropic behavior [176], where a hybridization of surface and bulk bands was considered. Interestingly, in the STM study, a strong zero-bias conductance peak (ZBCP) was observed in the vortex core, which was attributed to a Caroli-de Gennes-Matricon vortex core bound state, of which a zero-energy Majorana state is a special case. [175, 177] A ZBCP was also observed in the directional point contact Andreev reflection (PCAR) measurement [66], which suggests an unconventional order parameter for the superconducting state of BiPd. The mystery of the true nature of the superconducting state deepens, since thermal and transport measurements indicate that the bulk supports a multiple isotropic fully-gapped superconducting state.[172, 178] Many of these interesting properties share similarities with other TSC candidates [166], such as $Cu_{0.25}Bi_2Se_3$ and $PbTaSe_2$ [179]. In fact, $Cu_xBi_2Se_3$ [170] displays a similar ZBCP in PCAR measurements, which was attributed to the existence of Majorana fermions and hence topological superconductivity. Thus, further investigations of BiPd are highly desirable. Our contribution was to measure quantum oscillations in BiPd, which are usually studied to investigate the electronic structure of topological materials, such as surface states and non-trivial topology of the bands.

Here, we will discuss quantum oscillations in single crystal BiPd measured by torque magnetometry, i.e. the de Haas-van Alpen (dHvA) effect, in a tilted magnetic field. Analysis of the dHvA data suggests the Fermi surface is complex, three-dimensional, and composed of multiple sheets. One of the identified dHvA frequencies near 40 T demonstrates a non-trivial Berry phase with a very small effective mass. This suggests that this pocket of Fermi surface is topologically non-trivial, with transport governed by Dirac fermions. These results are compared to our detailed electronic structure calculations and data from previously reported surface probes.

We will briefly discuss the dHvA effect below, which will be followed by a detailed experimental procedures section and then results and discussion.

## 4.2 de Haas-van Alphen Effect

The de haas-van Alphen (dHvA) effect is the oscillatory response of the diamagnetic susceptibility of a metal in an applied magnetic field [180]. Since the discovery of oscillatory magnetic phenomena in pure Bismuth (Bi) metal by de Haas and van Alphen in 1930 at low temperature [180], a great deal of theoretical and experimental effort has been given to understand and interpret the effect. In the experiment with Bi, the magnetization near 14 K was measured in increasing field, and when the magnetic susceptibility was plotted against inverse field, 1/B, oscillatory behavior was found that was periodic in 1/B, which can be seen in Fig. 4.1. The oscillation was found prominently at low temperature and at a considerably high magnetic field. Landau explained this oscillatory phenomena as a direct consequence of quantization of a charged particle, which in this case are electrons, in a magnetic field, and thus the dHvA effect is a purely quantum mechanical phenomenon [180]. The diamagnetism comes from the magnetic response of nearly free conduction electrons under applied field producing shielding current [4]. This is a consequence of the famous Lenz's law. In 1952, Onsager established the theory for the dHvA effect utilizing the Landau quantization of the electron orbit in an applied field.

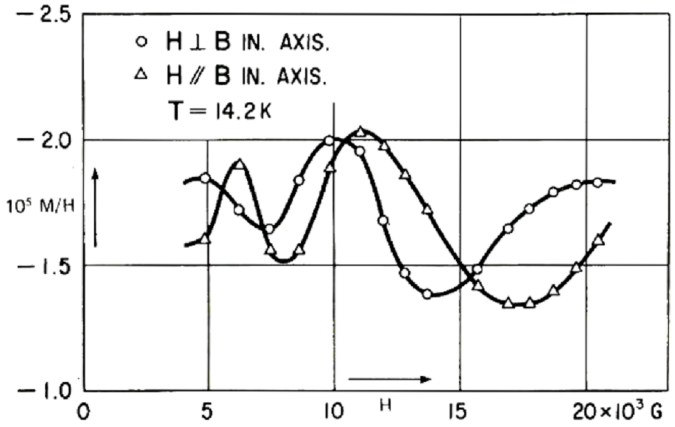


Figure 4.1: First experimental observation of oscillatory magnetic susceptibility in pure Bi.[180]

Onsager determined that the change in 1/B through a single period is given by [180],

$$\frac{1}{F} = \Delta(\frac{1}{B}) = \frac{2\pi q}{\hbar c}\frac{1}{A}. \tag{4.1}$$

Here, F is the frequency of the oscillation and $A$ is the extremal cross-sectional area of the Fermi surface normal to the applied magnetic field. This equation can be rearranged to give the simple form,

$$F = \frac{\hbar c}{2\pi q}A. \tag{4.2}$$

Thus, it is obvious from Eq. 4.2 that the extremal area of a cross-section of a Fermi surface of a metal is proportional to the frequency of the oscillation and can be utilized to study the Fermi surface.

From the semiclassical approach, the electrons in a magnetic field are influenced by the Lorentz force [4], $\vec{F}$

$$\vec{F} = q(\vec{v} \times \vec{B}). \tag{4.3}$$

When the applied field is perpendicular to the direction of the electron motion, we can apply the Sommerfeld quantization rule to get the famous Onsager relation [180],

$$a_n = (n + \frac{1}{2})\frac{2\pi qB}{\hbar c}. \tag{4.4}$$

Here, B is the applied field, $q$ is the charge of the electron and $n$ is the number of landau levels. For a free electron in closed circular motion due to the Lorentz force $\vec{F}$ mentioned above, the electron will occupy space in a tubular fashion, i.e in Landau tubes to satisfy the quantization rule given by Eq. 4.4. Landau tubes consist of the extremal orbits of the electron in field on an equal constant energy surface $\varepsilon$. The extremal orbits are those in the cross-section of the constant energy surface that dominates the response to

the applied field [4]. The non-extremal orbits differ in phase and simply cancel out. Here, $a$ is the area of the cross-section of the Landau tubes, which are now allowed orbits or states in k-space for the electron to stay in the applied field. For a free electron system with a spherical Fermi surface (FS) i.e. a constant energy surface, the Landau tubes are circular cylinders with an axis along the direction of the applied field, as seen in Fig. 4.2.

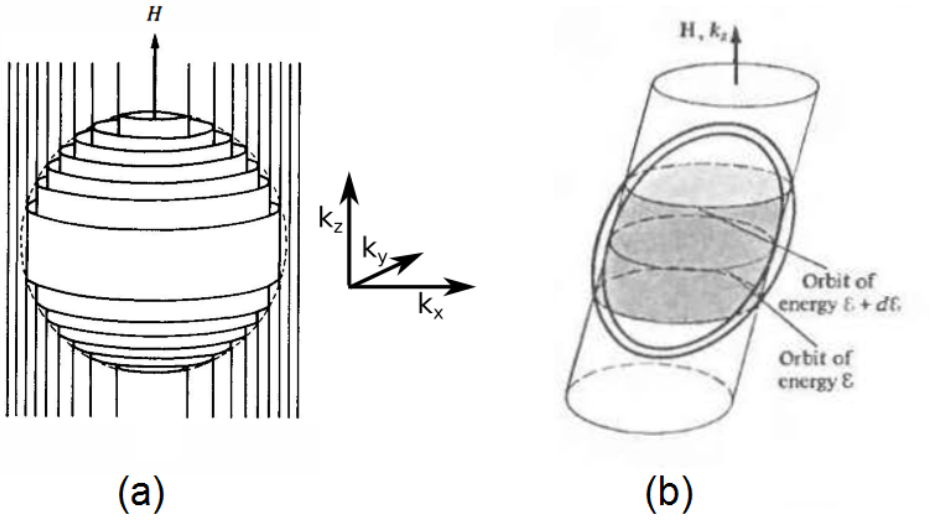


Figure 4.2: Schematic diagrams for (a) spherical constant energy surface, with field along $z$. The Fermi surface is indicated by a broken curve, and the tubes that are inside are occupied at base temperature i.e. 0 K [180]. (b) A Landau tube with an extremal orbit of constant energy $\varepsilon$ at a certain field. The orbit is perpendicular to the field direction [115].

The oscillatory magnetization can be understood by Fig. 4.2. If the applied field is weak, we can assume that there are a large number of tubes inside the Fermi surface, since from Eq. 4.4, it is obvious that the area of the tubes are proportional to the field strength. With increase in field, the area will increase, and the tube will expand until it decouples itself from the FS, allowing the next tube to do the same as the field is kept increasing, until the field reaches the quantum limit i.e. when n = 1. When the Landau tube separates itself from the FS, the electron density of states at that instant will vanish to zero. It is nonzero when the next tube is in the extremal orbit as shown in Fig. 4.2(b). This zero and nonzero occupation occurs periodically in increasing field, and this change in density of states is apparent in almost all electronic properties, such as magnetization (dHvA),

resistivity (Shubnikob-de Haas, SdH), and thermal properties. Thus, when the nth Landau tube leaves the FS at some field $B_n$, we get [4],

$$\frac{1}{B_n} = (n + \frac{1}{2})\frac{2\pi q}{\hbar c A}. \tag{4.5}$$

Successive tubes with equal area in $k$ space on the FS are given by,

$$A(\frac{1}{B_{n+1}} - \frac{1}{B_n}) = A\Delta(\frac{1}{B}) = \frac{2\pi q}{\hbar c}. \tag{4.6}$$

Eq. 4.6 indicates that equal increment of inverse field reproduces similar orbits of equal area in k space, and hence the periodicity in transport properties mentioned above [4]. The frequency of the oscillation is then given by Eq. 4.2.

Since the Landau tubes are quantized by default, and there are no tubes in between the constant energy range $\varepsilon$ and $\varepsilon + d\varepsilon$, all the levels above the energy $\varepsilon$ collapse to the next tube at $\varepsilon + d\varepsilon$ [115]. Thus, the Landau tubes are highly degenerate in energy. It is obvious from the discussion above that extremal areas can be accessed in different parts of the FS by applying field in different directions, as illustrated in Fig. 4.3.

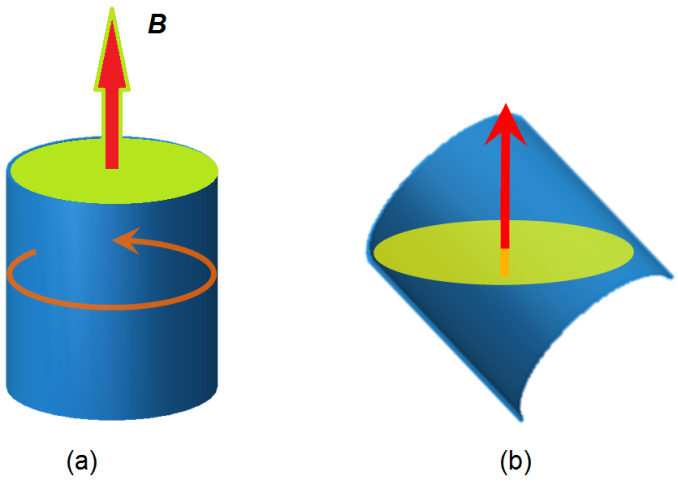


Figure 4.3: Different orbits of FS on a Landau tube when the area is extremal. (a) (b) Field applied in different directions, and hence different parts of the FS are accessed in the Landau tube.

As shown in Fig. 4.3(a), the yellow area is an extremal area perpendicular to field, and this area will increase or decrease as we move away from this initial direction (Fig. 4.3(b)). Thus, the increase or decrease in area will give corresponding frequencies which can be plotted as a function of the field direction (usually angle, $\theta$), and from this plot, the shape of the FS can be estimated by analyzing the angular dependence of the frequency.

To analyze the FS and related information, such as the cyclotron mass corresponding to the carriers at the FS, as well as the phases of the wave function of the carriers, a detailed analysis of the magnetic oscillations was necessary, and this was done elegantly by Lifshitz and Kosevich [180]. A full derivation of the Lifshitz and Kosevich (LK) formula is beyond the scope of this dissertation, and we will use the formula discussed by Shoenburg in his seminal book on magnetic oscillations in metals [180]. LK derived the response of the thermodynamic potential, $\Omega$, to the applied field, which essentially is related to all the observable quantities of the system. For example the magnetic response, i.e. moment, is given by,

$$M_s = -(\frac{\partial \tilde{\Omega}_s}{\partial B}). \tag{4.7}$$

Considering different factors that affect the oscillations, such as finite temperature, carrier scattering, and hence the relaxation rate, and spin, the oscillatory magnetization can finally be written as,

$$\Delta M \simeq \sum_{p=1}^{\infty} \frac{(-1)^p}{p^{3/2}} B^{\lambda} R_{T,p} R_{D,p} R_{S,p}\, sin[2\pi p(\frac{F}{B} - \gamma_p - \delta_p)]. \tag{4.8}$$

Eq. 4.8 is known as the LK formula [180] and is widely used in analyzing the magnetic oscillations observed experimentally. Here, the terms $R_T$, $R_D$ and $R_S$ are defined by subsequent equations, and $p$ refers to the $p^{th}$ harmonics of the fundamental frequencies. $R_T$ is the thermal damping term, which defines the effective mass of the band carriers. This finite temperature effect can be seen as phase smearing of the oscillation and results in

a reduction of the oscillation amplitude. At a finite temperature (T>0 K), the metallic properties are averaged over energies within a $k_B$T of constant energy $\varepsilon$. If the energy separation between two Landau tubes is smaller than $k_B$T, then for a given applied field, all the extremal orbits in that energy range will contribute to the overall average, and the oscillation will be smeared out [115]. This reduction of amplitude is handled by the reduction factor $R_T$, which is described by Eq. 4.9.

$$R_T = \frac{\alpha p T \mu}{B\, sinh(\frac{\alpha p T \mu}{B})}; \mu = \frac{m^*}{m_e}; \alpha = \frac{2\pi^2 k_B m_e}{e\hbar}. \tag{4.9}$$

,

where $m^*$ is the effective mass of the quasiparticles, and $\alpha$ amounts to a constant value of 14.7 T/K.

The effect of carrier scattering stemming from electron-electron or electron-phonon interactions, or from impurities, is described by$R_D$ in Eq. 4.10. If the electron relaxation rate is $\tau$ due to the scattering, then its energy can be estimated within $\Delta\varepsilon \sim \frac{\hbar}{\tau}$. If this energy is larger than the Landau tube separation, then the oscillatory structure will be diminished [115]. This is known as the Dingle reduction of the oscillatory amplitudes. The temperature $T_D$ is the Dingle temperature, and it describes the amount by which the amplitude is reduced due to the scattering. It can be understood simply by considering that, if there were no scattering of the electrons, than the actual amplitude of the oscillation at T = 0 K will not be diminished, but would be larger than the experimentally observed values. However, the amplitude is reduced as if the temperature of the system was not zero, but raised to a temperature known as the Dingle temperature:

$$R_D = e^{\frac{-\alpha p T_D \mu}{B}}. \tag{4.10}$$

The amplitude can also be affected by the Zeeman effect, due to the spin of the electron. If the spin-orbit interaction is negligible, then in a magnetic field, the spin degeneracy of

the energy levels are lifted, and the levels are split into two separate levels by an energy difference [180] $\Delta\varepsilon = \frac{1}{2}g\beta_0 H$. Here, $g$ is the spin-splitting factor, and for free electrons, $g \sim 2$. In general, the spin-up and spin-down electrons have separate Landau tubes which leads to a phase difference between the oscillations coming from the electrons with spin-up and spin-down [180]. This leads to an interference between these two contributions, and the reduction factor caused by this interference is simply given by Eq. 4.11, which is due to the superposition of spin-up and spin-down oscillation amplitudes to the net amplitude [180].

$$R_S = cos(\frac{\pi p g \mu}{2}). \tag{4.11}$$

It is also worth noting that, apart from the reduction factor described above, the overall condition of the sample that is under investigation can have substantial contribution to the amplitude reduction. For example inhomogeneity in the sample can smear out the amplitude. Mosaicity in crystals are also a source of amplitude reduction, since the crystal orientation is no longer absolute [180]. Thus, sample preparation is one of the most important activities of any investigation that involves the study of quantum oscillations, and high quality single crystals are a priority.

Finally, the oscillation is described by the sinusoidal term which contains the phase factor (-$\gamma_p$-$\delta_p$), where $\gamma_p$ is related to the Berry phase $\Phi_B$, as $\gamma_p = \frac{1}{2}$ - $\frac{\Phi_B}{2\pi}$. This phase analysis is of great significance. The topological nature of the bands can be directly assessed by the value of the phase. Generally, a trivial parabolic band topology will amount to a Berry phase of zero [180] i.e. $\gamma_p = \frac{1}{2}$. As described earlier, recent interest in topological phenomenona is investigated through the quantum oscillations and Berry phase analysis, which provides the motivation for this chapter as well. Aspects of the Berry phase will be discussed briefly in the following section.

Another important factor is the dimension of the Fermi surface cross-section, which is characterized by the term $\delta_p$. For a 2 dimensional Fermi surface $\delta_p = 0$, and it is $\delta_p = \pm \frac{1}{8}$ for a 3 dimensional surface [181]. The sign of $\delta_p$ is determined by the curvature

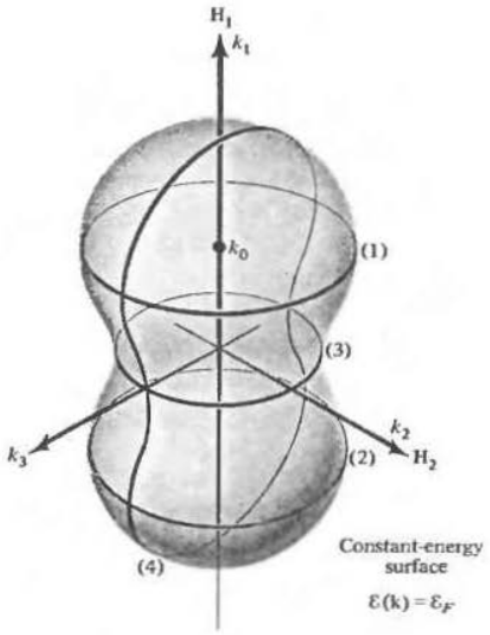


Figure 4.4: Schematic illustration of maximum and minimum extremal orbits. When the field is along $k_1$, the orbits labeled as 1 & 2 are maximum extremal orbits, while 3 is a minimum [115].

of the constant energy surface. It is positive when the Fermi surface cross-section is at a minima, and negative when the cross-section is at a maxima. The minimum and maximum cross-section of an extremal orbit are shown in Fig. 4.4. The factor $\lambda$ is also determined by the dimensionality of the Fermi surface, assuming a value of 0 for 2D and 1/2 for 3D pockets, respectively. [181]

### 4.2.1 Berry Phase and Topological States

In 1984 Berry published his seminal work on adiabatic evolution of a quantum state in its parameter space [182]. In this work he showed that the quantum state gains a phase (a geometrical phase) in addition to the dynamical one after the completion of an adiabatic cyclic evolution. In a classical analysis, the states of materials, such as solids, are defined by the obvious symmetries that are inherent to the lattice structures. However, there are also hidden symmetries, such as time reversal symmetry, that are only apparent in the wave function describing the system, not in the real space lattice symmetries. To

investigate and understand such symmetries and their evolution, as well as their impact on the wave function, and hence certain properties of matter, the wave function is subjected to the adiabatic evolution near the Brillouin zone. The adiabatic evolution can be understood by considering a non-degenerate quantum mechanical system with a time-dependent Hamiltonian. By keeping the eigenstates non-degenerate, we let the Hamiltonian evolve slowly in time, and if after the change, there are no transitions between the eigenstates, then the evolution of the Hamiltonian is adiabatic [183]. The rate of change or evolution of the Hamiltonian depends on the energy gap between the eigenstates, and hence is smaller than the gap for the adiabatic case.

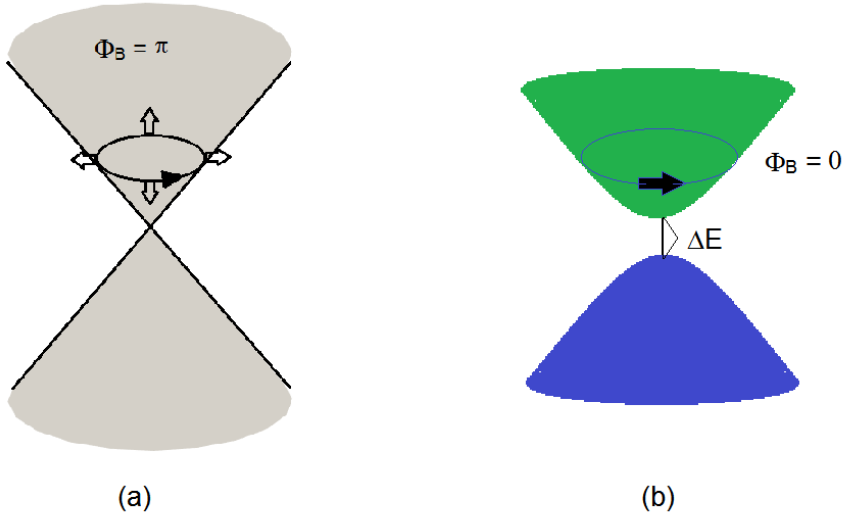


Figure 4.5: Accumulation of Berry phase. (a) $\pi$ Berry phase in coupled bands with a linear dispersion without a gap. (b) Parabolic dispersion between two uncoupled gapped bands produces a zero Berry phase.

Berry showed that in an cyclic adiabatic evolution of the eigenstates, where the external parameters evolve slowly, and make a loop in parameter space, then at the end of the loop, the eigenstates will return to their original state with an additional phase (Berry phase) [184]. The manifestation of a Berry phase has been realized in many areas, such as molecular physics, optics, resonance phenomena in nuclear quadrupole systems, as well as topological systems in solid state physics. [184, 185] The first example of this geometric

phase was found by Pancharatnam in an optical experiment, where interference between two systems was utilized. [183]. In solid state systems, the Berry phase has a profound effect and has gained much interest, since Zak [186] showed that the electron in a periodic lattice configuration can also gain Berry phase. Here, the Brillouin zone in reciprocal space plays the role of the parameter space. Mikitik and Sharlai [185] discussed the manifestation of the Berry phase in a metallic system under an external magnetic field, where the quantized levels of electrons host the Berry phase due to the semi-classical quantization condition. It is obvious from this that the dHvA effect would be the perfect tool to investigate the Berry phase, since the basis of the oscillatory phenomena is also the quantization rule, which forms the Landau tubes as discussed before. In general, a Berry phase is expected when the electronic bands have a crossing, such as in graphene, or an avoided crossing [185], which points toward the massless Dirac nature of the band carriers, satisfying a necessary condition for topological surface or edge states. The manifestation of the Berry phase was observed in TI's, which are generally probed through quantum oscillations [165].

In the following sections, we will discuss the sample preparation, which includes the synthesis of single crystalline BiPd, details of the experimental technique, and finally results and discussion.

## 4.3 Experimental Description

Single crystals of BiPd were synthesized using a modified Bridgman technique in an rf-induction melting furnace. About 10 grams of elementary Bi (alfa aesar 99.999%) and Pd (alfa aesar 99.999%) were weighed out, and the stoichiometric mixture was put in an alumina crucible. A polycrystalline ingot was made from this initial mixture by melting it in the rf-induction furnace. The ingot was then ground to powder and placed in a tapered graphite crucible with a pointed bottom. The graphite crucible was then placed inside a quartz tube and sealed under vacuum. The tube was placed inside the rf coil and suspended by the crystal puller. Ground polycrystalline BiPd was slowly melted, and then the tube was slowly lowered through the heating zone at a rate of 1-1.5 mm/hr. After 3 days of

growth, a large single crystal was formed with an easily cleavable surface.

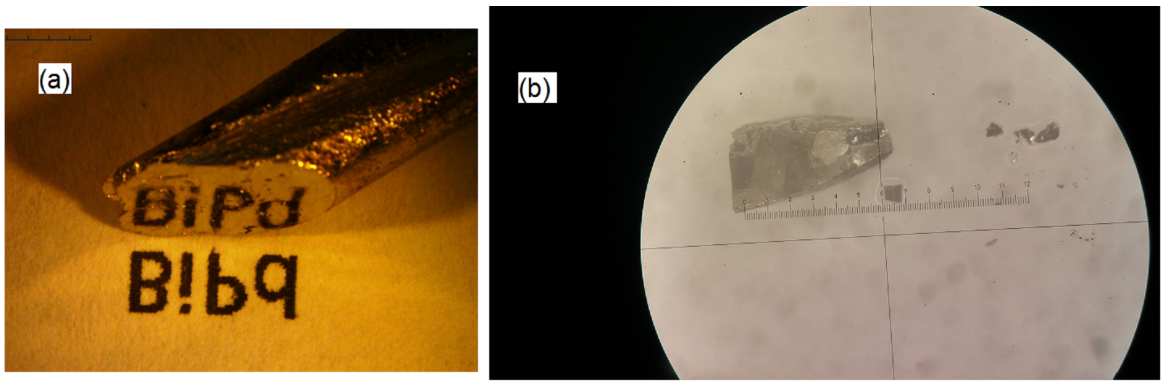


Figure 4.6: Single crystal of BiPd grown via a modified Bridgman technique. (a) A mirror-like surface is observed from the as-cleaved crystal. (b) Examples of cleaved pieces, which were analyzed via XRD and used in further measurements.

The crystal structure and phase purity of the samples were investigated by powder X-ray diffraction (XRD) using a small portion of powdered sample on a PANalytical Empyrean multi-stage X-ray diffractometer with Cu K$\alpha$ radiation ($\lambda$ = 1.54 Å). The system has a $\theta$-2$\theta$ geometry, and data were taken from 10° to 90° at a constant scan of 2° per minute at room temperature. The crystal structure was further analyzed using extensive XRD experiments using a PANalytical Empyrean X-Ray Diffractometer with a Pixcel1D detector and a HTK 1200 high temperature chamber. To check for the structural transitions reported earlier [187], a temperature dependent XRD was performed in the temperature range from 25–300°C with a heating rate of 2° C/min in an atmosphere of $N_2$ gas. A $\theta$-2$\theta$ geometry was utilized, and the scan range was (2$\theta$)= 15°–60° with a fixed step size of 0.0262°. Each step was counted for 41.6 sec to get better statistics.

The electrical resistivity was measured using a standard four-probe ac technique at 27 Hz with an excitation current of 1-3 mA, in which small diameter Pt wires were attached to the sample using a conductive epoxy (Epotek H20E). Data were collected between 1.8 and 290 K and in magnetic fields up to 9 T using a Quantum Design Physical Property Measurement System (PPMS). The specific heat was measured in the PPMS using a time-relaxation method between 2 and 20 K at 0 and 9 T. Magnetic susceptibility was also

measured in the PPMS in a constant magnetic field of 30 Oe; the sample was zero-field-cooled (ZFC) to 1.8 K, and then magnetic field was applied, followed by heating to 10 K and then cooled down again to 1.8 K [field-cooled (FC)]. The low temperature upper critical field was measured in a 35-T resistive magnet at the National High Magnetic Field Laboratory (NHMFL) in Tallahassee, FL using a four-probe ac technique with a 3-mA excitation current.

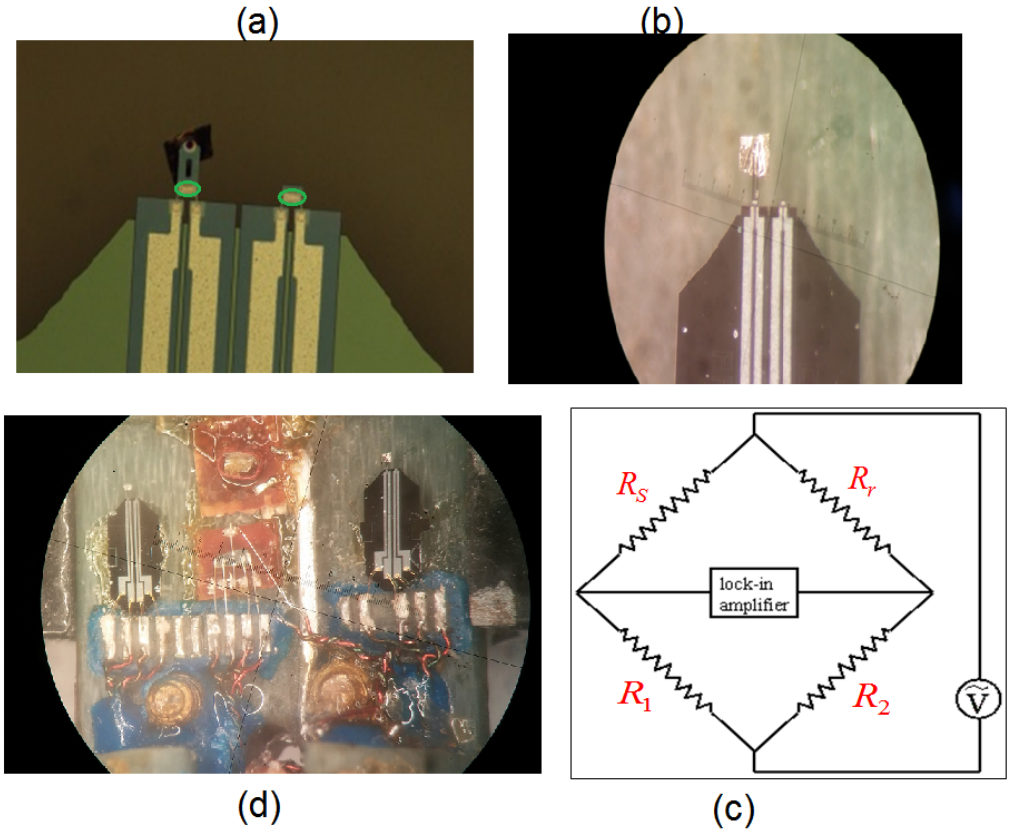


Figure 4.7: Torque magnetometry. (a) The PRC400 piezoresistive cantilever [188]. The green circles indicate the piezoresistive parts, where the sample and the reference are inserted. (b) A cleaved piece of crystal is attached to the cantilever. (c) The Wheatstone bridge arrangement for detection. (d) The whole assembly of the cantilever and four-probe holder are attached to the sample probe in a 16-pin connector. The sample probe is also attached with a stepper motor for sample rotation. Each turn of the stepper motor is equivalent to $\sim 7^\circ$ rotation. The data were collected using LabVIEW.

The measurement of quantum oscillations was done at the NHMFL using the 35-T resistive magnet at a base temperature of 350 mK. The torque magnetometry was em-

ployed using a PRC400 piezoresistive cantilever to detect the magnetization, and hence the corresponding oscillations under applied field. A cleaved piece of BiPd was attached to the cantilever, where the base of the cantilever has a piezoresistor, which changes its resistance value, when the cantilever is flexed, as seen in Fig. 4.7. There is a matching reference piezo-resistance value without a sample attached (Fig. 4.7(a)) which balances the sample resistance part. These resistances are then used in a Wheatstone bridge configuration which can be seen in Fig. 4.7(c) with two external resistors to balance the resistance of the complete bridge configuration. The whole circuit is very sensitive to torque through the very small changes in resistance, as the sample cantilever moves up and down due to the magnetization of the sample.

In our measurement,The field was initially applied at -21° from the *b*-axis and was then rotated towards the *ac*-plane. The orientation angle was measured from the cleaved surface, utilizing the natural termination of the crystal. The crystal was rotated in steps of roughly 7° to a maximum of 140° from its initial position. The torque magnetometry technique is highly sensitive and measures the anisotropy in the samples magnetization. For an applied field at some angle $\theta$ with respect to the *ac*-plane of the sample, the torque is that given by $\tau = \vec{M} \times \vec{H} = (\mathrm{M}_c\mathrm{H}_a - \mathrm{M}_a\mathrm{H}_c)\vec{b}$. Thus, in torque magnetometry measurements, the torque, and hence the amplitude of the oscillations, is minimum when the applied field is along a high symmetry direction, which in our case is when the magnetic field is perfectly aligned along the out-of-plane (B‖b) and in-plane (B‖ac) directions,

Once the angle dependent measurement was done, the sample cantilever assembly was then placed at 28° from the *b*-axis to do the temperature dependent measurements. Data were taken from 0.35 K to 20 K, and the corresponding torque was used to determine the effective mass of the electrons.

## 4.4 Results and Discussion

### 4.4.1 Crystal Structure and Electronic Band Structure

All of the XRD measurements indicated that the crystals formed in the $\alpha$-monoclinic phase with space group $P2_1$, which is noncentrosymmetric and chiral. The powder XRD pattern indicating the monoclinic structure is shown in Fig. 4.8.

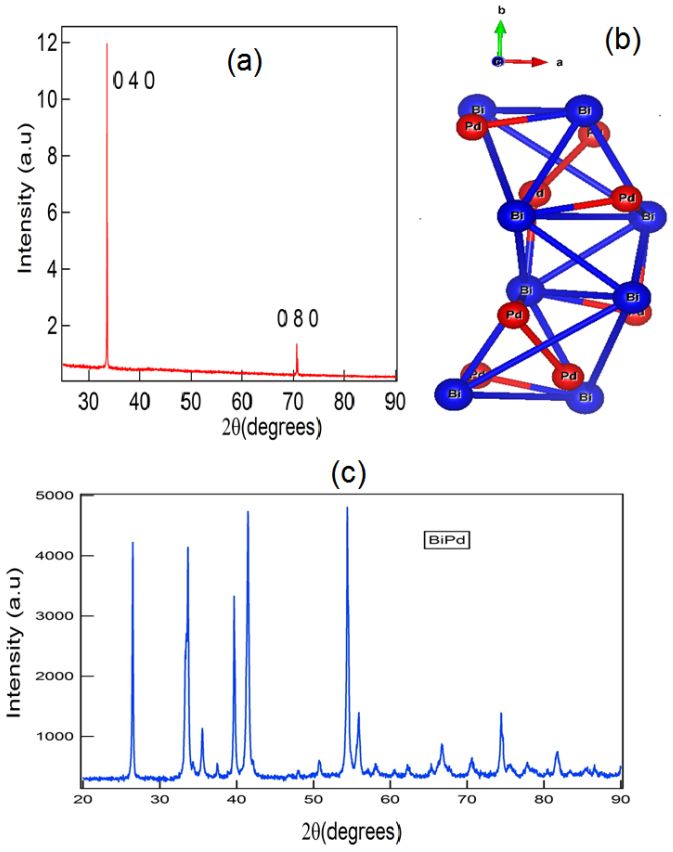


Figure 4.8: XRD patterns of BiPd. (a) Reflection from the (0 $k$ 0) plane, indicating the cleaved surface is along the $ac$-plane. (b) Crystal structure of BiPd, which lacks an inversion center, as well as a mirror plane.(c) Full powder XRD, indicating the single phase compound.

A cleaved piece of single crystal BiPd was analyzed using X-ray diffraction (XRD) which shows reflections from the (0 $k$ 0) plane only, as seen in Fig. 4.8(a), indicating the cleaved surface is perpendicular to the unique axis ($b$-axis) of its monoclinic structure. This cleaving along the ($h$ 0 $l$) plane is in agreement with previous reports. [174, 187] The results of the temperature-dependent XRD are shown in Fig. 4.9 A clear peak splitting is

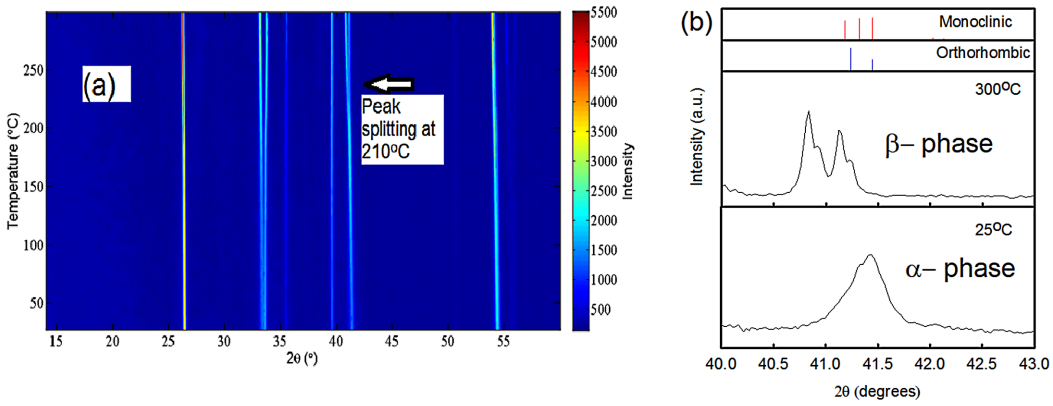


Figure 4.9: (a) Peak splitting indicating the transition from the monoclinic to the orthorhombic phase of BiPd. (b) Split peak was indexed and tracked through the transition.

observed at $\sim 210^{\circ}$ C, which confirms the polymorphic change from the $\alpha$ to the $\beta$ phase of BiPd [187] and indicates the crystals are in the correct phase.

### 4.4.2 Resistivity and Uppercritical Fields

From the temperature dependent resistivity, a sharp superconducting transition was found at 3.8 K as seen in Fig. 4.10(a). The resistivity is metallic with a RRR of over 100. This clearly indicates the crystals are of good quality. There is an inflection at around 30 K, whose origin is unknown. The residual resistivity is quite low compared to the room temperature value, suggesting a low scattering of carriers from impurities.

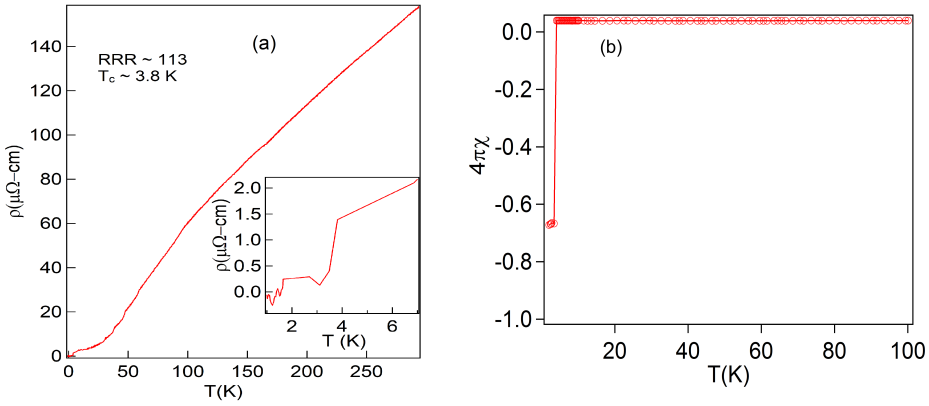


Figure 4.10: Superconducting transition of BiPd (a) in resistivity at 3.8 K . Inset: The low temperature resistivity. The residual resisitvity is small compared to the room temperature resistivity. (b) ZFC susceptibilities for BiPd at a constant field of 30 Oe. The value of the ZFC volume susceptibility data at low temperatures indicates bulk superconductivity.

The superconducting transition was also investigated via magnetization measurements, where the diamagnetism in the superconducting phase was observed. The ZFC temperature dependent magnetic susceptibility data are shown in Fig. 4.10(b). Measurements were performed at 30 Oe in a temperature range from 1.8 K to 100 K. The onset of diamagnetism occurs near 4 K, which is in agreement with the transport data. The ZFC data show a large, negative volume susceptibility at low temperature indicating bulk superconductivity. A perfect Meissner fraction corresponds to $4\pi\chi$ = -1. Several small odd-shaped pieces of sample were measured, and the data were not corrected for demagnetization effects.

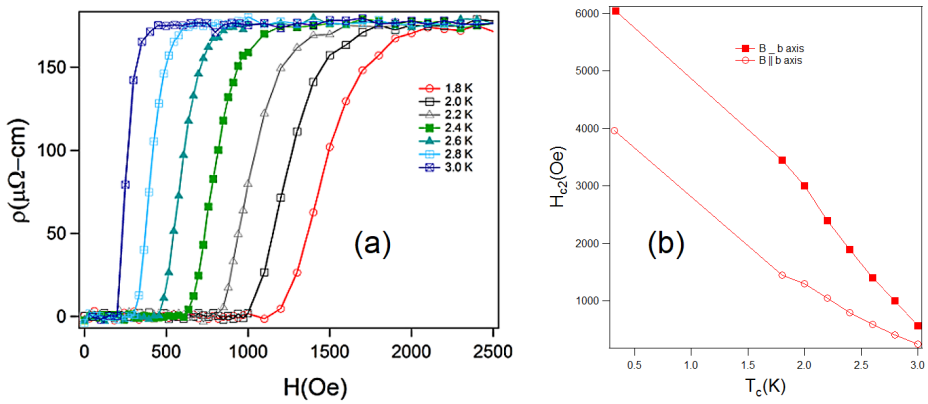


Figure 4.11: Uppercritical field of BiPd. (a) Critical fields from transport measurements done in the PPMS. (b) Anisotropy in the uppercritical field measured at the NHMFL and PPMS.

While estimating the uppercritical fields of BiPd, interesting properties were observed. There is a significant anisotropy in the uppercritical fields of BiPd when measured by applying field parallel and perpendicular to the crystallographic *b*-axis. A similar discrepancy in the uppercritical field was found in published works [65, 175].

### 4.4.3 dHvA Oscillations

For the quantum oscillation measurement, the field was applied parallel to the *b*-axis and was then rotated towards the *ac*-plane. The orientation angle was measured from the cleaved surface, utilizing the natural termination of the crystal. The rotation was about 7° per step, and the crystal was rotated about 117°, clockwise from its initial position as

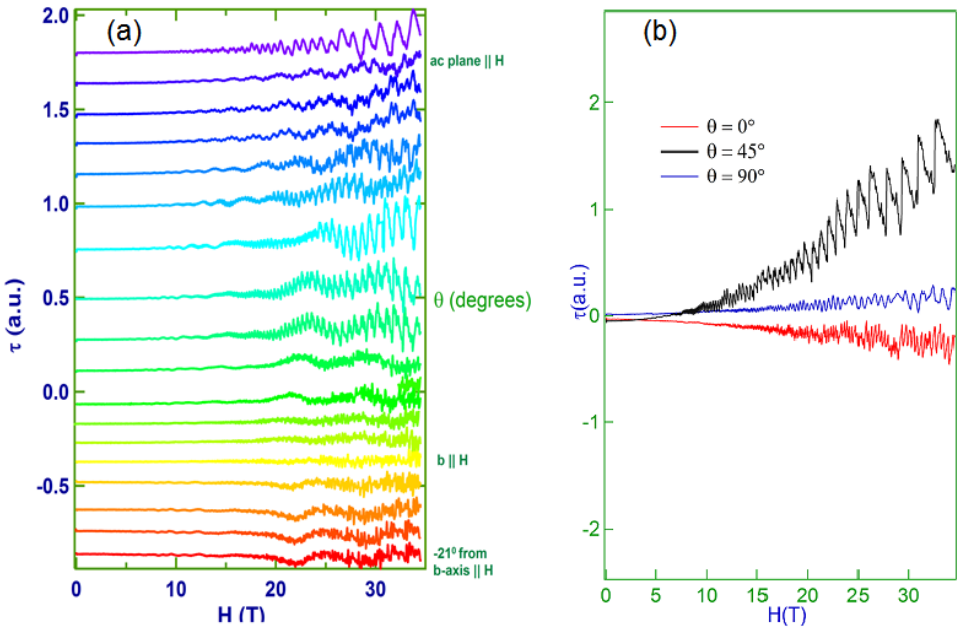


Figure 4.12: Quantum oscillations detected via torque response of the cantilever magnetometer at 0.35 K. (a) Raw oscillations with magnetic field applied at various angular directions with respect to the $b$-axis. The oscillations at higher field i.e. beyond 26 T, become saw tooth like, indicating that the cantilever deflection amplitude has maxed out, i.e. gone out of range, and the data beyond that range are not characteristic of BiPd. (b) Raw oscillations for field along, perpendicular, and at 45° from the $b$-axis showing the oscillation is minimized along the in-plane and out-of-plane directions.

well as -28° in counterclockwise direction. At all angular directions, clear oscillations were observed in the torque measurements, as shown in Fig. 4.12. In torque magnetometry measurements, the torque, and hence the amplitude of the oscillations, is minimum when the applied field is along a high symmetry direction, which is evident when the field was along the $b$-axis ($\theta = 0°$) or the $ac$-plane ($\perp$b-axis, $\theta = 90°$) and can be seen in Fig. 4.12.

From the raw oscillation, a smoothed background was subtracted. In general there are two ways of determining the background for the oscillations. First, the raw data is fit with a 3rd or 5th order polynomial equation and then the fit is used as a background. Or, a smoothing operation is applied to the raw data. Fitting the raw data with a higher order polynomial (>3) is usually avoided, since higher order polynomials can add extra frequencies, which are not from the sample. Hence, our choice was to use a smoothed background subtraction, while for a consistency check, we performed polynomial fits as

well. Both operations produced similar results. The background subtracted data are then plotted against inverse field, which shows the oscillations are periodic in 1/B, as shown in Fig. 4.13. Here, the field was applied about 70° from the *b*-axis.

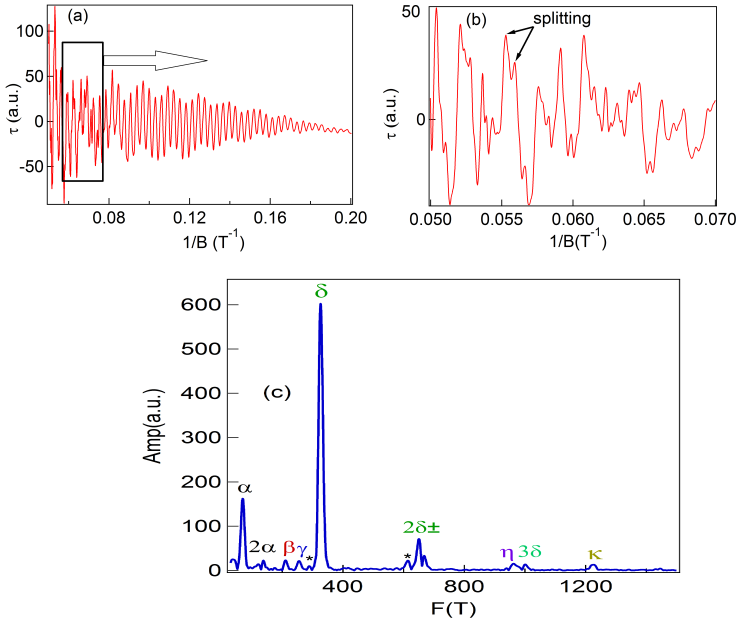


Figure 4.13: (a) Torque response of the cantilever magnetometer at 0.35 K with field applied at 70° from the *b*-axis showing dHvA oscillations in inverse field. A smoothed background was subtracted from the raw data. (b) The rectangular section in the box of (a) was zoomed to show the spin splitting of oscillations at higher field. (c) Corresponding frequencies were extracted by performing a Fast Fourier Transform (FFT) over the field range from 5 20 T. The primary frequencies $\alpha$, $\beta$, $\gamma$, $\delta$, $\eta$ and $\kappa$, and higher harmonics, are labeled in the figure. The star symbols represent some additional frequencies as described in the text.

Once the raw data were treated and plotted against inverse field, a Fast Fourier Transform (FFT) was performed using the FFT option within the Igor Pro software package. [189]. Before the FFT, the data were processed to increase the data resolution by performing a redimensioning operation, which just increases the number of data points by keeping the actual data range intact. Then a Hanning operation was performed to raise the signal to noise ratio. Then the FFT was performed, and several frequencies were extracted, as seen in Fig. 4.13(c). The fundamental frequencies are labeled as $\alpha$, $\beta$, $\gamma$, $\delta$, $\eta$ and $\kappa$, as well as their higher harmonics. The oscillations when the field was applied at 70° from the

$b$-axis contain a maximum number of frequencies as seen in Fig. 4.13(c).

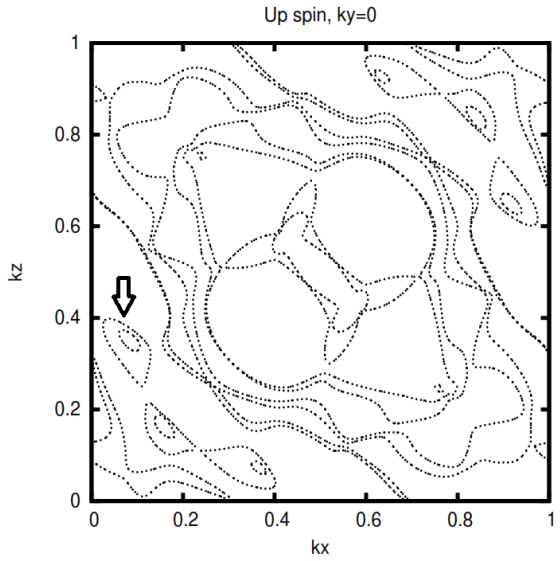


Figure 4.14: Slice of the Fermi surface at $K_y = 0$. The frequency $\alpha$ is indicated by a double arrow.

At higher field the Zeeman splitting is apparent in the raw oscillations (Fig. 4.13(b)). When the dHvA oscillations contain more than a single frequency, a variety of new effects can occur, such as frequency and amplitude modulation of one frequency by another and, more generally, the creation of a combination of frequencies and their harmonics, and in general, these effects can be attributed to either the magnetic interaction effect or the magnetic breakdown of frequency orbits [180]. Since the frequency $\delta$ appears to be dominant among all the frequencies it is more likely to be susceptible to magnetic breakdown. The small satellite peaks near $\delta$, designated with an asterisk in Fig. 4.13(c) likely represent the frequency and its higher harmonics that correspond to a breakdown orbit as well. In general magnetic interactions may result in unusually strong harmonics [180].

Rotating the sample with respect to the applied field reveals the dispersion of the dHvA frequencies. The results of the FFT for all angular position of the applied field are shown in Fig. 4.15. Among all the frequencies, the 40 T frequency ($\alpha$) is present over the entire angular sweep from $-21^\circ$ to $119^\circ$. Several other frequencies appear at different field directions and disappear quickly as the crystal is rotated. The high frequency $\delta \simeq$

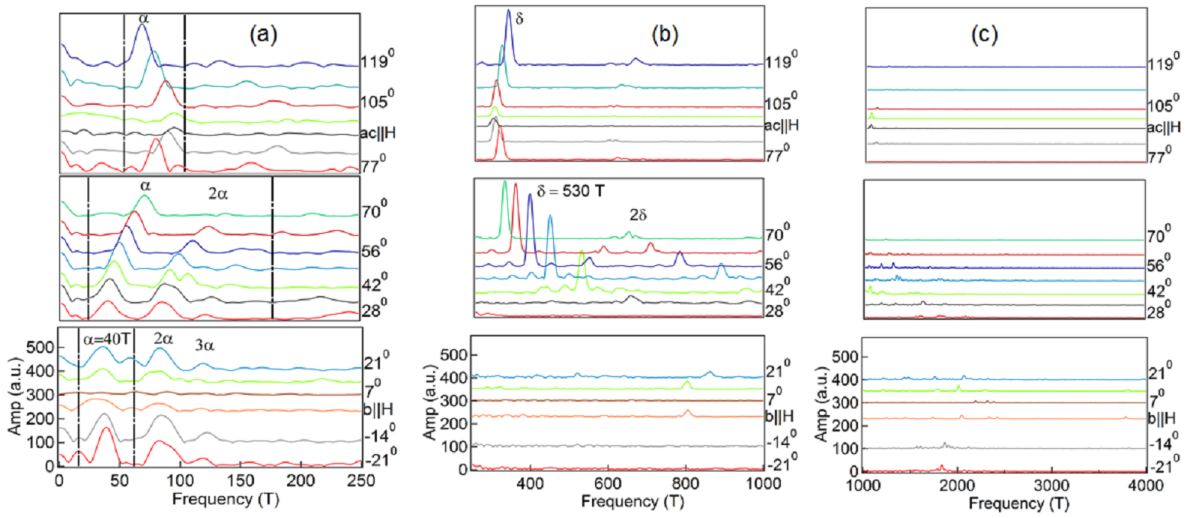


Figure 4.15: Result of the Fast Fourier Transform (FFT) of the oscillations in inverse field. The FFT was divided into 3 frequency regions: low, medium, and high frequency regions for clarification. (a) Result of FFT in the low frequency range 0 to 300 T, (b) the medium frequency range 300 to 1000 T, and in (c) the high frequency range 1000 to 4000 T.

530 T oscillations appear when the field was applied at 42° from the $b$-axis and remains for the rest of the angular sweep, which can be seen in Fig. 4.15. There is a moderate dispersion observed in the small frequency $\alpha$. The value of the frequency increases and assumes a maximum, when the field is applied along the $ac$-plane, or perpendicular to the $b$-axis ($\theta = 90°$). The shift in both of the frequencies $\alpha$ and $\delta$ can be followed for a significant range of angles, whereas the larger fundamental frequencies and the higher harmonics disappear upon further rotation of the crystal.

The angular dispersion of all the frequencies are shown in Fig. 4.16. Most of the frequencies appear at a certain angle and disappears upon further rotation of the crystal. This fast movement made it impossible to determine a general shape of those frequencies. Thus, we will attempt to further analyze the frequencies $\alpha$ and $\delta$.

The frequency dispersion of both $\alpha$ and $\delta$ are shown in a 3-dimensional plot in Fig. 4.17. It is evident that the frequency $\alpha$ is 3 dimensional in nature, as it persists in the entire angular sweep.

The $\alpha \simeq 40$-T frequency angular dependence can be fit by a 3-dimensional ellipsoid of

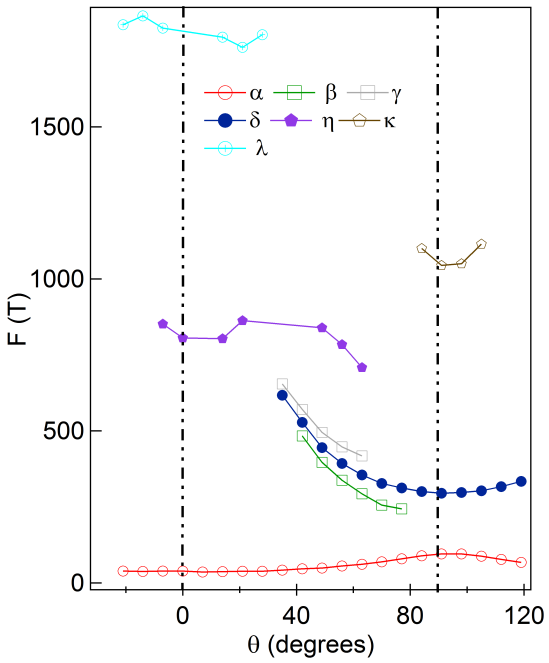


Figure 4.16: Frequency dispersion with respect to change in angular direction of the applied field with respect to $b$-axis. Only the fundamental frequencies are plotted.

the form in Eq. 4.12,

$$F(\theta) = \frac{F_0}{\sqrt{(cos(\theta - \theta_0)(\frac{\pi}{180}))^2 - \frac{1}{\varepsilon}(sin(\theta - \theta_0)(\frac{\pi}{180}))^2}}. \tag{4.12}$$

A similar fit to the angular dependence of the FFT frequencies was done for $BaFe_2As_2$ by Ross *et al*[190]. Here, the ellipticity was found to be $\varepsilon \sim 2.7$, as seen in Fig. 4.17(b). Thus, $\alpha$ is an anisotropic, 3-dimensional (3D) pocket of Fermi surface. Interesting physical phenomena are often associated with these kind of small pockets. The dispersion of frequency $\delta$ can also be fitted reasonably well with the 3 dimensional ellipsoid with ellipticity of ∼3.0 as seen in Fig. 4.17(c). Thus this is also a 3-dimensional piece pocket of the Fermi surface.

All of the fundamental frequencies calculated from the FFT analysis are listed in Table. 4.1 The Fermi surface cross-section ($A_F$) was calculated using the Onsager relation [180] $A_F = \frac{2\pi^2 F}{\Phi_0}$, where $\Phi_0 = \frac{h}{2e} \sim 2.067 \times 10^{-15}$ Wb is the magnetic flux quantum.

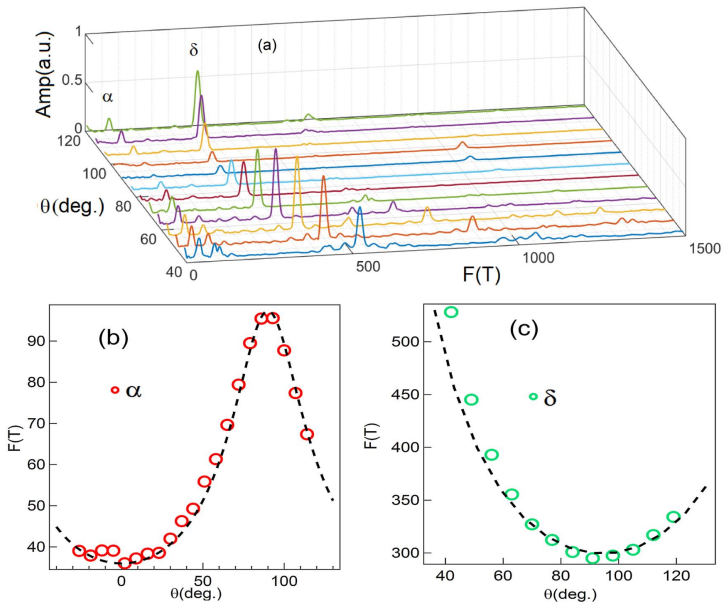


Figure 4.17: Frequency dispersion in rotating the sample with respect to applied field.(a) To get a clear view of frequencies $\alpha$ and $\delta$ data here are shown from the field along 42° to 119° with respect to b-axis.(b) Angular dependence of $\alpha$, the frequncy can be well described by a 3D anisotropic ellipsoid (dashed black curve) with ellipticity of 2.7. (c) Angular dependence of $\delta$, this frequency also corresponds to a 3D Fermi pocket, since it can be fitted with a 3D ellipsoid with ellipticity of 3.0 (black dashed line).

### 4.4.4 Effective Mass of the Quasi-particle

The dHvA oscillations i.e. the oscillatory magnetization can be described by the Lifshitz-Kosevich (LK) formula [185, 191], described in Eq. 4.8. Using the individual damping terms, such as $R_T$, described in Eq. 4.9, we can calculate the effective mass of the band carriers. This can be done by fitting the temperature dependence of the oscillation amplitude with Eq. 4.9. Since at certain angular positions and at higher fields, magnetic breakdown and Zeeman splitting occur, we applied the field at 28° from the *b*-axis. At this position, only few of the frequencies are present, and the effect of Zeeman splitting and magnetic breakdown are minimized. From the band structure calculations, it was also found (Fig. 4.14) that the frequency $\alpha$ is not susceptible to magnetic break down, and thus it is the perfect candidate for further analysis that can give us information about the phase, and hence topology of this band. Also, at this angular position and at higher temperatures, only the $\alpha$ frequency dominates and persists at temperatures as high as 20

Table 4.1: Fundamental dHvA frequencies obtained from torque measurements of BiPd and their corresponding Fermi surface cross-sections ($A_F$), which were calculated as described in the text.

| Label | F (T) | $A_F \times 10^{-5}$ (Å$^2$) |
|---|---|---|
| $\sigma$ | 40 | 381 |
| $\beta$ | 210.78 | 2012.8 |
| $\gamma$ | 256 | 2444.7 |
| $\delta$ | 530 | 5061.3 |
| $\eta$ | 962.82 | 9194.6 |
| $\kappa$ | 1227.5 | 11722.2 |

K, as shown in Fig. 4.18(a). This indicates a light mass for the band carriers associated with this frequency.

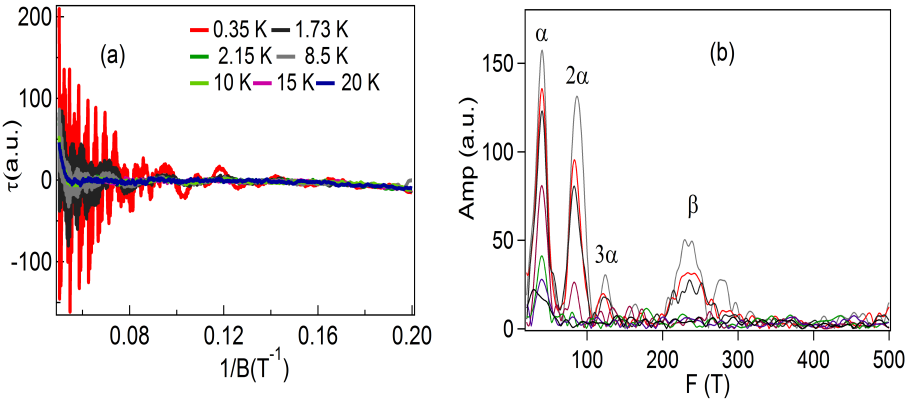


Figure 4.18: (a)Temperature dependent torque measurement. (a) Background subtracted oscillation in inverse field showing a decrease in oscillations. (b) Corresponding FFT showing the decrease in the oscillation amplitude over the field range from 5 to 20 T.

.

To resolve the frequency amplitude carefully from the background, data up to 15 K were used in the fit, as shown in Fig. 4.19. The effective mass for the $\alpha$ mode was found to be $m^* = (0.18 \pm 0.01)m_e$ from the fit (Fig. 4.19(a)), where we have used the thermal damping term of Eq. 4.8, and $m_e$ is the mass of a bare electron. The amplitudes of the other large frequencies drop abruptly, as shown in the Fig. 4.18(b). Increasing the temperature prevented an accurate estimation of the effective mass for all the oscillatory modes. For example, using only a limited number of data points (3 for $\beta$), the effective of mass of the frequency $\beta$ was estimated to be $(0.55 \pm 0.03)m_e$,which can be seen in Fig. 4.19(b). From

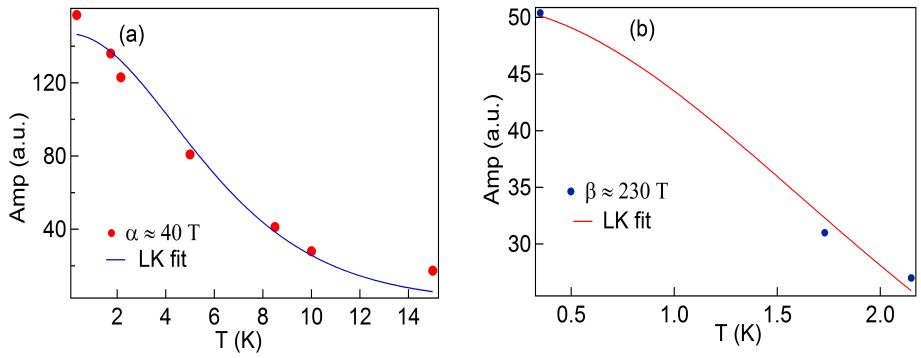


Figure 4.19: LK fit, using the thermal damping term $R_T$, to the temperature depenedent amplitude of the frequencies: (a) $\alpha$ with a mass of (0.18±0.01)$m_e$, and (b) $\beta$ with a mass of (0.55 ± 0.03)$m_e$. $m_e$ is the mass of a bare electron.

.

the analysis above, the frequency $\alpha$ stands out with its light mass and small area, as well as its 3D nature. From the effective mass and using the frequency along the $b$-axis, the average (over all orbits) the Fermi velocity can be estimated using the relation $v_F = \frac{\sqrt{2e\hbar F}}{m^*}$. The value for the frequency $\alpha$ was found to be $v_F = 2.2 \times 10^5\, ms^{-1}$. Now we will consider the phase of the $\alpha$ frequency.

### 4.4.5 Phase of the Frequency Orbit

The phase analysis is necessary to determine the nature of the band carriers as well as the topology of the bands. Typically, topological materials are analyzed by studying their electronic structure, which is investigated through quantum oscillations and the Berry phase associated with it. As discussed in the introductory section, using Eq. 4.8, we can estimate the total phase, and hence the Berry phase associated with the oscillation, thereby gaining information on the bands.

Upon a closer look, and from the analysis above, we found the data at 10 K to be optimum to perform a total LK fit. For the oscillations at 10 K, the higher frequencies were already damped, and the signal-to-noise ratio is better than the higher temperature data. Thus, using the 10-K data, we fit the oscillation with Eq. 4.8, as shown in Fig. 4.20.

In the LK fit, the value of B is found from the average of the field range used. In the

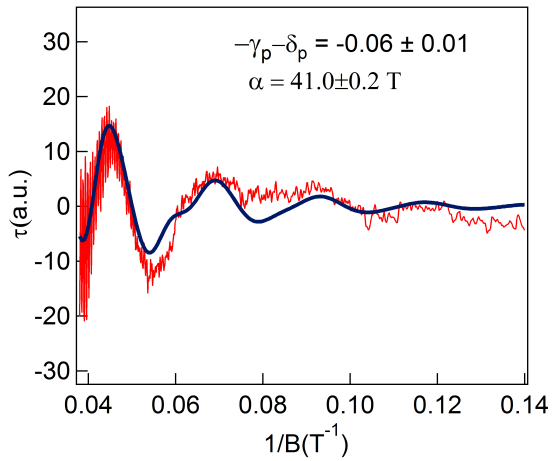


Figure 4.20: The blue solid line is the LK fit to the 10-K data (red curve), as described in the text. Two higher harmonics and the principle frequency were used for fitting over the broad field range from 7  25 T. The residual high frequency oscillation doesn't appear until around 23 T. Hence, the 40-T frequency is dominant at 10 K.

fit shown in Fig. 4.20, B was calculated as, $\frac{1}{B} = (\frac{1}{7} + \frac{1}{25})2$, with the mass was taken from the fit shown in Fig. 4.19. The value of the exponent on B, i.e the term $\lambda$, was set to 1/2, since the $\alpha$ frequency is 3-dimensional. Upon fitting, several useful pieces of information can be extracted. First, the frequency of 41.0±0.2 T was extracted, which matches the frequency obtained from the FFT and indicates a consistent analysis.

The phase factor ($-\gamma_p$-$\delta_p$) was found to be -0.06±0.01. From this, the Berry phase can be estimated using appropriate values of $\delta_p$ for a 3-dimensional Fermi surface. Here, it assumes values of ± 1/8. Thus, the Berry phase was calculated to be (1.13±0.01)$\pi$ for the surface with the cross-section at a minimum ($+\frac{1}{8}$), or (0.63±0.01)$\pi$ for the cross-section with a maximum, ($-\frac{1}{8}$). This result indicates the Berry phase is clearly non-trivial. For a parabolic, i.e. Schrodinger type electron, the Berry phase would be zero or $2\pi$, which would mean the band has trivial topology. The non-zero $\pi$ Berry phase points toward Dirac-like carriers and a non-trivial topology. [160, 165]

### 4.4.6 LL-fan Diagram and Dingle Temperature

The topological properties of the Fermi surface are determined by the values of the Berry phases, which can also be extracted from a Landau level (LL) fan diagram. The DOS

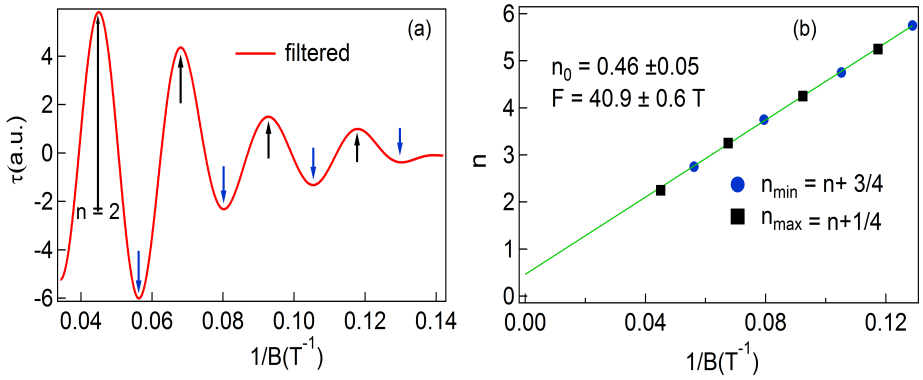


Figure 4.21: (a) The frequency $\alpha$ after the filtering process. The oscillation minima and maxima are indexed as discussed in the text. (b) LL-fan diagram as discussed in the text. The solid line is a linear fit with an intercept $n_0 = 0.46\pm0.05$. The slope of the fit corresponds to the original frequency, i.e. 40.9±0.6 T.

is proportional to $dM/dB$. Thus, the LL index should be assigned an integer value for the minima and maxima in the dHvA oscillations and plotted versus the corresponding inverse field values. We then applied this analysis to the frequency $\alpha$. It was first isolated, and the oscillation minima and maxima were indexed with integer values n to get the LL-fan diagram [192, 193]. To isolate the oscillations corresponding to the frequency $\alpha$ only, it was filtered out from the background subtracted data at 10 K using a band-pass filter in Igor Pro. For every filtering cycle, the data were analyzed by FFT to make sure the frequency and the phase of remain constant, so the overall phase of the frequency does not change, which can be seen in Fig. 4.22. This is important in order to get the correct Berry phase information as mentioned above. Once the filtering was complete, the oscillation minima are defined by n+$\frac{3}{4}$(Fig. 4.21(a), blue arrows) and the maxima by n+$\frac{1}{4}$ (Fig. 4.21(a), black arrows) [192, 193]. These integers are then plotted versus inverse field to obtain the LL-fan diagram.

The Berry phase can then be estimated using the intercept, i.e. $\Phi_B = 2\pi(n_0 \pm \delta_p)$, where $\delta_p$ is the same as defined above. From the Landau-fan fit to the filtered data (Fig. 4.21(b)), the intercept $n_0$ was found to be 0.46±0.05. Using this value, the Berry phase was estimated to be (1.17±0.05)$\pi$ for the minimal cross-section or (0.67±0.05)$\pi$ for

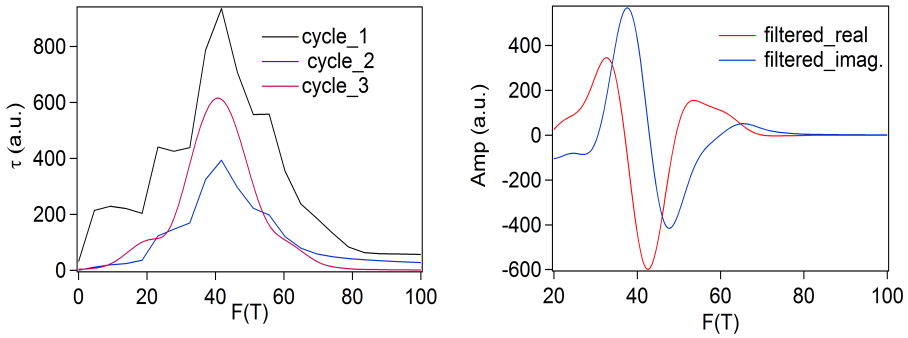


Figure 4.22: Evolution of frequency filtering. (a) The frequency $\alpha$ in the filtering process. The result of the FFT in subsequent filtering yields exactly the same frequency, as expected. (b) Real and imaginary part of the FFT after the last cycle of filtering.

the maximal cross-section. These values are consistent with the phase determined from the LK fit. Furthermore, the slope of the linear fit in the Landau fan diagram in Fig. 4.21(b), which is 40.9±0.6 T, equals the frequency found previously from the FFT analysis and the LK fit.

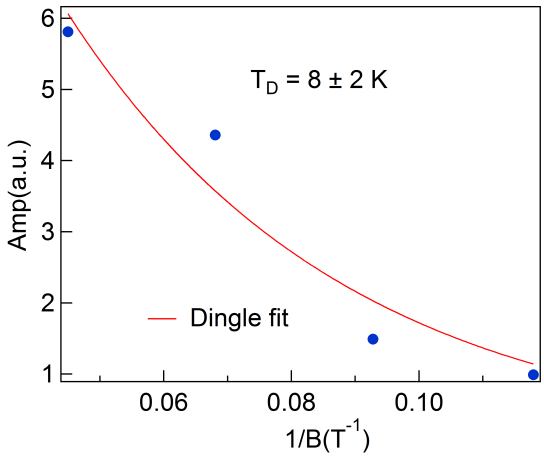


Figure 4.23: The Dingle temperature of frequency $\alpha$. The amplitude of the oscillation maxima was noted from the filtered oscillation data and plotted against the corresponding field value. The solid line is a fit to the Dingle temperature term Eq. 4.10.

The Dingle temperature $T_D$ can also be estimated using the amplitude of the oscillation maximum and plotting them against the corresponding field value. The data can then be fit to the LK formula using the thermal damping factor $R_D$. From the fit, we get $T_D = 8\pm2$ K. Using the value of $T_D$, the relaxation time $\tau_q$ can be calculated. The carrier mobility

$\mu_q$ can then be determined [180], where $\tau_q = \frac{\hbar}{2\pi K_B T_D}$, and $\mu_q = \frac{e\tau_q}{m^*}$. Using $T_D = 8$ K, the relaxation rate was found to be $\tau_q = 1.5\times\ 10^{-13}$ s, and hence the mobility $\mu_q = 1465$ cm$^2$/Vs. This collective analysis indicates the $\alpha$ frequency corresponds to a topologically non-trivial mode.

## 4.5 Conclusion

To conclude, high quality single crystals of BiPd were synthesized. From multiple XRD measurements, we determined the structure to be $\alpha$-monoclinic with space group $P2_1$. A sharp superconducting transition was found in both transport and magnetization measurements at $T_c = 3.8$ K. The discrepancy between the estimation of the uppercritical fields, as well as surface probe measurements, point toward a complex superconducting behavior, where an unconventional superconducting order parameter was suggested. The existence of a topological superconducting state was not excluded, and this motivated us to investigate the quantum oscillations in BiPd.

The dHvA quantum oscillations in the magnetization of high-quality single crystals of the NCS superconductor BiPd were analyzed. FFT analysis revealed multiple frequencies associated with a complex Fermi surface. The small frequency at 40 T was found to be three dimensional and anisotropic. The LK fit and further phase analysis confirmed a non-trivial $\pi$ Berry phase is associated with this small pocket and a high mobility, pointing strongly to the Dirac-like nature of the carriers. A non trivial Berry phase in the bulk band points toward the possibility of topological states in this compound. This is consistent with the recent findings of the topological surface states in BiPd [174, 176]. Although this particular Fermi pocket is quite small, if this band corresponds to one of the superconducting bands, it can impact the topological nature of the superconductivity. Considering the existence of non-trivial Berry phase associated with a 3 dimensional Fermi pocket, our findings add to the array of interesting properties observed in BiPd and provide further motivation to establish the true nature of the bulk superconductivity and potential topological superconductivity in this compound.

# Chapter 5
# Magnetic Ordering in *B20* Compound $Ru_{1-x}Co_xGe$

## 5.1 Introduction

In the previous chapters, we have discussed NCS superconductors and the effect of broken inversion symmetry on their properties. The NCS structure coupled with the anti-symmetric spin orbit coupling associated with it, can also cause interesting phenomena to emerge in magnetic systems. A wide variety of magnetic systems have been found to host non-collinear magnetic structures due to the lack of inversion symmetry, such as the magentic skyrmion lattice in *B20* systems [70, 71], and magnetic chiral solitons [72], for example. Interestingly, topological skyrmions were first predicted by Tony Skyrme in the field of high energy particle physics [76, 77], but they turn out to be of great importance in condensed matter physics, as low energy excitations in topological materials that are NCS. In these magnetic compounds, the noncentrosymmetry offers the chance to observe the effects of an antisymmetric exchange interaction (also called the Dzyaloshinsky-Morya (DM) interaction) coexisting with ferromagnetic interactions [86, 87]. The competition between the symmetric exchange interaction and the anti-symmetric DM interaction results in the formation of helical magnetic ground states, since the DM interaction is lower in energy than the isotropic exchange interaction [70]. The non-collinear spin textures appear just below the magnetic transition in a narrow field ($H$) and temperature ($T$) region [80, 194]. The crystal anisotropy, third in the energy scale among all the interactions in *B20* cubic systems, pins the wave vector $q$ of the helix in a certain crystallographic direction [70]. Since this energy is rather small, the wave vector $q$ will be able to rotate in small fields to align with the external field direction.

The exotic magnetism found in transition metal silicides and germanides having the *B20* crystal structure has fascinated condensed matter physicists for decades. The most cel-

ebrated of these is MnSi, which has been investigated as a long wavelength helimagnet [82], a prototypical weak itinerant ferromagnet [83], a possible pressure induced quantum critical system [84], and most recently, as a host for a skyrmion lattice [85]. This class of compounds also includes FeGe, $Fe_{1-x}Co_xSi$, and MnGe, all of which are helimagnets because of the importance of the DM interaction in NCS systems. The occurrence of the skyrmion lattice phase is intimately connected to the helimagnetism having a characteristic wavevector that matches the helimagnetic (HM) wavevector, $q$, for each of these systems, despite the wide range of $q$'s displayed (ranging from $0.09\ \mathrm{nm}^{-1}$ in FeGe [195] to $2.1\ \mathrm{nm}^{-1}$ in MnGe [196]). The case of $Fe_{1-x}Co_xSi$ is particularly interesting to us, since the magnetism results from carrier doping the small band gap insulator FeSi to create a magnetic semiconductor [197]. In addition, the two parent compounds, FeSi and CoSi (a diamagnetic semimetal), have no intrinsic magnetic moments, let alone a magnetic transition.

RuGe is diamagnetic and a small band gap insulator, which crystallizes in the *B20* cubic structure. Interestingly, CoGe is also non-magnetic and a semimetal with a Dirac point just below the Fermi level and crystallizes in the *B20* structure when grown under pressure [198]. Doping Co for Ru nucleates magnetic moments and results in a magnetic ground state. In the following sections, we will discuss the synthesis and measurements of magnetic and transport properties of single crystalline $Ru_{1-x}Co_xGe$ (x = 0.1, 0.15, & 0.20, nominal). Single crystals of $Ru_{1-x}Co_xGe$ (x = 0.1, 0.15, & 0.20, nominal) were synthesized, and both powder and single crystal XRD performed on those crystals confirmed the *B20* structure. From the ac susceptibility measurement under ambient pressure, a magnetic transition was observed at around 5 K for nominal $Ru_{0.9}Co_{0.1}Ge$, 6.2 K for nominal $Ru_{0.85}Co_{0.15}Ge$, and 8.5 K for nominal $Ru_{0.8}Co_{0.2}Ge$. Magnetization measurements suggest a low saturation moment, where the overall behavior is akin to other *B20* compounds, such as MnSi and $Fe_{1-x}Co_xSi$. Among the *B20*s, $Ru_{1-x}Co_xGe$ is only the second example, after $Fe_{1-x}Co_xSi$, in which magnetism was found by chemical substitution between a nonmagnetic insulator (RuGe) and a non-magnetic semimetal (CoGe). Transport measurements

are similar to the behavior of $Fe_{1-x}Co_xSi$, where a complex resistivity consistent with a small band gap and strong correlation effects was observed with decreasing temperature. The magnetoresistance is positive and increases nearly linearly with field. While pure RuGe has a positive thermopower (Seebeck coefficient) at all temperatures [199], $Ru_{1-x}Co_xGe$ (x = 0.1, 0.15, & 0.2, nominal) has a negative thermopower. These measurements suggest that the introduction of Co has induced a small density of negative charge carriers as well as magnetic moments.

## 5.2 Experimental Description

Single crystals of a series of Co-doped RuGe were synthesized using a modified Bridgman technique in an rf-induction melting furnace. A series of 10%, 15%, and 20% nominal Co-doped RuGe was attempted to be made in single crystal form. About 10 grams of elementary Ru (alfa aesar 99.999%), Co (alfa aesar 99.99%) and Ge (alfa aesar 99.999%) were weighed out, and the stoichiometric mixture was put in an alumina crucible. For each growth, about 10% extra Ge was added to the total weight to act as a flux. A polycrystalline ingot was made from this initial mixture by melting it in the rf-induction furnace. The ingot was then ground to powder and placed in a doubly-tapered graphite crucible with a pointed bottom. The graphite crucible was then placed inside a quartz tube and sealed under vacuum. The tube was placed inside the rf coil suspended by the crystal puller. Ground polycrystalline Co-doped RuGe was slowly melted, and then the tube was lowered through the heating zone at 1-1.5 mm/hr, while keeping the melt inside the heating zone, at the same temperature. After 3 days of growth, a large single crystal was found, which can be seen in Fig. 5.1.

The single crystals of $Ru_{1-x}Co_xGe$ ($x = 15$ and 20) were mounted onto separate glass fiber tips using epoxy, attached to a goniometer head via the ends of brass pins, and the goniometer setup was placed on a Nonius Kappa CCD X-ray diffractometer equipped with Mo–K$\alpha$ radiation ($\lambda = 0.71073$ Å). The cubic Laue symmetry $m-3$ and systematic absences led to the space group selection of $P2_13$ (No. 198). The generation of the initial

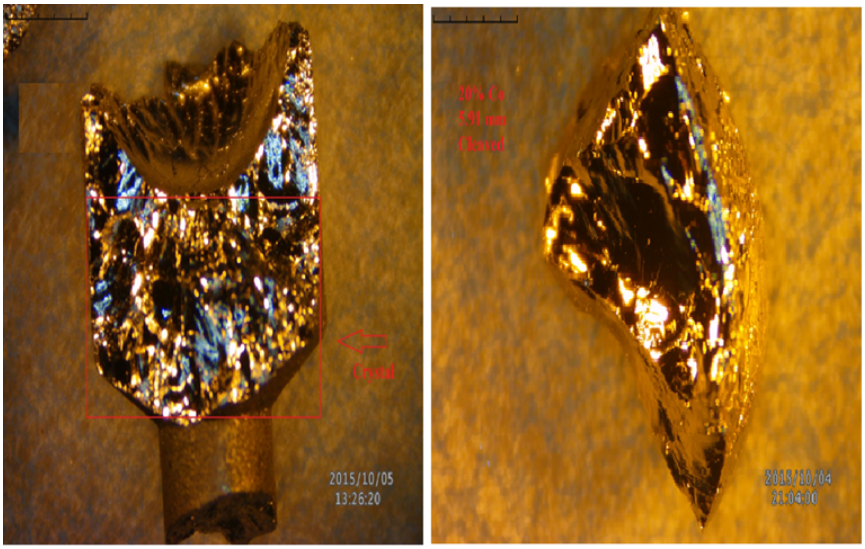


Figure 5.1: Single crystals of a series of Co-doped RuGe.

model and subsequent structure refinement were conducted using SIR97 and SHELX97, respectively[200, 201]. All models were corrected for extinction (SHELXL method), as well as absorption (multi-scan method)[202]. After locating all the atomic positions, the displacement parameters were refined as anisotropic, and weighting schemes were applied during the final stages of the refinement.

The crystal structure and phase purity of the crystalline samples were also investigated by powder X-ray diffraction (XRD) using a small portion of a powdered sample on a PANalytical Empyrean multi-stage X-ray diffractometer with Cu K$\alpha$ radiation ($\lambda$ = 1.54 Å). The system has a $\theta$-2$\theta$ geometry, and data were taken from 10° to 90° at a constant scan of 2° per minute at room temperature.

Further crystal structure measurements and an attempt to solve the magnetic structure were made on the four circle beam line (HB3A) of HFIR at ORNL [203]. This particular beam line is suitable to solve the magnetic structure, as well as identify any phase transitions. The four-circle dffractometer goniometer has a full $\chi$ circle with a 4.5–450 K closed-cycle helium refrigerator with a $^3$He detector. A multilayer-[110]-silicon wafer monochromator was used, with the reflection from planes of the $< 011 >$ zone. This ensures sharp diffraction peaks over the specified ranges of detector angles by control of the

horizontal radius of curvature and the fixed monochromator angle of 48°. Wavelengths of 1.003, 1.542, and 2.541Åcan be achieved [203]. For our experiment we used the wavelength of 2.541Å which has $\sim 2.28\%\ \lambda/2$ contamination [203].

Once the analysis on HB3A was completed, further investigation of the magnetic structure was performed on the small angle neutron scattering beam line GP-SANS [204] at HFIR. SANS is a useful tool for investigating microstructures, such as the flux lattices in superconductors, ferrofluids, and the relationship between structural and magnetic domains and ordering in magnetic materials. Furthermore, it allows for probing structural information on length scales ranging from 0.5-200 nm with a Q range as low as 0.0007 Å while allowing up to 20 m of sample-to-detector distance [204].

The electrical resistivity was measured using a standard four-probe ac technique at 27 Hz with an excitation current of 1-3 mA, in which small diameter Pt wires were attached to the sample using a conductive epoxy (Epotek H20E). Data were collected between 1.8 to 290 K and in magnetic fields up to 9 T using a Quantum Design, Physical Property Measurement System (PPMS). The specific heat was measured in the PPMS using a time-relaxation method between 2 and 20 K at 0 and 9 T. Magnetic susceptibility was also measured in the PPMS and in a Quantum Design XL-7 SQUID Magnetometer.

Thermoelectric power, or Seebeck coefficent ($S$), was measured by a comparative technique in the PPMS from 350 K to 2 K using a home-built sample holder with a constantan metal standard. The Seebeck coefficient is the ratio of voltage that develops divided by the temperature gradient across a sample [205]. The thermoelectric power depends on several intrinsic parameters of a compound via the thermoelectric figure of merit ZT, which is described by the equation below [205],

$$ZT = \frac{\sigma S^2 T}{\kappa}. \tag{5.1}$$

where, $\sigma$ is the electrical conductivity, and $\kappa$ is the thermal conductivity. The sign of the Seebeck coefficient usually indicates the majority carrier in the compound. Fig. 5.2 shows

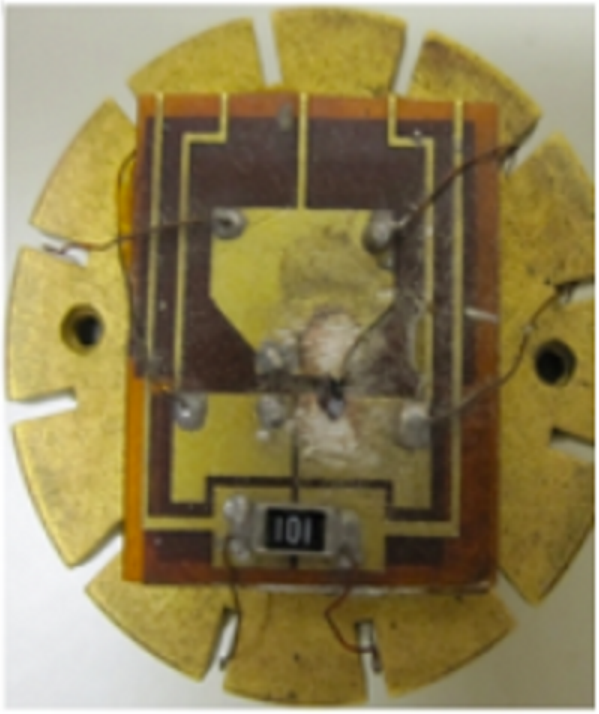


Figure 5.2: MMR stage mounted to Quantum Design puck used in the thermopower measurement. The illustration was taken from Ref. [97]

a typical MMR puck used to measure the thermopower in the PPMS. Here, a constantan metal standard with a known thermopower value ($S_c = 40\mu V/K$) is used with a heater, a 1000 Ω chip resistor, and a space for a rod shaped sample to be mounted. Usually the sample and the standard are approximately the same size, and one end of them is kept in contact with the heater. [97] When the heater is turned on for a very short amount of time, one end of both the sample and standard heat up, and a temperature gradient is created. As a result, the thermoelectric voltage is developed across each of them, and thus the Seebeck coefficient can be described by:

$$S_s = \frac{\Delta V_s}{\Delta T_s}. \tag{5.2}$$

$$S_c = \frac{\Delta V_c}{\Delta T_c}. \tag{5.3}$$

Since the temperature difference across both the sample and constantan standard is the same, the Seebeck coefficient for the sample can be estimated using [97],

$$S_s = \frac{\Delta V_s}{\Delta V_c} \times S_c. \tag{5.4}$$

The temperature control is achieved via the PPMS, whereas the voltage and the heater are controlled through external electronics using two Keithley voltmeters and a current source. The complete operation is controlled via LabView software, which records the voltage difference and calculates the Seebeck coefficient automatically.

## 5.3 Results and Discussions

### 5.3.1 Crystal Structure and Electronic Band Structures

A series of Co-doped RuGe samples was synthesized in single crystal form, and among them, 10, 15 and 20% Co-doped samples were analyzed thoroughly to check for phase purity and actual Co concentration in the sample. The result of single crystal XRD of 20% nominal Co-doped sample can be seen in Fig. 5.3(a). From the XRD the crystal was identified to be in space group $P2_13$ with a lattice parameter of $a = 4.8340 \pm 0.0002$Å. A similar result was obtained for the 15% nominal Co-doped sample. Phase purity is also evident from the powder XRD as seen in Fig 5.3(b) , from the peak to peak comparison to the pure RuGe, all the samples are seen to be in correct *B20* cubic phase.

After the powder XRD showed single-phase samples with the *B20* cubic phase in space group $P2_13$, we attempted to determine the actual Co concentration in the nominally 15% and 20% Co-doped samples. Attempts to grow crystals beyond 20% nominal Co-doped RuGe were unsuccessful, which indicates a Co solubility limit at ambient pressure. Furthermore, it is known that pure CoGe only forms in the *B20* crystal structure under pressure [198], and thus it was necessary to investigate to what extent Co could be doped in

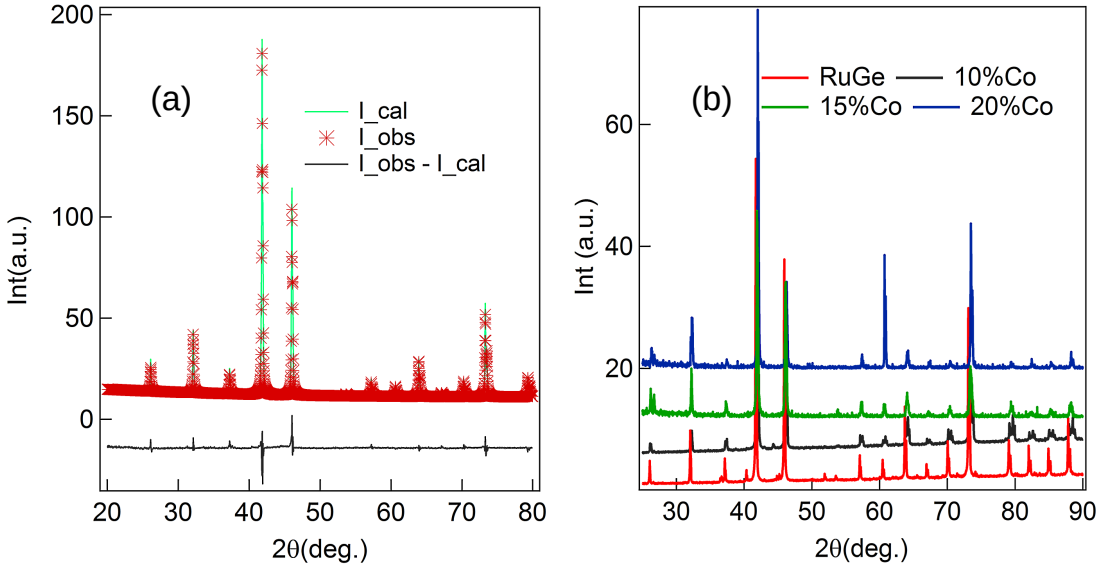


Figure 5.3: (a) Single crystal XRD of 20% nominal Co-doped RuGe. Rietveld refinement to the data showed the sample to be in *B20* cubic structure. (b)Powder XRD of single crystals of the series of Co-doped RuGe. A small amount of single crystals were ground to perform the XRD. The Red curve indicates the expected peak postions for the *B20* structure.

RuGe under ambient pressure. Elemental analysis of the single crystals was done utilizing both EDS and WDS. Data from both of the experiments showed that the samples are extremely homogeneous in composition with a small number of defects. Elemental analysis from both EDS and WDS showed that the actual Co concentration in 20% nominal Co-doped sample was about $\sim 4.8\%$, where as for 15%, it was $\sim 4.7\%$, suggesting the solubility limit had been reached. Data from the WDS analysis on the 20% nominal Co-doped sample can be seen in the Table. 5.1.

To investigate the possibility of an ordered magnetic ground state in Co-doped RuGe, we analyzed the electronic band structure of both the pure and doped material. It was reported earlier that pure RuGe [199] is a small band gap, $\sim 20meV$, insulator and diamagnetic, similar to FeSi [206]. The electronic band structure was calculated using the same LAPW method in the WIEN2K software as was done for $Re_6Zr$. From the DOS of pure RuGe, shown in Fig. 5.4(a), it is evident that it does not contain any states at the

Table 5.1: Elemental composition of 20% nominal Co-doped RuGe. From the WDS data, it was evident that the solubility limit under ambient pressure is about 4.8%.

| Element | Mass% | Norm% | Atom% | Error% |
|---|---|---|---|---|
| Ge | 43.376 | 43.415 | 50.624 | 0.32 |
| Ru | 53.219 | 53.266 | 44.6095 | 0.21 |
| Co | 3.316 | 3.319 | 4.7665 | 0.65 |
| Total | 99.911 | 100 | 100 | |

Fermi energy, and thus is a semiconductor with no Pauli paramagnetic contribution to its magnetic susceptibility.

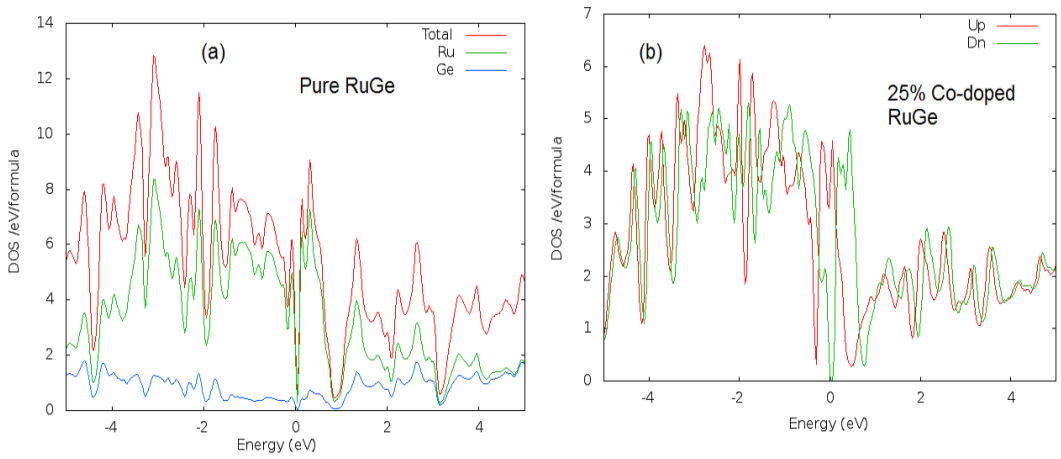


Figure 5.4: Theoretical calculation of electronic DOS of pure and doped RuGe. (a) Pure RuGe, where there are no states at the Fermi energy. (b)The 25% nominal doped RuGe, where there is a sharp peak in the DOS at Fermi level, indicating magnetism, since all the states are from a spin-up component.

The 25% electron doped i.e. Co-doped RuGe in Fig. 5.4(b) was simulated in the rigid band approximation where the valance electron count was increased to the level of 25% Co doping. At this doping concentrations, the Fermi level moves up into the peak in the DOS above the small band gap as carriers are added. A nonzero DOS now appears at the Fermi energy, indicating carrier availability for transport and the emergence of magnetism. All of the states are from a spin-up component, which immediately points toward possible half-

metallic and magnetic behavior as was shown to be the case for $Fe_{1-x}Co_xSi$ for $x$<0.3 [91, 207]. Our original goal was to create an ordered magnetic state in Co-doped RuGe in the hopes of realizing a helimagnetic or skyrmion phase in another *B20* system. The band structure calculations above at least suggested the doped samples should be magnetic, and this was verified through magnetization measurements (below).

### 5.3.2 Magnetization

Once the samples were analyzed via XRD and the phase purity was confirmed, we performed measurements to check for magnetic order. The magnetic measurements were performed in a SQUID. First, we measured the AC susceptibility with an excitation field of 10 Oe and frequency of 99.99 Hz. The mass of a small piece of the crystal was measured, and then the sample was placed in a plastic straw and inserted into the sample coil of SQUID. The results of the AC susceptibility measurements are shown in Fig. 5.5.

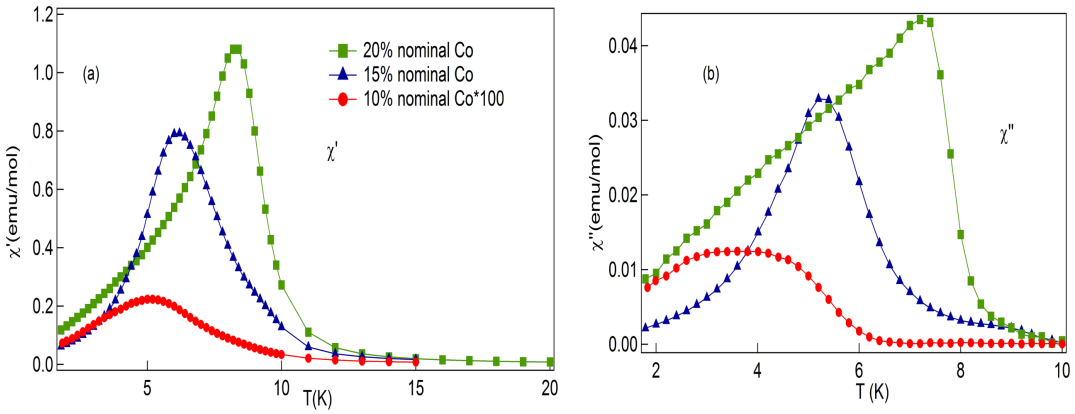


Figure 5.5: AC susceptibility of Co doped RuGe. (a) Real part of the AC susceptibility showing a broad maximum for the 10% Co-doped sample, whereas for the 15 & 20% samples, a sharp peak indicates magnetic ordering, in contrast to pure RuGe, which is diamagnetic. (b) Imaginary part of the AC susceptibility. The magnetic ordering is also observed in the imaginary part. The 10% Co-doped data were magnified for comparison purposes.

The AC susceptibility measurement clearly indicates magnetic ordering in Co-doped

RuGe. For 10% nominal Co-doped RuGe, both the real and imaginary parts show a broad maximum around 5 K, indicating the magnetic ordering temperature (Curie temperature, $T_C$). Interestingly, 15% Co-doped RuGe, has a sharp peak in both the real and imaginary part of the AC susceptibility at a higher temperature (6.5 K), suggesting a higher Co concentration. Finally, the 20% nominal Co-doped sample shows the highest ordering temperature at 8.5 K, with a sharp peak in the real and imaginary parts of the AC susceptibility. The systemic increase in ordering temperature indicates the Co concentration scales with increased doping.

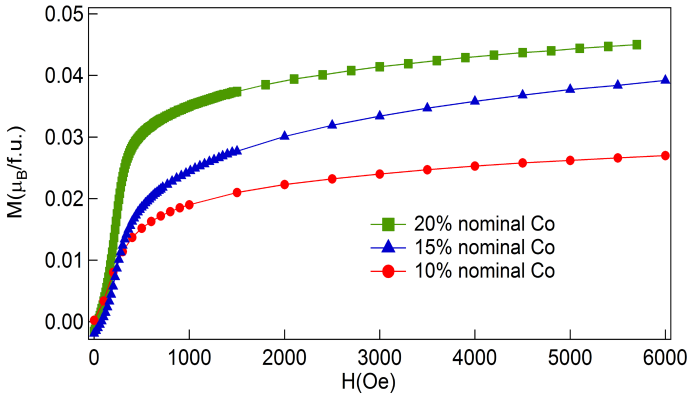


Figure 5.6: Magnetization at 1.8 K. The saturation moment increases uniformly as the Co concentration increases. For the 20% sample, the saturation moment is about 0.045 $\mu_B/f.u.$, f.u. stands for formula unit.

The *M(T)* and *M(H)* curves provide additional information on the nature of magnetic ordering, including the values of the fluctuating and saturation moment associated with the compounds. Here, a large low field contribution to the moment was observed in the *M(H)* curve as seen in Fig. 5.6, suggesting the magnetic order is ferromagnetic. This result is similar to that of MnGe, FeGe, and MnSi [198], where there is a steep increase in *M(H)* below $T_c$ at low field, which ends with a near saturation at high field. The ordered moment increases with increasing Co concentration. The highest ordered moment was found for the 20% nominally Co-doped sample (Fig. 5.6). Importantly, in the magnetic *B20* compounds such as MnSi, FeGe and Co doped (>10 %) FeSi, there is clear sign in *M(H)* data that indicates the existence of multiple magnetic phases with a helical ground

state. For example, in the magnetization increases in stepwise fashion, transitioning from helical to conical phase and then to spin polarized phase in higher field. While Co-doped RuGe at the present nominal doping concentrations do not show similar behavior.

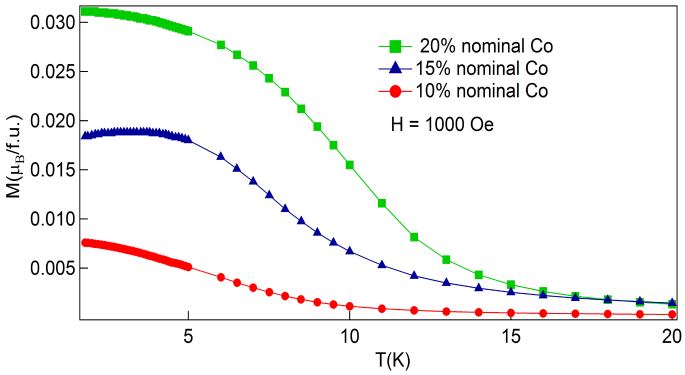


Figure 5.7: Magnetization under constant field of 1000 Oe. A ferromagnetic ordering was found for all of the doped compounds. The ordered moment is the lowest for the 10% Co-doped sample and increases for the nominal 15 & 20% samples.

As seen in Fig. 5.7, the *M(T)* data suggests a ferromagnetic ordering at the transition temperatures observed in the AC susceptibility. From the inverse DC molar susceptibility, i.e. M vs T curve, the data can be fit with a Curie-Weiss law (Fig. 5.8) as discussed in the second chapter. Since the 20% sample had the highest ordered moment, we focused on this compound for further analysis. The fluctuating moment above $T_c$ for the 20% sample was found to be 1.29 $\mu_B/Co$ using the measured Co concentration from WDS, with a positive Weiss temperature of 17.8±0.2 K (Fig. 5.8).

From the *M(H)* data below the ordering temperature, we can estimate the saturation moment. The data at 1.8 K for the three different Co-doped samples are shown in Fig. 5.6 which shows that, the saturation moment is lowest for the lowest Co-doped sample, which is consistent with the *M(T)* and AC susceptibility measurements. Presumably, Co dopes into the Ru site, as supported by the WDS data. The solubility limit is reached at ∼4.8% doping, which also has the highest saturated moment of 0.045 $\mu_B/f.u.$ or 0.9 $\mu_B/Co$. This is smaller than the effective moment calculated from the Curie-Weiss fit to the reciprocal molar susceptibility (Fig. 5.8). This difference indicates the itinerant nature of the magnetism,

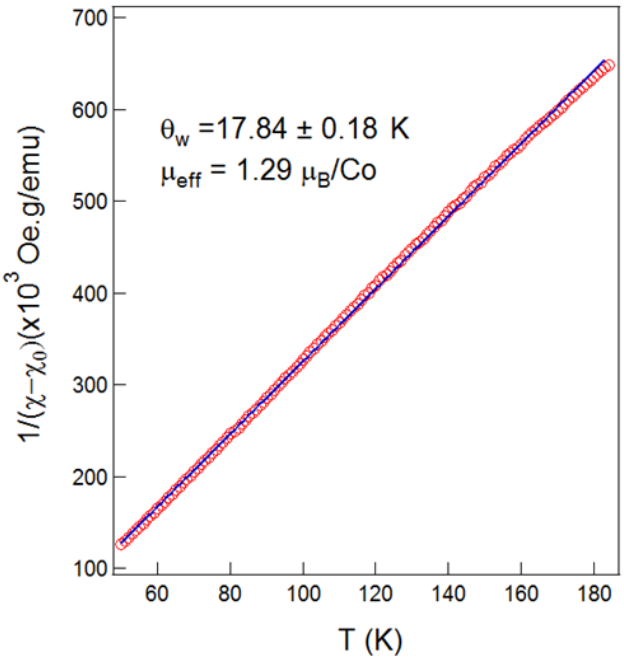


Figure 5.8: Curie-Weiss fit to the magnetization data of the 20% nominal Co-doped sample. A paramagnetic background was subtracted prior to the fit. The solid line is the Curie-Weiss fit as discussed in Chapter 2.

which is similar to other B20 compounds, such as MnSi [208]. The Rhodes-Wohlfarth ratio (RWR), which is the ratio of the effective moment to the saturation moment, $\frac{\mu_{eff}}{\mu_{sat}}$, is a measure of the itinerancy of the magnetism [209]. A value of 1.00 would indicate a local moment system. Using the data for the 20% sample, the RWR is 1.43, suggesting that Co-doped RuGe is a weak itinerant ferromagnet [210]. Much larger ratios are found in other ferromagnetic materials, such as $LaFe_4As_{12}$, where the RWR is 32, which indicates a very strong itinerant nature of the magnetism [211]. The results on Co-doped RuGe are consistent with other B20 compounds, which are also weak ferromagnets with itinerant moments inferred from the RWR value. For example, MnSi has a RWR as high as 3.5 [210]. For Co-doped FeSi, the RWR value consistently increases with increasing Co concentration and assumes a maximum (>6.0) at ∼70% Co-doping level [91].

The hysteresis in magnetization at 1.8 K for the 20% sample is shown in Fig. 5.9. There

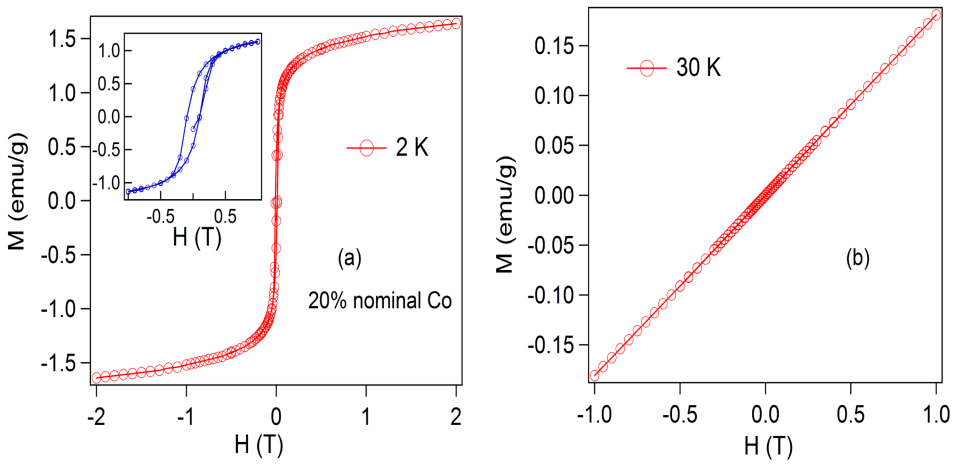


Figure 5.9: Magnetic hysteresis curve for the 20% sample at 1.8 K (a) and 30 K (b). (a) Ferromagnetism with a small hysteresis was observed below the Curie temperature. (b) A similar measurement at 30 K shows paramagnetism consistent with the ferromagnetic ordering below 8.5 K. Inset: Small hysteresis around 500 Oe at T = 1.8 K.

is a small hysteresis below the $T_c$ which, can be due to magnetic domain effect. The data are consistent with ferromagnetic ordering below 8.5 K. At 30 K, paramagnetic behavior was found with no magnetic coercivity i.e. hysteresis. It is important to note that, the above magnetic measurements suggest weak itinerant ferromagnetism and are similar to Co-doped FeSi [90, 207, 212] with low Co concentration(<5%).

### 5.3.3 Resistivity and Seebeck Coefficient

Similar to FeSi [213], the resistivity of pure RuGe, a small band gap semiconductor, shows a characteristics of slight carrier doping [214]. The temperature dependent resistivity can be divided into three regions: (1) A low temperature region dominated by e-e interaction similar to Co-doped FeSi [215], (2) a metallic behavior at intermediate temperatures, and beyond that (3) a region upto measured maximum temperature of 290 K with either thermally activated or variable range hopping type conduction [214]. The Co-doped RuGe samples follow a similar trend, which can be seen in Fig. 5.10.

The resistivities of the Co-doped samples are less than pure RuGe (4.0 m$\Omega$.com) 5.10, and the transport data are similar to that of $Fe_{1-x}Co_xSi$ [207]. In the intermediate temper-

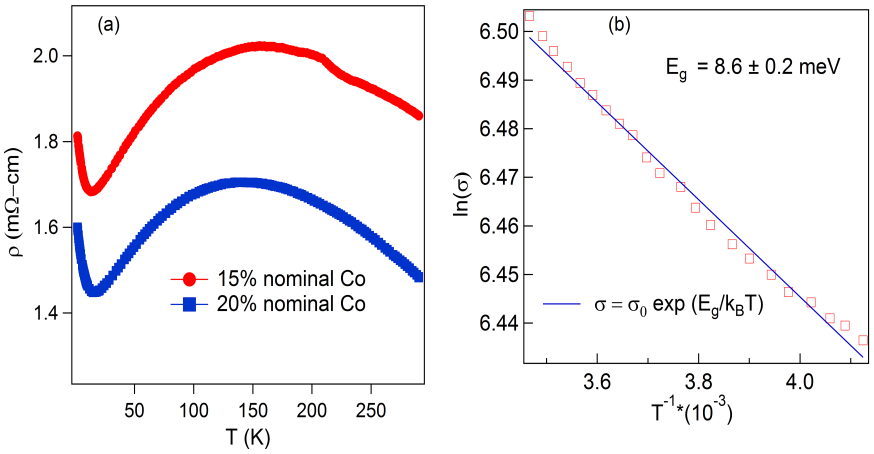


Figure 5.10: (a) Temperature dependent resistivity of Co-doped RuGe. The room temperature resistivity is much smaller than that of pure RuGe [214], with values typical of doped semiconductors. (b) Considering a thermally activated behavior in the temperature range 230 to 290 K, the band gap was estimated using the fit described in the text.

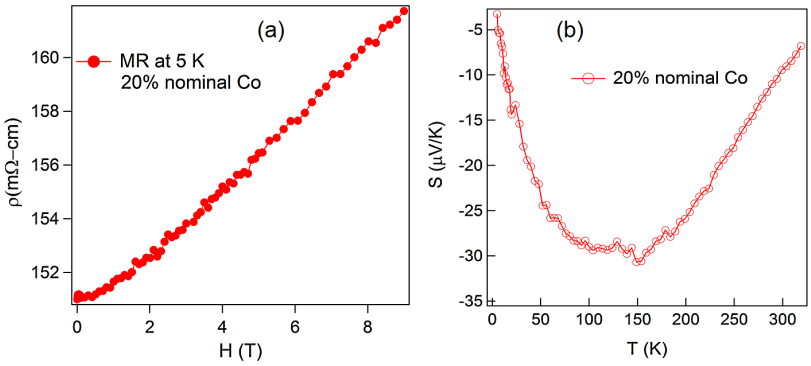


Figure 5.11: (a) Magnetoresistance at 5 K of the 20% sample. (b) Seeback coefficient of 20% nominal Co-doped RuGe. Solid line is a guide to the eye.

ature (110–20 K) behavior is metallic-like, since $\frac{d\rho}{dT} > 0$. An activated behavior is observed in the intermediate temperature region, 230 $\sim$ 290 K, which can be due to either hopping or thermal activation. If we consider activated behavior, we can find the band gap utilizing Arrhenius plot [214] as shown in Fig. 5.10(b).

Fitting the data in Fig. 5.10(b) returns a band gap of 8.6 meV for the 20% nominal Co-doped RuGe sample, which is smaller than the gap of pure RuGe (20 meV). This is consistent with the formation of an impurity band and additional electrons being added via Co doping. The kink or upturn in the resistivity at low temperature, i.e. 12 K, is

likely due to disorder and electron–electron interactions [216] in proximity to the metal–insulator transition. This is strikingly similar to that of $Fe_{0.95}Co_{0.05}Si$ [217][207]. The upturn in the resistivity is slightly higher in temperature than the Curie temperature. It is worthwhile to recall that the EDS and WDS data showed at 20% nominal doping, the actual Co concentration was about 5%. The resistance as a function of applied Field, i.e. magnetoresistance (MR), is shown in Fig. 5.11(a). The MR remains positive and increases with increase in field without any sign of saturation up to 9 T. Similar MR was also found in $Fe_{1-x}Co_xSi$ for small values of x [207].

The thermopower is another important property of semiconducting materials and is of interest from a practical standpoint for potential applications in electronic refrigeration and power generation. From the thermopower measurements the sign of the majority carriers can also be found. The Seebeck coefficient for pure RuGe is that of an intrinsic semiconductor with p-type conduction, i.e. the majority carriers are holes with a positive thermopower. [214]. The Co-doped RuGe, as seen in Fig. 5.11(b) for 20% sample, exhibits a negative Seebeck coefficient, and is therefore, an n-type conductor. With increasing temperature, the Seebeck coefficient moves over a broad maximum and then decreases, similar to pure RuGe and doped FeSi [207]. The room temperature value of Co-doped RuGe (-10 $\mu$ V/K) is smaller (and negative) compared to that of pure RuGe (+27 $\mu$ V/K). The n-type conduction in the doped sample clearly indicates the conversion of the majority carriers from holes to electrons, consistent with the doping, and a similar behavior is observed in Co-doped FeSi [207].

### 5.3.4 Heat Capacity

Heat capacity was measured for the 20% nominal Co-doped sample via a time relaxation method. The result of the heat capacity is shown in Fig. 5.12.

A transition is apparent in the heat capacity at the same temperature a magnetic transition was observed in the magnetic measurements, and thus corresponds to a bulk magnetic transition. From the total heat capacity data, the phonon contribution was

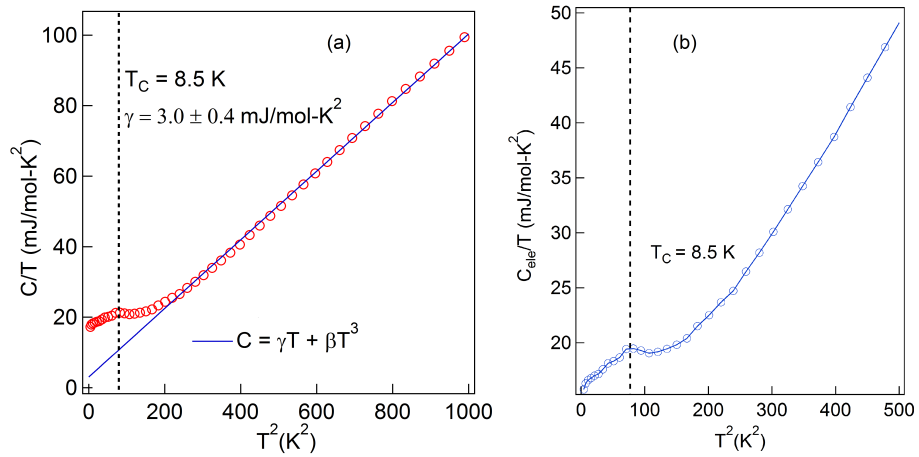


Figure 5.12: Heat capacity of doped RuGe as a function of temperature. (a) The total heat capacity of 20% Co-doped sample. The solid line is a fit to the data to estimate the phonon contribution. (b) The electronic heat capacity calculated from the fit in (a) as discussed in text. Solid line is a guide to the eye. Both parts of the heat capacity showed a transition at 8.5 K. The vertical dashed line indicates the Curie temperature.

estimated using the fit (Fig. 5.12(a)) of the form,

$$C = \gamma T + \beta T^3. \tag{5.5}$$

From the fit, the Sommerfeld coefficient is $\gamma = 3.0 \pm 0.4$ mJ mol$^{-1}$ K$^{-2}$ and the Debye coefficient $\beta = 0.0937 \pm 0.0007$ mJ mol$^{-1}$ K$^{-4}$. The Debye temperature can be estimated from the relation $\theta_D = (\frac{5\beta}{N12\pi^4 R})^{-1/3}$. For 20% sample, $\theta_D = 430$ K which is close to that of other B20 compounds, such as MnSi and doped FeSi.

The value of $\gamma$ suggests enhancement in density of states (DOS) for the doped sample compared to the pure RuGe, since the pure RuGe shows no apparent DOS (insulator) in the Fermi level from the electronic structure calculation. A similar trend was found in $Fe_{1-x}Co_xSi$ where the value of $\gamma$ is 3.4 mJ mol$^{-1}$ K$^{-2}$ for 5% Co doping concentration and increases upon further addition of Co [218, 219]. This phenomenon can be understood via the renormalization of noninteracting bands that resulted in the enhanced DOS at the gap edge and was also found in pure FeSi [220].

### 5.3.5 Neutron Scattering

Once the weak itinerant ferromagnetic behavior of $Ru_{1-x}Co_xGe$ was established, we set out to investigate the magnetic structure of $Ru_{1-x}Co_xGe$ using neutron diffraction techniques. We performed a neutron experiment at ORNL using the HB3A beam line with a four-circle diffractometer, which is a convenient tool for investigating and solving both the crystal and magnetic structures. Unfortunately, the small size of the ordered magnetic moment, $\mu_S = 0.045\ \mu_B$/f.u., prevented us from determining the magnetic structure. However, the crystal structure of $Ru_{1-x}Co_xGe$ with x = 0.2 nominal was found to be consistent with the results of the XRD analysis and is shown in Fig. 5.13.

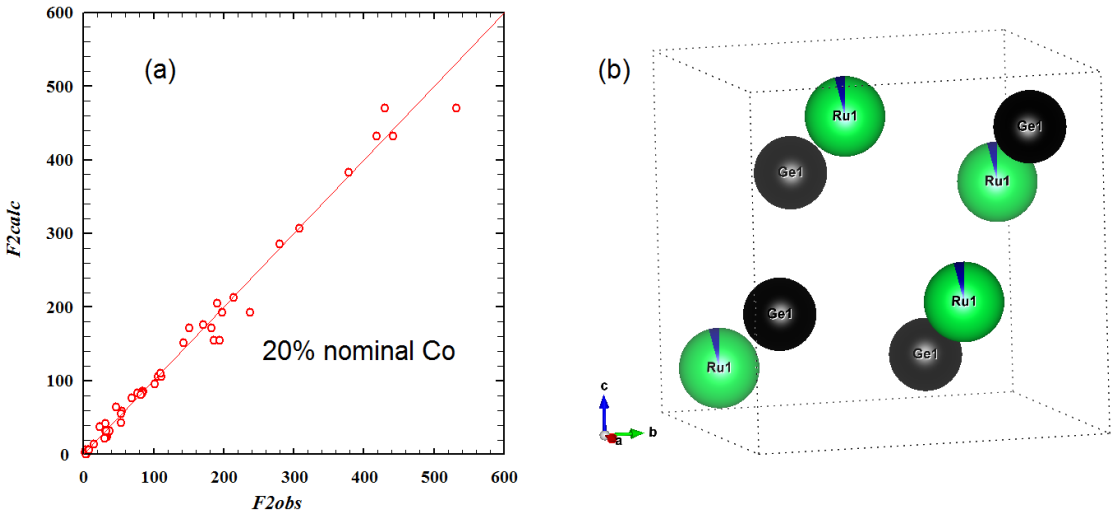


Figure 5.13: Neutron scattering data from single crystals of nominal $Ru_{0.8}Co_{0.2}Ge$ on the HB3A beam line of HFIR at ORNL. (a) The nuclear structure refinement matched well to the observed data, indicating the cubic $P2_13$ structure type. (b) Schematic illustration of the $Ru_{0.8}Co_{0.2}Ge$ structure, which shows the actual Co concentration was about 5%.

Since large length scale structures are better investigated through small angle neutron scattering (SANS), we further investigated the $Ru_{0.8}Co_{0.2}Ge$ sample using the GP-SANS instrument at HFIR. Unfortunately, small ordered magnetic moment of our sample again prevented us from observing any magnetic scattering, which is quite likely to be on the same scale as the incoherent scattering. However, to check for consistency, we measured a MnSi single crystal grown with Ga flux to verify its helimagnetic and skyrmion lattice

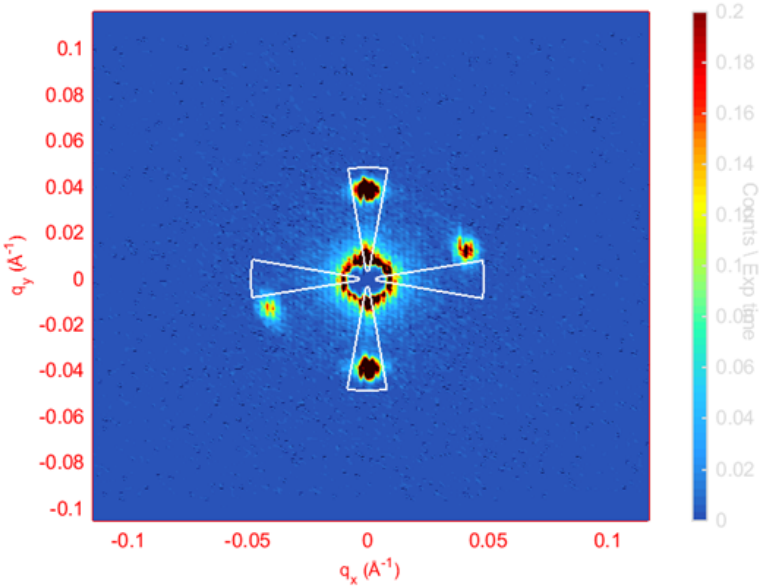


Figure 5.14: Small angle neutron scattering on $MnSi_{1-x}Ga_x$. The helical magnetic state is observed with four distinct spots, in agreement with previous work on MnSi [82]

phases. The results for $MnSi_{1-x}Ga_x$ are shown in Fig. 5.14.

## 5.4 Conclusion

In an effort to discover new materials that could possibly host emergent magnetic phenomena, such as magnetic skyrmions, we have synthesized and explored the behavior of single crystals of $Ru_{1-x}Co_xGe$ via a modified Bridgman technique. From the magnetization data, a clear magnetic transition was found for nominal x= 0.1, 0.15, and 0.2 Co-doped RuGe. From the detailed EDS and WDS analysis, the actual Co concentration was found to be much less, and a solubility limit was reached at 5%. This is not unexpected, as the other end member, CoGe, only forms in the B20 structure under high pressure. The resistivity is typical of that of a doped semiconductor with an activated or variable range hopping type behavior in the moderately high temperature range and metallic behavior at the intermediate temperatures. Electron-electron interactions dominate the magnetoresistance and are responsible for the upturn in resistivity below 20 K. The thermopower measurement showed a sign reversal for doped RuGe, indicating the majority carriers to be electron-like in

accordance with the electron doping. Heat capacity data also confirmed the bulk magnetic transition with an enhanced DOS at the Fermi level for higher Co concentrations.

Thus, we have discovered that Co substitution into the small band gap insulator RuGe having the B20 crystal structure results in a magnetic ground state. This is interesting and important for several reasons. First, it is the second example of magnetism found by chemically doping a nonmagnetic insulator (RuGe) into a non-magnetic semimetal (CoGe, also having the B20 crystal structure) [198], while long-range magnetic order emerges for intermediate concentrations. Second, it demonstrates that the presence of Fe is not necessary for nucleating a magnetic state in an FeSi-like cubic system. Third, given the similarities to FeSi and its doped variants, the magnetism is likely to be helimagnetic with q determined by an expectedly larger spin-orbit coupling, simply because of the larger atomic masses, compared to that of the silicides, FeGe, or MnGe. Naively, this would argue for a larger q that varies with x in a similar fashion to the case of $Fe_{1-x}Co_xSi$ [90]. Finally, it is likely that this system will also host a skyrmion lattice phase for finite magnetic fields whose properties may be different from those established in MnSi, MnGe, $Fe_{1-x}Co_xSi$, and FeGe. If indeed that is the case, then $Ru_{1-x}Co_xGe$ will be a germanide counterpart to FeSi and allow for an investigation of the effects of tuning spin-orbit coupling on the skyrmion phase.

However, attempts to investigate the possible helimagnetic ground state utilizing neutron diffraction techniques at the current doping level was hindered due to the low saturation moment, which is only a few ($\sim$4%) percent of a Bohr magneton. From the HB3A data, it was evident that the crystal structure was cubic with space group $P2_13$ and also can be refined with 5% Co doping in Ru site. Given that the saturation moment increases with Co concentration, we are motivated to produce samples with higher Co content, since even for FeSi, the helimagnetism and hence the skyrmion phase, can only be unequivocally resolved experimentally at doping levels above 5% Co with larger saturation moment. [90] Our future goal is to synthesize higher Co-content samples using high-pressure synthesis techniques and to complete the phase diagram $0 < x < 1$. Currently, a high-pressure fur-

nace is being commissioned in our laboratory in the Department of Physics & Astronomy.

# Chapter 6
# Summary and Outlook

In this dissertation, we have explored three NC systems in an effort to understand the effect of broken inversion symmetry and spin orbit coupling on the superconducting and magnetic properties of some selected intermetallic compounds. During this work, I have studied NC $Re_6Zr$, BiPd, and $Ru_{1-x}Co_xGe$ by investigating their structural, physical, magnetic and thermal properties by employing a variety of synthesis and characterization techniques. Our study has further illustrated that complex interactions in condensed matter systems in the presence of broken symmetries can lead to exotic magnetic ground states and novel superconductivity.

The NC superconductor $Re_6Zr$ shows complex behavior, with its resistivity, magnetic susceptibility, and specific heat measurements confirming it to be a strongly correlated, type-II superconductor with a bulk transition temperature near 6.7 K. The thermal conductivity is dominated by the phonon contribution near the superconducting transition and is enhanced below $T_c$ due to a decrease in electron-phonon scattering, as the electrons form quasiparticle pairs. The upper critical field $H_{c2}(0)$ is comparable to the calculated Pauli limit, which can be a consequence of the SO interaction or strong coupling, or it might also be due to the contribution from a triplet-pairing component to the superconducting order parameter. These measurements suggest that the superconducting behavior of $Re_6Zr$ deviates from that of conventional superconductors. However, the low temperature electronic specific heat and penetration depth indicate fully-gapped BCS type superconductivity. This is interesting, since the irreducible representation analysis [118] of the point group of $Re_6Zr$ showed that the order parameter may be anisotropic. However, current experimental data suggests the gap is isotropic, which is similar to the majority of the NC superconductors, where conflicting behavior restricts the order parameter. The smaller ASOC in $Re_6Zr$ compared to other unconventional NC superconductors, limits the amount of triplet component

contributing to the order parameter and is not experimentally discernible.

BiPd is another interesting NC superconductor, where the role of ASOC on its superconducting properties can be well understood, due to its weakly correlated nature. Due to the presence of a Dirac point below the Fermi level, it supports topological surface states as probed via ARPES and STM studies [174–176]. The presence of a ZBCP in STM and PCAR measurements indicates the realization of an Andreev Bound state indicating possibility of Majorana mode in the vortex core [66]. The presence of a Majorana fermionic mode is generally attributed to the presence of topological superconductivity. We studied the dHvA quantum oscillations in the magnetization of high-quality single crystals of BiPd. We observed clear oscillations at 350 mK and as high as 20 K. The periodic oscillations were analyzed via FFT, which revealed multiple frequencies associated with a complex Fermi surface. Among those, a small frequency at 40 T was found to be three dimensional and anisotropic. The LK fit and further phase analysis confirmed a non-trivial $\pi$ Berry phase is associated with this small pocket and a high mobility, pointing strongly to the Dirac-type nature of the carriers. A non-trivial Berry phase in the bulk band points toward the possibility of topological states in this compound and are consistent with other recent studies [174–176]. While this Fermi pocket is rather small, if this particular band corresponds to one of the superconducting bands, then the non-trivial topology of this band might influence the bulk superconductivity.

Symmetry principles play an important role in magnetism as well. In fact, the antisymmetric spin orbit coupling interaction that we have studied can only occur in systems where inversion symmetry is broken. As a consequence of antisymmetric exchange, a wide variety of magnetic systems have been found to host non-collinear magnetic structures, such as the magnetic Skyrmion lattice in the cubic *B20* systems [70, 71]. In an effort to discover new materials that could possibly host the Skyrmion lattice, we have synthesized and explored the behavior of single crystals of $Ru_{1-x}Co_xGe$ grown via a modified Bridgman technique. From the magnetization data, a clear magnetic transition was found for nominal x= 0.1,

0.15, and 0.2 Co-doped RuGe. From the detailed EDS and WDS analysis, the actual Co concentration was found to be much less, and a solubility limit was reached at 5%, which is consistent with the other end member, CoGe, only forming in the *B20* structure under high pressure. The resistivity is typical of that of a doped semiconductor with an activated or hopping behavior in the room temperature range and metallic behavior at intermediate temperatures. Electron-electron interactions dominate the magnetoresistance and are responsible for the upturn in resistivity below 20 K. The thermopower measurement showed a sign reversal for doped RuGe, indicating the majority carriers to be electron-like in accordance with the electron doping. Heat capacity data also confirmed the bulk magnetic transition with an enhanced DOS at the Fermi level for higher Co concentrations. Thus, we have transformed a diamagnetic insulator into a ferromagnetic semiconductor with electron doping.

This dissertation work demonstrates that antisymmetric spin-orbit interactions play an important role in the underlying physical properties of condensed matter systems with broken inversion symmetry. Further work is needed to fully understand and quantify how varying the strength of ASOC affects the individual superconducting or magnetic compounds. For example, a deeper analysis of the structure of the superconducting order parameter of $Re_6Zr$ will require the synthesis of single crystals. With single crystals, the anisotropic measurement of the upper critical field, NMR relaxation rates (Knight shift), penetration depth, as well as point probes, such as PCAR can be utilized. A complete investigation of the topological nature of BiPd is also imperative. High field (<50 T) dHvA measurements can be performed to study the Berry phase of several other frequencies that we have identified in our work. At higher field, the quantum limit can be reached for some of the frequencies. Further investigation of the temperature dependence of the frequencies identified thus far can also give insight into the quasi-particle mass, as well as their topological nature, when coupled with phase analysis. Even though we were successful in tuning in magnetic order in Co doped RuGe, an investigation of a possible helimagnetic ground

state utilizing neutron diffraction techniques at the current doping level was not possible due to the small ordered moment. Given that the saturation moment increases with Co concentration, we are motivated to produce samples with higher Co content, since even for FeSi, the helimagnetism, and hence the Skyrmion phase, appears at doping levels above 5% Co. [90]. Thus, future work should focus on the synthesis of higher Co-content samples using high-pressure synthesis techniques and to complete the phase diagram ($0 < x < 1$) of this series. At higher Co concentration, a larger ordered moment would allow neutron diffraction investigations of the magnetic structure, with the hope of revealing another rare example of the Skyrmion lattice.

> .....the grandest discoveries of science have been but the rewards of accurate measurement and patient long-continued labour in the minute sifting of numerical results. (Lord W.T. Kelvin) [221]

# References


[1] M. Tinkham, *Introduction to superconductivity* (Courier Corporation, 1996).

[2] "Inversion Symmetry," `http://symmetry.otterbein.edu/tutorial/inversion.html`, accessed: 09-30-2017.

[3] "SO interaction," `https://www.st-andrews.ac.uk/~dc43/PH4021/`, accessed: 09-30-2017.

[4] C. Kittel, *Introduction to solid state*, Vol. 162 (John Wiley & Sons, 1966).

[5] "Spectral Splitting," `http://hyperphysics.phy-astr.gsu.edu/hbase/quantum/hydfin.html`, accessed: 09-30-2017.

[6] W. Meissner and R. Ochsenfeld, Naturwissenschaften **21**, 787 (1933).

[7] W. H. Keesom and J. N. Van den Ende, P K Akad Wet-Amsterd **35**, 143 (1932).

[8] V. L. Ginzburg and L. D. Landau, Zh. Exsper. Teor. Fiz. **20**, 10641 (1950).

[9] A. A. Abrikosov, Soviet Physics Jetp-Ussr **5**, 1174 (1957).

[10] J. Bardeen, L. N. Cooper, and J. R. Schrieffer, Phys. Rev. **106**, 162 (1957).

[11] L. N. Cooper, Phys. Rev. **104**, 1189 (1956).

[12] L.-P. Lévy, *Magnetism and superconductivity* (Springer Science & Business Media, 2013).

[13] J. Bardeen, L. N. Cooper, and J. R. Schrieffer, Phys. Rev. **108**, 1175 (1957).

[14] M. Smidman, *Superconducting and magnetic properties of non-centrosymmetric systems*, Ph.D. thesis, University of Warwick (2014).

[15] M. Sigrist, A. Avella, and F. Mancini, in *AIP Conference Proceedings*, Vol. 789 (AIP, 2005) pp. 165–243.

[16] R. Hott, R. Kleiner, T. Wolf, and G. Zwicknagl, in *Frontiers in Superconducting Materials* (Springer, 2005) pp. 1–69.

[17] R. P. Singh, A. D. Hillier, B. Mazidian, J. Quintanilla, J. F. Annett, D. M. Paul, G. Balakrishnan, and M. R. Lees, Phys. Rev. Lett. **112**, 107002 (2014).

[18] E. Bauer and M. Sigrist, *Non-centrosymmetric superconductors: introduction and overview*, Vol. 847 (Springer Science & Business Media, 2012).

[19] E. I. Rashba, Sov. Phys. Solid State **2**, 1109 (1960).

[20] L. P. Gor'kov and E. I. Rashba, Phys. Rev. Lett. **87**, 037004 (2001).

[21] F. Kneidinger, E. Bauer, I. Zeiringer, P. Rogl, C. Blaas-Schenner, D. Reith, and R. Podloucky, Physica C **514**, 388 (2015).

[22] P. W. Anderson, Phys. Rev. B **30**, 4000 (1984).

[23] P. A. Frigeri, D. F. Agterberg, A. Koga, and M. Sigrist, Phys. Rev. Lett. **92**, 097001 (2004).

[24] M. Sigrist, D. Agterberg, P. Frigeri, N. Hayashi, R. Kaur, A. Koga, I. Milat, K. Wakabayashi, and Y. Yanase, J. Magn. Magn. Mater. **310**, 536 (2007).

[25] Frigeri, P. A., Agterberg, D. F., Milat, I., and Sigrist, M., Eur. Phys. J. B **54**, 435 (2006).

[26] P. A. Frigeri, D. F. Agterberg, and M. Sigrist, New Journal of Physics **6**, 115 (2004).

[27] E. Bauer, G. Hilscher, H. Michor, M. Sieberer, E. Scheidt, A. Gribanov, Y. Seropegin, P. Rogl, W. Song, J.-G. Park, *et al.*, Czechoslovak Journal of Physics **54**, 401 (2004).

[28] E. Bauer, G. Hilscher, H. Michor, C. Paul, E. W. Scheidt, A. Gribanov, Y. Seropegin, H. Noël, M. Sigrist, and P. Rogl, Phys. Rev. Lett. **92**, 027003 (2004).

[29] N. Metoki, K. Kaneko, T. Matsuda, A. Galatanu, T. Takeuchi, S. Hashimoto, T. Ueda, R. Settai, Y. Ōnuki, and N. Bernhoeft, Journal of Physics: Condensed Matter **16**, L207 (2004).

[30] K. Izawa, Y. Kasahara, Y. Matsuda, K. Behnia, T. Yasuda, R. Settai, and Y. Onuki, Phys. Rev. Lett. **94**, 197002 (2005).

[31] T. Takeuchi, T. Yasuda, M. Tsujino, H. Shishido, R. Settai, H. Harima, and Y. Onuki, Journal of the Physical Society of Japan **76**, 014702 (2007), http://dx.doi.org/10.1143/JPSJ.76.014702 .

[32] K. V. Samokhin, E. S. Zijlstra, and S. K. Bose, Phys. Rev. B **69**, 094514 (2004).

[33] D. F. Agterberg, P. A. Frigeri, R. P. Kaur, A. Koga, and M. Sigrist, Physica B: Condensed Matter **378**, 351 (2006).

[34] R. L. Ribeiro, I. Bonalde, Y. Haga, R. Settai, and Y. Ōnuki, Journal of the Physical Society of Japan **78**, 115002 (2009).

[35] M. Yogi, H. Mukuda, Y. Kitaoka, S. Hashimoto, T. Yasuda, R. Settai, T. D. Matsuda, Y. Haga, Y. Ōnuki, P. Rogl, *et al.*, Journal of the Physical Society of Japan **75**, 013709 (2006).

[36] Y. Muro, D. Eom, N. Takeda, and M. Ishikawa, Journal of the Physical Society of Japan **67**, 3601 (1998).

[37] T. Kawai, H. Muranaka, M.-A. Measson, T. Shimoda, Y. Doi, T. D. Matsuda,

Y. Haga, G. Knebel, G. Lapertot, D. Aoki, J. Flouquet, T. Takeuchi, R. Settai, and Y. Onuki, Journal of the Physical Society of Japan **77**, 064716 (2008).

[38] R. Settai, Y. Miyauchi, T. Takeuchi, F. Lévy, I. Sheikin, and Y. Ōnuki, Journal of the Physical Society of Japan **77**, 073705 (2008).

[39] N. Kimura, K. Ito, H. Aoki, S. Uji, and T. Terashima, Phys. Rev. Lett. **98**, 197001 (2007).

[40] T. Akazawa, H. Hidaka, T. Fujiwara, T. Kobayashi, E. Yamamoto, Y. Haga, R. Settai, and Y. Ōnuki, Journal of Physics: Condensed Matter **16**, L29 (2004).

[41] S. Fujimoto, Journal of the Physical Society of Japan **75**, 083704 (2006).

[42] H. Q. Yuan, D. F. Agterberg, N. Hayashi, P. Badica, D. Vandervelde, K. Togano, M. Sigrist, and M. B. Salamon, Phys. Rev. Lett. **97**, 017006 (2006).

[43] P. Badica, T. Kondo, and K. Togano, Journal of the Physical Society of Japan **74**, 1014 (2005).

[44] H. Takeya, K. Hirata, K. Yamaura, K. Togano, M. El Massalami, R. Rapp, F. A. Chaves, and B. Ouladdiaf, Phys. Rev. B **72**, 104506 (2005).

[45] M. Nishiyama, Y. Inada, and G.-q. Zheng, Phys. Rev. Lett. **98**, 047002 (2007).

[46] K. Miliyanchuk, F. Kneidinger, C. Blaas-Schenner, D. Reith, R. Podloucky, P. Rogl, T. Khan, L. Salamakha, G. Hilscher, H. Michor, *et al.*, in *Journal of Physics: Conference Series*, Vol. 273 (IOP Publishing, 2011) p. 012078.

[47] F. Kneidinger, L. Salamakha, E. Bauer, I. Zeiringer, P. Rogl, C. Blaas-Schenner, D. Reith, and R. Podloucky, Phys. Rev. B **90**, 024504 (2014).

[48] E. Bauer, R. T. Khan, H. Michor, E. Royanian, A. Grytsiv, N. Melnychenko-Koblyuk, P. Rogl, D. Reith, R. Podloucky, E.-W. Scheidt, W. Wolf, and M. Marsman, Phys. Rev. B **80**, 064504 (2009).

[49] G. Eguchi, D. C. Peets, M. Kriener, Y. Maeno, E. Nishibori, Y. Kumazawa, K. Banno, S. Maki, and H. Sawa, Phys. Rev. B **83**, 024512 (2011).

[50] V. K. Anand, A. D. Hillier, D. T. Adroja, A. M. Strydom, H. Michor, K. A. McEwen, and B. D. Rainford, Phys. Rev. B **83**, 064522 (2011).

[51] A. D. Hillier, J. Quintanilla, and R. Cywinski, Phys. Rev. Lett. **102**, 117007 (2009).

[52] T. Shibayama, M. Nohara, H. A. Katori, Y. Okamoto, Z. Hiroi, and H. Takagi, Journal of the Physical Society of Japan **76**, 073708 (2007).

[53] P. Parab, D. Singh, H. Muthurajan, R. Singh, P. Raychaudhuri, and S. Bose, arXiv preprint arXiv:1704.06166 (2017).

[54] M. A. Khan, A. B. Karki, T. Samanta, D. Browne, S. Stadler, I. Vekhter, A. Pandey, P. W. Adams, D. P. Young, S. Teknowijoyo, K. Cho, R. Prozorov, and D. E. Graf, Phys. Rev. B **94**, 144515 (2016).

[55] L. Jiao, J. L. Zhang, Y. Chen, Z. F. Weng, Y. M. Shao, J. Y. Feng, X. Lu, B. Joshi, A. Thamizhavel, S. Ramakrishnan, and H. Q. Yuan, Phys. Rev. B **89**, 060507 (2014).

[56] T. Terashima, M. Kimata, S. Uji, T. Sugawara, N. Kimura, H. Aoki, and H. Harima, Phys. Rev. B **78**, 205107 (2008).

[57] R. Settai, I. Sugitani, Y. Okuda, A. Thamizhavel, M. Nakashima, Y. Onuki, and H. Harima, Journal of Magnetism and Magnetic Materials **310**, 844 (2007), proceedings of the 17th International Conference on Magnetism.

[58] R. Settai, Y. Okuda, I. Sugitani, Y. Ōnuki, T. Matsuda, Y. Haga, and H. Harima, International Journal of Modern Physics B **21**, 3238 (2007).

[59] S. Kuroiwa, Y. Saura, J. Akimitsu, M. Hiraishi, M. Miyazaki, K. H. Satoh, S. Takeshita, and R. Kadono, Phys. Rev. Lett. **100**, 097002 (2008).

[60] J. Chen, M. B. Salamon, S. Akutagawa, J. Akimitsu, J. Singleton, J. L. Zhang, L. Jiao, and H. Q. Yuan, Phys. Rev. B **83**, 144529 (2011).

[61] Y. Nishikayama, T. Shishidou, and T. Oguchi, Journal of the Physical Society of Japan **76**, 064714 (2007).

[62] W. Lee, H. Zeng, Y. Yao, and Y. Chen, Physica C: Superconductivity **266**, 138 (1996).

[63] I. Bonalde, R. Ribeiro, K. Syu, H. Sung, and W. Lee, New Journal of Physics **13**, 123022 (2011).

[64] J. Chen, L. Jiao, J. Zhang, Y. Chen, L. Yang, M. Nicklas, F. Steglich, and H. Yuan, New Journal of Physics **15**, 053005 (2013).

[65] D. C. Peets, A. Maldonado, M. Enayat, Z. Sun, P. Wahl, and A. P. Schnyder, Physical Review B **93**, 174504 (2016).

[66] M. Mondal, B. Joshi, S. Kumar, A. Kamlapure, S. C. Ganguli, A. Thamizhavel, S. S. Mandal, S. Ramakrishnan, and P. Raychaudhuri, Phys. Rev. B **86**, 094520 (2012).

[67] J. S. Kim, W. Xie, R. K. Kremer, V. Babizhetskyy, O. Jepsen, A. Simon, K. S. Ahn, B. Raquet, H. Rakoto, J.-M. Broto, and B. Ouladdiaf, Phys. Rev. B **76**, 014516 (2007).

[68] S. Seki and M. Mochizuki, *Skyrmions in magnetic materials* (Springer, 2015).

[69] N. Kanazawa, *Charge and Heat Transport Phenomena in Electronic and Spin Structures in B20-type Compounds* (Springer, 2015).

[70] C. Pfleiderer, T. Adams, A. Bauer, W. Biberacher, B. Binz, F. Birkelbach, P. Böni, C. Franz, R. Georgii, M. Janoschek, *et al.*, Journal of Physics: Condensed Matter **22**, 164207 (2010).

[71] M. C. Langner, S. Roy, S. K. Mishra, J. C. T. Lee, X. W. Shi, M. A. Hossain, Y.-D. Chuang, S. Seki, Y. Tokura, S. D. Kevan, and R. W. Schoenlein, Phys. Rev. Lett. **112**, 167202 (2014).

[72] Y. Togawa, T. Koyama, K. Takayanagi, S. Mori, Y. Kousaka, J. Akimitsu, S. Nishihara, K. Inoue, A. S. Ovchinnikov, and J. Kishine, Phys. Rev. Lett. **108**, 107202 (2012).

[73] S. S. P. Parkin, M. Hayashi, and L. Thomas, Science **320**, 190 (2008), http://science.sciencemag.org/content/320/5873/190.full.pdf .

[74] C. Pfleiderer, Nature Physics **7**, 673 (2011).

[75] N. Nagaosa and Y. Tokura, Nature nanotechnology **8**, 899 (2013).

[76] T. Skyrme, International Journal of Modern Physics A **3**, 2745 (1988).

[77] T. H. R. Skyrme, in *Proceedings of the Royal Society of London A: Mathematical, Physical and Engineering Sciences*, Vol. 260 (The Royal Society, 1961) pp. 127–138.

[78] A. Bogdanov and D. Yablonskii, Zh. Eksp. Teor. Fiz **95**, 182 (1989).

[79] A. Bogdanov and A. Hubert, Journal of magnetism and magnetic materials **138**, 255 (1994).

[80] U. Rößler, A. Bogdanov, and C. Pfleiderer, Nature **442**, 797 (2006).

[81] X. Yu, Y. Onose, N. Kanazawa, J. Park, J. Han, Y. Matsui, N. Nagaosa, and Y. Tokura, Nature **465**, 901 (2010).

[82] e. Y. Ishikawa, K. Tajima, D. Bloch, and M. Roth, Solid State Communications **19**, 525 (1976).

[83] Y. Ishikawa, G. Shirane, J. A. Tarvin, and M. Kohgi, Phys. Rev. B **16**, 4956 (1977).

[84] C. Pfleiderer, S. Julian, and G. Lonzarich, Nature **414**, 427 (2001).

[85] S. Mühlbauer, B. Binz, F. Jonietz, C. Pfleiderer, A. Rosch, A. Neubauer, R. Georgii, and P. Böni, Science **323**, 915 (2009).

[86] I. Dzyaloshinsky, Journal of Physics and Chemistry of Solids **4**, 241 (1958).

[87] T. Moriya, Phys. Rev. **120**, 91 (1960).

[88] M. Kataoka, Journal of the Physical Society of Japan **56**, 3635 (1987).

[89] P. Milde, D. Köhler, J. Seidel, L. Eng, A. Bauer, A. Chacon, J. Kindervater, S. Mühlbauer, C. Pfleiderer, S. Buhrandt, *et al.*, Science **340**, 1076 (2013).

[90] J. Beille, J. Voiron, F. Towfiq, M. Roth, and Z. Y. Zhang, Journal of Physics F: Metal Physics **11**, 2153 (1981).

[91] K. Ishimoto, M. Ohashi, H. Yamauchi, and Y. Yamaguchi, Journal of the Physical Society of Japan **61**, 2503 (1992).

[92] X. Yu, N. Kanazawa, Y. Onose, K. Kimoto, W. Zhang, S. Ishiwata, Y. Matsui, and Y. Tokura, Nature materials **10**, 106 (2011).

[93] N. Kanazawa, Y. Onose, T. Arima, D. Okuyama, K. Ohoyama, S. Wakimoto, K. Kakurai, S. Ishiwata, and Y. Tokura, Phys. Rev. Lett. **106**, 156603 (2011).

[94] T. Adams, A. Chacon, M. Wagner, A. Bauer, G. Brandl, B. Pedersen, H. Berger, P. Lemmens, and C. Pfleiderer, Phys. Rev. Lett. **108**, 237204 (2012).

[95] Y. Kabiri, A. Kermanpur, and A. Foroozmehr, Vacuum **86**, 1073 (2012).

[96] "Arc melting diagram," `http://slideplayer.com/slide/6242912/`, accessed: 09-30-2017.

[97] N. Haldolaarachchige, *Strongly Correlated Electron Behavior in Transition Metal Intermetallics: Enhanced Thermoelectricity and Quantum Criticality in $FeGa_3$ and Superconductivity in $NiBi_3$* (Louisiana State University, 2012).

[98] "Induction heating block diagram," `http://nvlpubs.nist.gov/nistpubs/jres/104/3/html/j43nav.htm` (), accessed: 09-30-2017.

[99] "Principle of induction heating," `http://www.gh-ia.com/induction_heating.html` (), accessed: 09-30-2017.

[100] A. R. West, *Solid state chemistry and its applications* (John Wiley & Sons, 2007).

[101] H. J. Scheel, P. Capper, and P. Rudolph, *Crystal Growth Technology: Semiconductors and Dielectrics* (John Wiley & Sons, 2010).

[102] "Vertical Bridgman Technique," `http://aam.mathematik.uni-freiburg.de/IAM/homepages/alfred/BSSBBDK.html`, accessed: 09-30-2017.

[103] "Floating zone technique," `http://www.tf.uni-kiel.de/matwis/amat/elmat_en/kap_6/advanced/t6_1_3.html` (), accessed: 09-30-2017.

[104] "Floating Zone Furnace," `http://www.crystalsys.co.jp/english/product02_e.html` (), accessed: 09-30-2017.

[105] N. L. Parr, *Zone refining and allied techniques* (Newnes, 1960).

[106] A. Brown, *JD Bernal: the sage of science* (Oxford University Press, 2005).

[107] "Braggs law," http://serc.carleton.edu/research_education/geochemsheets/BraggsLaw.html, accessed: 09-30-2017.

[108] "Shared instrumention facility," https://sites01.lsu.edu/faculty/sif/, accessed: 09-30-2017.

[109] J. Rodriguez-Carvajal, in *satellite meeting on powder diffraction of the XV congress of the IUCr*, Vol. 127 (Toulouse, France:[sn], 1990).

[110] "Scanning Electron Microscope," https://www.purdue.edu/ehps/rem/rs/sem.htm, accessed: 09-30-2017.

[111] "Wavelength Dispersive Spectroscopy," http://serc.carleton.edu/research_education/geochemsheets/wds.html, accessed: 09-30-2017.

[112] "Quantum Design ppms," https://www.qdusa.com/sitedocs/productBrochures/1070-002.pdf, accessed: 09-30-2017.

[113] F. Pobell, *Matter and methods at low temperatures* (Springer Science & Business Media, 2007).

[114] R. Schutz, Review of Scientific Instruments **45**, 548 (1974).

[115] N. W. Ashcroft and N. D. Mermin, *Solid state physics* (Holt, Rinehart and Winston, 1976).

[116] H. Q. Yuan, D. F. Agterberg, N. Hayashi, P. Badica, D. Vandervelde, K. Togano, M. Sigrist, and M. B. Salamon, Phys. Rev. Lett. **97**, 017006 (2006).

[117] G. Goll, *Unconventional superconductors: experimental investigation of the order-parameter symmetry*, Vol. 214 (Springer Science & Business Media, 2006).

[118] R. P. Singh, G. Balakrishnan, D. M. Paul, and M. R. Lees, unpublished (2015).

[119] J. Quintanilla, A. D. Hillier, J. F. Annett, and R. Cywinski, Phys. Rev. B **82**, 174511 (2010).

[120] G. M. Luke, Y. Fudamoto, K. M. Kojima, M. I. Larkin, J. Merrin, B. Nachumi, Y. J. Uemura, Y. Maeno, Z. Q. Mao, and Y. Mori, Nature **394**, 558 (1998).

[121] J. Xia, Y. Maeno, P. T. Beyersdorf, M. M. Fejer, and A. Kapitulnik, Phys. Rev. Lett. **97**, 167002 (2006).

[122] G. M. Luke, A. Keren, L. P. Le, W. D. Wu, Y. J. Uemura, D. A. Bonn, L. Taillefer, and J. D. Garrett, Phys. Rev. Lett. **71**, 1466 (1993).

[123] P. de Rotier, A. Huxley, A. Yaouanc, J. Flouquet, P. Bonville, P. Imbert, P. Pari, P. Gubbens, and A. Mulders, Physics Letters A **205**, 239 (1995).

[124] Y. Aoki, A. Tsuchiya, T. Kanayama, S. R. Saha, H. Sugawara, H. Sato, W. Higemoto,

A. Koda, K. Ohishi, K. Nishiyama, and R. Kadono, Phys. Rev. Lett. **91**, 067003 (2003).

[125] A. Maisuradze, W. Schnelle, R. Khasanov, R. Gumeniuk, M. Nicklas, H. Rosner, A. Leithe-Jasper, Y. Grin, A. Amato, and P. Thalmeier, Phys. Rev. B **82**, 024524 (2010).

[126] A. D. Hillier, J. Quintanilla, B. Mazidian, J. F. Annett, and R. Cywinski, Phys. Rev. Lett. **109**, 097001 (2012).

[127] B. Matthias, V. Compton, and E. Corenzwit, Journal of Physics and Chemistry of Solids **19**, 130 (1961).

[128] J. Bardeen, G. Rickayzen, and L. Tewordt, Phys. Rev. **113**, 982 (1959).

[129] M. Houssa and M. Ausloos, Journal of Physics: Condensed Matter **9**, 201 (1997).

[130] R. C. Yu, M. B. Salamon, J. P. Lu, and W. C. Lee, Phys. Rev. Lett. **69**, 1431 (1992).

[131] A. F. May, M. A. McGuire, J. E. Mitchell, A. S. Sefat, and B. C. Sales, Phys. Rev. B **88**, 064502 (2013).

[132] Y. Machida, K. Tomokuni, T. Isono, K. Izawa, Y. Nakajima, and T. Tamegai, Physica E **43**, 714 (2011).

[133] J. G. Checkelsky, R. Thomale, L. Li, G. F. Chen, J. L. Luo, N. L. Wang, and N. P. Ong, Phys. Rev. B **86**, 180502 (2012).

[134] Y. Zhang, N. P. Ong, P. W. Anderson, D. A. Bonn, R. Liang, and W. N. Hardy, Phys. Rev. Lett. **86**, 890 (2001).

[135] J.-P. Reid, M. A. Tanatar, X. G. Luo, H. Shakeripour, N. Doiron-Leyraud, N. Ni, S. L. Bud'ko, P. C. Canfield, R. Prozorov, and L. Taillefer, Phys. Rev. B **82**, 064501 (2010).

[136] C. T. V. Degrift, Physica B+C **108**, 1361 (1981).

[137] R. Prozorov and R. W. Giannetta, Superconductor Science and Technology **19**, R41 (2006).

[138] R. Prozorov and V. G. Kogan, Reports on Progress in Physics **74**, 124505 (2011).

[139] A. Eiling and J. S. Schilling, Journal of Physics F: Metal Physics **11**, 623 (1981).

[140] K. Blaha, P.and Schwarz, G. K. H. Madsen, D. Kvasnicka, and J. Luitz, Vienna: Karlheinz Schwarz, Technical University of Wien (2001).

[141] J. P. Perdew, K. Burke, and M. Ernzerhof, Phys. Rev. Lett. **77**, 3865 (1996).

[142] A. C. Jacko, J. Fjaerestad, and B. J. Powell, Nat. Phys. **6**, 422 (2009).

[143] K. Kadowaki and S. Woods, Solid State Communications **58**, 507 (1986).

[144] A. B. Karki, Y. M. Xiong, N. Haldolaarachchige, S. Stadler, I. Vekhter, P. W. Adams, D. P. Young, W. A. Phelan, and J. Y. Chan, Phys. Rev. B **83**, 144525 (2011).

[145] E. Helfand and N. R. Werthamer, Phys. Rev. **147**, 288 (1966).

[146] N. R. Werthamer, E. Helfand, and P. C. Hohenberg, Phys. Rev. **147**, 295 (1966).

[147] T. P. Orlando, E. J. McNiff, S. Foner, and M. R. Beasley, Phys. Rev. B **19**, 4545 (1979).

[148] M. Schossmann and J. P. Carbotte, Phys. Rev. B **39**, 4210 (1989).

[149] K. Maki, Phys. Rev. **148**, 362 (1966).

[150] A. B. Karki, Y. M. Xiong, I. Vekhter, D. Browne, P. W. Adams, D. P. Young, K. R. Thomas, J. Y. Chan, H. Kim, and R. Prozorov, Phys. Rev. B **82**, 064512 (2010).

[151] K. Behnia, R. Bel, Y. Kasahara, Y. Nakajima, H. Jin, H. Aubin, K. Izawa, Y. Matsuda, J. Flouquet, Y. Haga, Y. Ōnuki, and P. Lejay, Phys. Rev. Lett. **94**, 156405 (2005).

[152] A. Kowalczyk, T. Tolinski, M. Reiffers, M. Pugaczowa-Michalska, G. Chelkowska, and E. Gao, Journal of Physics: Condensed Matter **20**, 255252 (2008).

[153] J. Annett, N. Goldenfeld, and S. R. Renn, Phys. Rev. B **43**, 2778 (1991).

[154] I. Bonalde, H. Kim, R. Prozorov, C. Rojas, P. Rogl, and E. Bauer, Phys. Rev. B **84**, 134506 (2011).

[155] E. Bauer, G. Rogl, X.-Q. Chen, R. T. Khan, H. Michor, G. Hilscher, E. Royanian, K. Kumagai, D. Z. Li, Y. Y. Li, R. Podloucky, and P. Rogl, Phys. Rev. B **82**, 064511 (2010).

[156] W. L. McMillan, Phys. Rev. **167**, 331 (1968).

[157] C. K. Poole, H. A. Farach, and R. J. Creswick, *Handbook of superconductivity* (Academic press, 1999).

[158] P. A. Beck and H. Claus, JOURNAL OF RESEARCH OF THE NATIONAL BUREAU OF STANDARDS SECTION A-PHYSICS AND CHEMISTRY , 449 (1970).

[159] Z. F. Weng, J. L. Zhang, M. Smidman, T. Shang, J. Quintanilla, J. F. Annett, M. Nicklas, G. M. Pang, L. Jiao, W. B. Jiang, Y. Chen, F. Steglich, and H. Q. Yuan, Phys. Rev. Lett. **117**, 027001 (2016).

[160] L. Fu, C. L. Kane, and E. J. Mele, Phys. Rev. Lett. **98**, 106803 (2007).

[161] Y. L. Chen, J. G. Analytis, J.-H. Chu, Z. K. Liu, S.-K. Mo, X. L. Qi, H. J. Zhang,

D. H. Lu, X. Dai, Z. Fang, S. C. Zhang, I. R. Fisher, Z. Hussain, and Z.-X. Shen, Science **325**, 178 (2009).

[162] Y. Xia, D. Qian, D. Hsieh, L. Wray, A. Pal, H. Lin, A. Bansil, D. Grauer, Y. S. Hor, R. J. Cava, and M. Z. Hasan, Nature Physics **5**, 398 (2009).

[163] M. Z. Hasan and C. L. Kane, Rev. Mod. Phys. **82**, 3045 (2010).

[164] M. König, S. Wiedmann, C. Brüne, A. Roth, H. Buhmann, L. W. Molenkamp, X.-L. Qi, and S.-C. Zhang, Science **318**, 766 (2007).

[165] X.-L. Qi and S.-C. Zhang, Rev. Mod. Phys. **83**, 1057 (2011).

[166] Y. S. Hor, A. J. Williams, J. G. Checkelsky, P. Roushan, J. Seo, Q. Xu, H. W. Zandbergen, A. Yazdani, N. P. Ong, and R. J. Cava, Phys. Rev. Lett. **104**, 057001 (2010).

[167] M. Sato and S. Fujimoto, Phys. Rev. B **79**, 094504 (2009).

[168] A. P. Schnyder and S. Ryu, Phys. Rev. B **84**, 060504 (2011).

[169] B. Béri, Phys. Rev. B **81**, 134515 (2010).

[170] S. Sasaki, M. Kriener, K. Segawa, K. Yada, Y. Tanaka, M. Sato, and Y. Ando, Phys. Rev. Lett. **107**, 217001 (2011).

[171] F. Wilczek, Nature Physics **5**, 614 (2009).

[172] B. Joshi, A. Thamizhavel, and S. Ramakrishnan, Physical Review B **84**, 064518 (2011).

[173] Y. Bhatt and K. Schubert, Journal of the Less Common Metals **70**, P39 (1980).

[174] H. M. Benia, E. Rampi, C. Trainer, C. M. Yim, A. Maldonado, D. C. Peets, A. Stöhr, U. Starke, K. Kern, A. Yaresko, G. Levy, A. Damascelli, C. R. Ast, A. P. Schnyder, and P. Wahl, Phys. Rev. B **94**, 121407 (2016).

[175] Z. Sun, M. Enayat, A. Maldonado, C. Lithgow, E. Yelland, D. C. Peets, A. Yaresko, A. P. Schnyder, and P. Wahl, Nat. Commun. **6**, 6633 (2015).

[176] S. Thirupathaiah, S. Ghosh, R. Jha, E. D. L. Rienks, K. Dolui, V. V. Ravi Kishore, B. Büchner, T. Das, V. P. S. Awana, D. D. Sarma, and J. Fink, Phys. Rev. Lett. **117**, 177001 (2016).

[177] C. Caroli, P. D. Gennes, and J. Matricon, Physics Letters **9**, 307 (1964).

[178] X. B. Yan, Y. Xu, L. P. He, J. K. Dong, H. Cho, D. C. Peets, J.-G. Park, and S. Y. Li, Superconductor Science and Technology **29**, 065001 (2016).

[179] G. M. Pang, M. Smidman, L. X. Zhao, Y. F. Wang, Z. F. Weng, L. Q. Che, Y. Chen,

X. Lu, G. F. Chen, and H. Q. Yuan, Phys. Rev. B **93**, 060506 (2016).

[180] D. Shoenberg, *Magnetic oscillations in metals* (Cambridge University Press, 2009).

[181] J. Hu, Z. Tang, J. Liu, X. Liu, Y. Zhu, D. Graf, K. Myhro, S. Tran, C. N. Lau, J. Wei, and Z. Mao, Phys. Rev. Lett. **117**, 016602 (2016).

[182] M. Berry, Journal of Physics A: Mathematical and General **18**, 15 (1985).

[183] C. Chamon, M. O. Goerbig, R. Moessner, and L. F. Cugliandolo, *Topological Aspects of Condensed Matter Physics: Lecture Notes of the Les Houches Summer School: Volume 103, August 2014*, Vol. 103 (Oxford University Press, 2017).

[184] D. Xiao, M.-C. Chang, and Q. Niu, Reviews of modern physics **82**, 1959 (2010).

[185] G. P. Mikitik and Y. V. Sharlai, Phys. Rev. Lett. **82**, 2147 (1999).

[186] J. Zak, Phys. Rev. Lett. **62**, 2747 (1989).

[187] Y. Bhatt and K. Schubert, Journal of the Less Common Metals **64**, P17 (1979).

[188] H. Takahashi, K. Ando, and Y. Shirakawabe, Ultramicroscopy **91**, 63 (2002).

[189] I. Pro, Lake Oswego, Oregon, USA. (2011).

[190] J. G. Analytis, R. D. McDonald, J.-H. Chu, S. C. Riggs, A. F. Bangura, C. Kucharczyk, M. Johannes, and I. R. Fisher, Phys. Rev. B **80**, 064507 (2009).

[191] I. M. Lifshitz and A. M. Kosevich, Sov. Phys. JETP **2**, 636 (1956).

[192] J. Xiong, Y. Luo, Y. Khoo, S. Jia, R. J. Cava, and N. P. Ong, Phys. Rev. B **86**, 045314 (2012).

[193] Y. Ando, Journal of the Physical Society of Japan **82**, 102001 (2013).

[194] A. Bauer and C. Pfleiderer, Phys. Rev. B **85**, 214418 (2012).

[195] B. Lebech, J. Bernhard, and T. Freltoft, Journal of Physics: Condensed Matter **1**, 6105 (1989).

[196] N. Kanazawa, J.-H. Kim, D. S. Inosov, J. S. White, N. Egetenmeyer, J. L. Gavilano, S. Ishiwata, Y. Onose, T. Arima, B. Keimer, and Y. Tokura, Phys. Rev. B **86**, 134425 (2012).

[197] N. Manyala, Y. Sidis, J. F. DiTusa, G. Aeppli, D. P. Young, and Z. Fisk, Nature materials **3**, 255 (2004).

[198] J. F. DiTusa, S. B. Zhang, K. Yamaura, Y. Xiong, J. C. Prestigiacomo, B. W. Fulfer, P. W. Adams, M. I. Brickson, D. A. Browne, C. Capan, Z. Fisk, and J. Y. Chan, Phys. Rev. B **90**, 144404 (2014).

[199] Z. Xiong, X. Wang, L. Cao, J. Wang, J. Yu, H. Yin, X. Wang, and J. Mao, Journal of Alloys and Compounds **693**, 440 (2017).

[200] G. M. Sheldrick, Acta Crystallographica Section A **64**, 112 (2008).

[201] A. Altomare, M. C. Burla, M. Camalli, G. L. Cascarano, C. Giacovazzo, A. Guagliardi, A. G. Moliterni, G. Polidori, and R. Spagna, Journal of Applied Crystallography **32**, 115 (1999).

[202] Z. Otwinowski and W. Minor, Methods in Enzymology **276**, 307 (1997).

[203] "Four circle Diffractometer," `https://neutrons.ornl.gov/hb3a`, accessed: 09-30-2017.

[204] "General Purpose Small Angle Neutron Scattering Diffractometer," `https://neutrons.ornl.gov/gpsans`, accessed: 09-30-2017.

[205] V. Zaitsev, M. Fedorov, I. Eremin, E. Gurieva, and D. Rowe, CRC Press, Taylor & Francis, Boca Raton (2006).

[206] S. Paschen, E. Felder, M. A. Chernikov, L. Degiorgi, H. Schwer, H. R. Ott, D. P. Young, J. L. Sarrao, and Z. Fisk, Phys. Rev. B **56**, 12916 (1997).

[207] Y. Onose, N. Takeshita, C. Terakura, H. Takagi, and Y. Tokura, Phys. Rev. B **72**, 224431 (2005).

[208] S. M. Stishov and A. E. Petrova, Physics-Uspekhi **54**, 1117 (2011).

[209] P. Rhodes and E. P. Wohlfarth, in *Proceedings of the Royal Society of London A: Mathematical, Physical and Engineering Sciences*, Vol. 273 (The Royal Society, 1963) pp. 247–258.

[210] T. Chatterji, *Neutron scattering from magnetic materials* (Gulf Professional Publishing, 2005).

[211] S. Tatsuoka, H. Sato, K. Tanaka, M. Ueda, D. Kikuchi, H. Aoki, T. Ikeno, K. Kuwahara, Y. Aoki, H. Sugawara, and H. Harima, Journal of the Physical Society of Japan **77**, 033701 (2008), http://dx.doi.org/10.1143/JPSJ.77.033701 .

[212] J. Beille, J. Voiron, and M. Roth, Solid state communications **47**, 399 (1983).

[213] D. Mandrus, J. L. Sarrao, A. Migliori, J. D. Thompson, and Z. Fisk, Phys. Rev. B **51**, 4763 (1995).

[214] H. Hohl, A. Ramirez, C. Goldmann, G. Ernst, and E. Bucher, Journal of Alloys and Compounds **278**, 39 (1998).

[215] N. Manyala, J. F. DiTusa, G. Aeppli, and A. P. Ramirez, Nature **454**, 976 (2008).

[216] N. Manyala, Y. Sidis, J. F. DiTusa, G. Aeppli, D. P. Young, and Z. Fisk, Nature

**404**, 581 (2000).

[217] J. F. DiTusa, K. Friemelt, E. Bucher, G. Aeppli, and A. P. Ramirez, Phys. Rev. Lett. **78**, 2831 (1997).

[218] A. Lacerda, H. Zhang, P. Canfield, M. Hundley, Z. Fisk, J. Thompson, C. Seaman, M. Maple, and G. Aeppli, Physica B: Condensed Matter **186188**, 1043 (1993).

[219] M. A. Chernikov, L. Degiorgi, E. Felder, S. Paschen, A. D. Bianchi, H. R. Ott, J. L. Sarrao, Z. Fisk, and D. Mandrus, Phys. Rev. B **56**, 1366 (1997).

[220] M. A. Chernikov, L. Degiorgi, E. Felder, S. Paschen, A. D. Bianchi, H. R. Ott, J. L. Sarrao, Z. Fisk, and D. Mandrus, Phys. Rev. B **56**, 1366 (1997).

[221] P. Tunbridge, *Lord Kelvin: his influence on electrical measurements and units*, 18 (Iet, 1992).

# Vita

Mojammel Alam Khan was born in a small town, Feni of the south Asian nation Bangladesh. After successful completion of his high school and college education with high merit, he was accepted in the biggest and most prominent university of Bangladesh, the University of Dhaka. Here he majored in Physics and successfully completed his Bachelor in Science in 2011. He came to Louisiana State University in the Fall of 2012 to pursue higher studies in experimental physics. He completed his Master of Science degree in physics in 2016 and hopes to receive his Doctor of Philosophy in December 2017.